

Cover Page



Universiteit Leiden



The handle <http://hdl.handle.net/1887/21918> holds various files of this Leiden University dissertation.

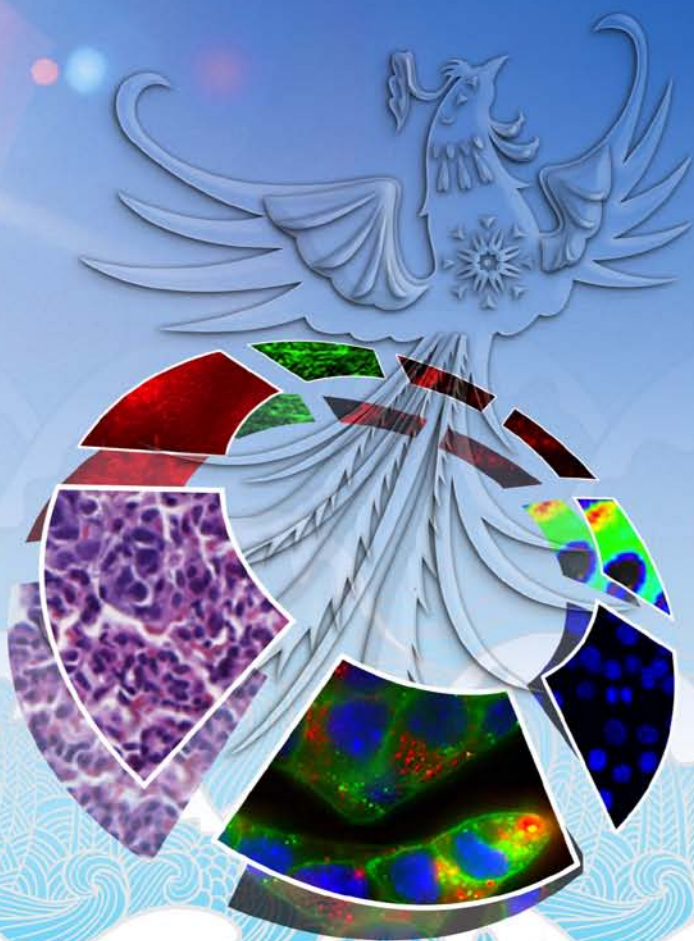
**Author:** Xie, Bangwen

**Title:** Optical imaging of cancer and cell death

**Issue Date:** 2013-10-08

# Optical Imaging

of Cancer and Cell Death



Bangwen Xie



# Optical Imaging

of Cancer and Cell Death



Bangwen Xie

---

Thesis layout and cover design by P.J.H. Fijlstra and M. Calusinska  
Cover illustration based on figures from Chapter 2  
Printed by Gildeprint Drukkerijen

The studies presented in this thesis were supported by the Center for Translational Molecular Medicine, project MUSIS (grant 03O-202), the Netherlands.

Costs associated with the publication of this thesis were financially supported by PerkinElmer, Percuros BV, LI-COR Biosciences, Ilumicare BV and the Department of Radiology of Leiden University Medical Center.

ISBN: 978-94-6108-509-2

© 2013 Bangwen Xie. Leiden, The Netherlands.

All rights reserved. No part of this publication may be reproduced or transmitted in any form, by any means without prior written permission of the author.

---

# Optical Imaging of Cancer and Cell Death

## PROEFSCHRIFT

ter verkrijging van  
de graad van Doctor aan de Universiteit Leiden,  
op gezag van Rector Magnificus prof. mr. C.J.J.M. Stolker,  
volgens besluit van het College voor Promoties  
te verdedigen op  
dinsdag 8 oktober 2013  
klokke 11.15 uur

door

**Bangwen Xie**

Geboren te Jiangxi, China  
in 1985

# Promotiecommissie

## Promotor

Prof. dr. C.W.G.M. Löwik

## Co-promotoren

Dr. E.L. Kaijzel

Dr. E.R. van Beek

## Overige leden

Prof. Dr. B.P.F. Lelieveldt

Prof. Dr. M. Hoehn (Max Planck Institute for Neurological Research, Cologne)

Dr. M. Robillard (Tagworks Pharmaceuticals, Eindhoven)

To my mother and father

谨以此书献给我的父亲母亲

天道酬勤

事在人为

Good things come to the one who works hard

# Contents

Chapter 1	Introduction	9
Chapter 2	Dual-Wavelength Imaging of Tumor Progression by Activatable and Targeting Near-Infrared Fluorescent Probes in a Bioluminescent Breast Cancer Model	27
Chapter 3	Multicolor Fluorescence Imaging of Traumatic Brain Injury in a Cryolesion Mouse Model	47
Chapter 4	Optical Imaging of Cell Death in Traumatic Brain Injury Using a Heat Shock Protein-90 Alkylator	67
Chapter 5	Optical Imaging of Treatment-related Tumor Cell Death Using a Heat Shock Protein-90 Alkylator	87
Chapter 6	General Discussion and Future Scope	107
Chapter 7	Summary – 论文摘要 – Samenvatting	117
Chapter 8	Miscellaneous Acknowledgements – 致谢 – Dankwoord Curriculum Vitae – 作者简介 – Biografie List of Publications	129





# CHAPTER ONE

## Introduction



## 1.1 General introduction of Molecular imaging

Molecular imaging can be broadly defined as the science to non-invasively visualize and quantitatively analyze the function of *in vivo* biological processes at the cellular and molecular level<sup>1,2</sup>. The technique of molecular imaging has enabled real-time monitoring of expression of specific genes and the localization of probes or markers. It non-invasively provides the visualization, characterization and eventually quantification of cellular and molecular processes, under physiological or pathological conditions, in a living organism. Especially over the last two decades, the technique of molecular imaging has become increasingly important and currently plays a crucial role in the areas of fundamental and clinical research, including regenerative medicine, drug development, image guided therapy, cancer and stem cell therapies<sup>3-6</sup>.

Molecular imaging makes use of various imaging agents and modalities and in recent years, the resolution and image quality of existing imaging systems have improved continuously by choosing a suitable molecular imaging agent for its matching imaging modality. The various existing imaging technologies differ in several aspects, like spatial resolution, depth penetration, energy expended for image generation, availability of injectable/biocompatible molecular probes and the respective detection threshold of probes for a given technology<sup>7</sup>.

### 1.1.1 Imaging modalities

Current molecular imaging modalities mainly include optical imaging, nuclear imaging, ultrasound, MRI and computed tomography (CT). These modalities vary broadly in sensitivity and spatial resolution. Figure 1 shows an overview of the most common molecular imaging modalities used in pre-clinical settings. In general, the two most sensitive imaging modalities are optical imaging and nuclear imaging. Optical imaging mainly consists of bioluminescence imaging (BLI) and fluorescence imaging (FLI), whereas nuclear imaging includes single-photon emission computed tomography (SPECT) and positron emission tomography (PET). Amongst the relatively low sensitivity but high spatial resolution modalities, ultrasound is a modality with a broad clinical availability. Another common modality that is found in hospitals and clinical centers worldwide is MRI. Compared to optical imaging and nuclear imaging, MRI requires larger quantities of the contrast agent, normally at micro-molar range. Besides optical imaging, nuclear imaging and ultrasound, other imaging techniques, e.g. CT and MRI, have been used more for diagnostic imaging as they predominantly provide anatomical pictures. Each imaging modality has its advantages and disadvantages and a number of reviews have summarized the complexity and diversity of current molecular imaging modalities<sup>8-11</sup>. The ideal

situation is to be able to obtain sophisticated imaging at the molecular level with a high sensitivity and high spatial resolution. A final unmet need is to integrate the different imaging modalities so that complementary information can be obtained from each modality.

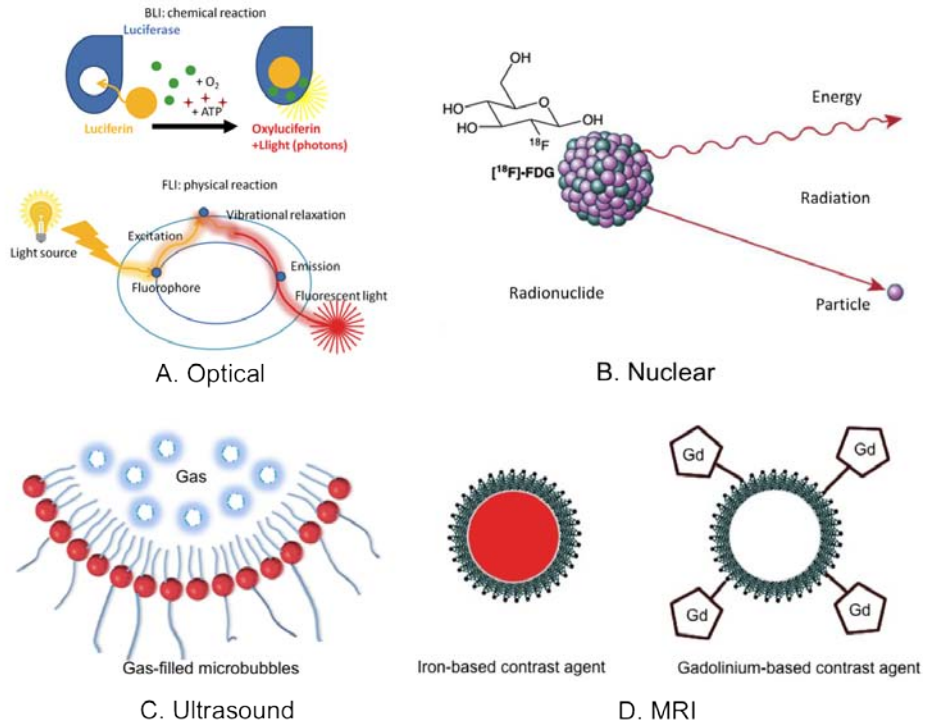


**Figure 1. Overview of four common molecular imaging modalities.** A. Optical imaging: for BLI, substrate (e.g. luciferin) is required to react with enzymes (e.g. luciferase) to enable native light emission; or for FLI, probes with fluorophores (e.g. fluorescein) consist of small molecules that may be quenched with fluorescence potential and only liberated after specific enzymatic cleavage or upon molecular target binding. B. Nuclear imaging (SPECT/PET): SPECT uses gamma rays to provide 3D information as cross-sectional slices and PET detects positron emission from radionuclides, commonly 18-Fluorine. Small molecules, including drugs, can be adapted to incorporate suitable radionuclides enabling both localization and quantification of molecular expression. C. Ultrasound: active microbubbles made from albumin or lipids are relatively in large structures (5 to 10  $\mu\text{m}$  diameter). They are typically bound to activated endothelium. D. MRI: Depends on the type of delivery payloads, either ultra-small superparamagnetic-based molecular imaging agent (e.g. iron oxides) or paramagnetic-based molecular imaging agent (e.g. gadolinium chelates) can be employed. Iron oxide particles (size range  $\sim 10$  nm to 5  $\mu\text{m}$ ) are commonly equipped within polymer shells. Gadolinium contrast requires interaction with local water molecules, so that the surface of the carrier is often decorated by the gadolinium chelates <sup>12</sup>.

For all types of imaging modalities, the signal-to-background ratio (SBR) is always a parameter needs to be addressed. SBR is a measure used to compare the level of a desired signal to the level of background noise. SBR is defined as

the ratio of signal power to the noise power and a ratio higher than 1 indicates more signal than noise.

Most of molecular imaging modalities can obtain the desired signals without any enhancement or modification. However, sometimes for improving the SBR, the imageable signal needs to be enhanced to a level strong enough for visualization. The methods vary from improving target concentration by pretargeting, specific chemical activation, conformational changes, multivalency, or biological trapping to obtain maximized specificity<sup>1,13</sup>. For example, Barbet J. *et al* proved that target concentration in tumor tissues can be enhanced while their uptake in normal tissues is reduced by pretargeting labeled bivalent haptens with bispecific antibodies<sup>14</sup>. Whereas Weissleder R. *et al* made use of protease-activated near-infrared fluorescent probes for imaging, resulting in high SBR upon proteolytic activation of the fluorophores<sup>15</sup>.

In this thesis, we will mainly focus on optical imaging and its pre-clinical applications, both at the microscopic and macroscopic level, because it has the potential to significantly enhance our understanding of basic cancer and cell death mechanisms. Compared to nuclear imaging, ultrasound, MRI and CT which are already in function in the clinic, optical imaging provides wider functional contrast than current clinical imaging techniques. This is done either by intrinsic monitoring of physiological changes, e.g. bioluminescence, and light absorption, or by external contrast such as the use of fluorescence probes. Importantly, optical imaging is generally non-invasive and high-throughput, the equipment needed for measurements is of low cost. Eventually, we hope optical imaging can be implemented as the next clinical modality in conjunction with the other already established clinical imaging techniques.

## 1.1.2 Molecular imaging agents

Next to a molecular imaging modality, a specific molecular imaging agent, which is related to the biological process of interest, is the key requirement for molecular imaging. The term molecular imaging agent can be broadly defined as a probe that is used to visualize and characterize biological processes in living organisms, where the probe can be detectable by a certain molecular imaging modality described above. Both endogenous and exogenous molecules can be used as molecular imaging agents<sup>16</sup>. Commonly an imaging agent is a high-affinity ligand conjugated to signal molecules, which can be detected by an appropriate imaging modality. This ligand recognizes a specific molecular target, like certain enzymes, adhesion molecules and their receptors, growth factors and cytokine receptors and reporter genes<sup>1,17-19</sup>. Examples of different reporter systems are illustrated in Figure 2.

After the selection of a molecular target, a high-affinity ligand possessing the

specificity for the selected target needs to be chosen. This means the ligand should have high specificity to reach the intended target at a sufficient concentration within a short amount of time, so that it can be detected *in vivo* before degradation or excretion occurs. Such ligand can be a peptide, an engineered monoclonal antibody or antibody fragment, a recombinant protein, an aptamer, an oligosaccharide or another small molecule<sup>1,19</sup>. The ligand can recognize the target specifically through various means, e.g. receptor or antibody recognition, enzymatic activation and/or cellular trapping<sup>20</sup>.) Many antibodies have been used against numerous targets including epidermal growth factor receptor,  $\alpha_v\beta_3$  integrin, glucose transporter and matrix metalloproteinases (MMPs). The production of antibodies, however, is relatively complex and expensive<sup>21-24</sup>. For this, small cell-penetrating peptides (CPPs) have been considered to be good alternatives. CPPs are able to penetrate cell membranes efficiently and labeled CPPs can also be specifically activated by certain proteases, like MMPs and Cathepsins<sup>25-27</sup>. Furthermore, dual-modality probes can be made by linking fluorescent CPPs to nanoparticles for *in vivo* fluorescence and magnetic resonance imaging (MRI)<sup>28</sup>. Other issues like biodistribution, excretion rate, toxicity and non-specific binding should be considered when choosing an appropriate molecular imaging agent<sup>1,9</sup>.

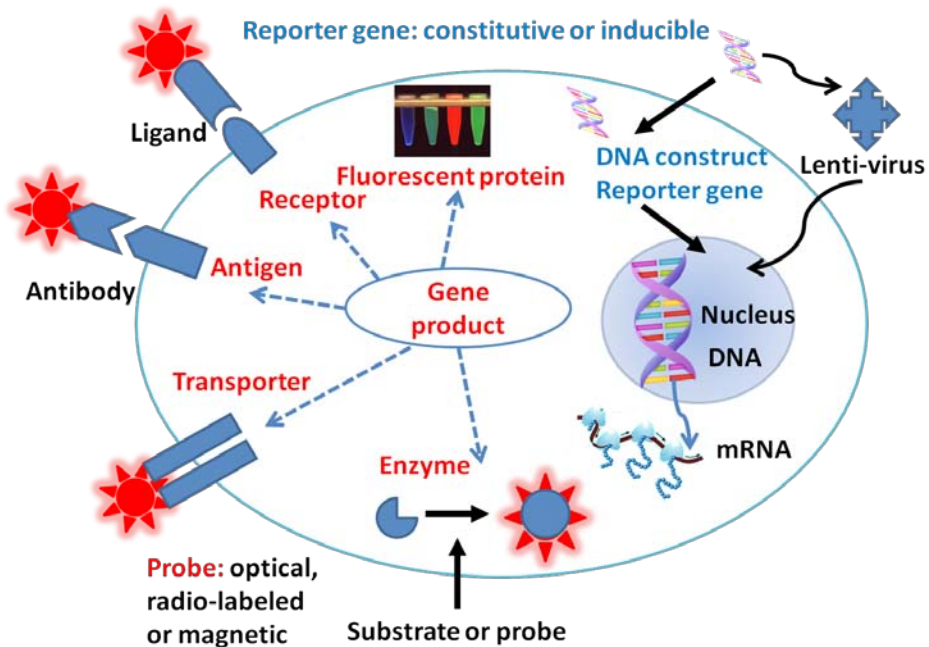


**Figure 2. Schematic representation illustrating some selected reporter systems.** Gene reporter constructs can be either driven by a constitutive active promoter resulting in a continuous production of the gene reporter product. It can also be driven by an inducible promoter that will be activated only when the specific promoter is turned on. If required, the promoter can also be tissue specific resulting in the production of the reporter gene product only in that specific tissue. For the delivery of a reporter construct, the reporter gene construct

has to be delivered to a cell (or tissue). This can be accomplished by classical transfection methods or using a viral vehicle to infect the cells. When adenoviral vectors are used the reporter gene will not be integrated into the genome of the cell and therefore will only be temporarily expressed. When classical transfection, retroviral or lentiviral constructs are used, the reporter gene will be stably integrated into the genome of the cell and the reporter will be passed on to every daughter cell after division. There are different types of gene reporters. The gene product of the reporter constructs can be an antigen, transporter, receptor, enzyme or fluorescent protein. For molecular imaging, an antibody tagged with a probe can be used to bind certain antigen; a ligand tagged with a probe can be used to recognize a specific receptor; a transported molecule tagged with a probe can be used for a transporter uptake; an substrate can be used for an enzyme reaction which leads to the generation of a signal (e.g. bioluminescence) or fluorescent proteins that generate light by themselves when excited with external light source.

## 1.2 Optical imaging

Optical imaging uses light to non-invasively interrogate cellular and molecular function in living organisms and ultimately obtains information from tissue composition and biomolecular processes. Images are generated by using photons ranging from ultraviolet to near-infrared<sup>16,29</sup>.

Among different molecular imaging modalities, optical imaging is specifically appealing for *in vivo* non-invasive imaging, both at macroscopic (e.g. whole body small animal imaging) and microscopic (e.g. multi-photon microscopy and confocal microscopy) level, because of its high sensitivity and versatility<sup>30</sup>. There are a number of approaches used for optical imaging (e.g. BLI, FLI, fluorescence tomography, optical coherence tomography and photoacoustic microscopy). The various methods use bioluminescence, fluorescence, light scattering and/or absorption as the source of imaging contrast<sup>29,31-33</sup>. For example, bioluminescence is visible light generated by a living organism via a chemical reaction. So for BLI, a specific enzyme and its corresponding substrate are required. Fluorescence, however, comes from molecules that react to light in a physical process. In this process, a fluorescent object (e.g. a fluorophore) absorbs light of certain wavelengths and then emits it during vibrational relaxation. In most cases, some energy is lost as heat so that the emitted light has less energy and a longer wavelength than the light absorbed. So for FLI, an external light source for excitation is needed<sup>6,34</sup>. Nowadays, besides the conventional fluorescence reflectance imaging approach, developments in optical imaging are currently under way to extend FLI to three-dimensional imaging with volumetric information by fluorescence-mediated molecular tomography (FMT) and multispectral optoacoustic tomography (MSOT)<sup>35,36</sup>.

### 1.2.1 Bioluminescence imaging

The high sensitivity of BLI makes it to be an excellent experimental tool for fundamental research in small animals like mice. With the negligible background, BLI is particularly useful for studying diverse biological processes, including 1) longitudinally tracking luciferase-labeled cancer cells, immune cells, and other cell

---

types in rodent models; 2) Monitoring gene expression changes associated with chemical stress, tumor hypoxia and heat-shock response; 3) Assessing protein stability and function to elucidate complex disease mechanisms; 4) Imaging therapeutic delivery to enhance the specificity and efficacy of targeted gene-based therapies and accelerate drug discovery<sup>37-41</sup>.

However, BLI measurement requires a chemical reaction between luciferase and luciferin for light production, which luciferase binds its cognate luciferin and catalyzes the oxidation of the small molecule. So it cannot be employed in human or animals lacking expression of bioluminescent reporters, e.g. in syngeneic mouse models, spontaneous tumor models or chemical-induced cancer models<sup>42-44</sup>. Moreover, images acquired from BLI measurement mostly use algorithms to assign the positions of the light sources more precisely but still lack of 3D information<sup>45</sup>. These drawbacks of BLI limit its clinical translation.

To cover the drawbacks of BLI, FLI is considered to be a good alternative. Especially because of to the development of injectable NIR fluorescent probes with specific targeting or activating abilities, FLI in the NIR region will allow application in the clinic, e.g. for image-guided surgery, early disease diagnosis and therapy monitoring<sup>3,46,47</sup>.

## 1.3 Near-infrared fluorescence imaging

Due to the fact that the absorption coefficient of tissue is considerably lower in the NIR region (700-900 nm), the light can penetrate deeper (several centimeters)<sup>48</sup>. Minimal light absorption by hemoglobin and water in the NIR spectrum enables advanced FLI systems to sensitively detect NIR fluorophores *in vivo* with high resolution<sup>49</sup>.

The widely used NIR fluorophores, including cyanine dyes like Cy3, Cy5.5, Cy7, Alexa Fluor dyes like Alexa Fluor 750 and IRDye Infrared Dyes like IRDye 800CW have generated a great interest as they show favorable SBR. Currently, the NIR fluorescent probes can be broadly divided into two types: either using the NIR fluorophore solely as non-specific probes or the fluorophore coupled to a ligand serving as specific probes. Firstly, isotopes and fluorophores can be used interchangeably as non-specific imaging agents. For example, Evans blue has been commonly used in cell viability assays because of its penetrable to non-viable cells<sup>50</sup>. Indocyanine green is a cyanine dye which is used in the clinic, e.g. for the non-invasive monitor of lymph node mapping<sup>51</sup>. However, these imaging agents are associated with relatively high background signal due to the non-specific binding nature. To achieve a better SBR, many more NIR fluorescent probes are specifically targeted to recognize certain features of cells or activation-sensitive towards certain enzyme reactions<sup>52-54</sup>. Different tumor-specific targeting probes can specifically bind to different membrane targets like

glucose transporters (GLUTs) or epidermal growth factor receptors (EGFRs) <sup>55,56</sup>. For activatable probes, many are designed to be selectively activated by enzymes such as matrix metalloproteinases (MMPs) or cathepsins, which are highly expressed by, e.g. cancer cells, so that they can be used for cancer imaging <sup>57,58</sup>. Specifically, by using fluorescence resonance energy transfer (FRET) probes, more precise information about the functional specificity of certain process can be generated <sup>59</sup>. The probe is designed with linkers between pairs of fluorochromes in close proximity, typically <10nm. A donor chromophore, initially in its electronic excited state, may transfer energy to an acceptor chromophore through non-radiative dipole-dipole coupling. However, when the fluorescence is quenched due to the close proximity of fluorochromes, the capacity for excitation will be restricted. Upon the enzymatic target-induced cleavage of the linkers, the strong increase in distance between donor and acceptor chromophores will result in detectable fluorescence.

### 1.3.1 Near-infrared fluorescence imaging of cancer

FLI is a rapidly developing discipline and among various research areas, much attention has been drawn to the development of disease-oriented molecular imaging, in particular the diagnosis of cancer at an early stage. The detection of changes at the molecular level, which occur before typical symptoms can appear, will greatly contribute to the treatment of many diseases, especially cancer <sup>6</sup>. Early detection and non-invasively monitor of treatment are essential for increasing the survival rate; promising imaging agents in combination with advanced imaging modalities have significantly contributed to this field in the last few years <sup>10,49,60</sup>.

There are many hallmarks of cancer that can serve as appropriate imaging targets. Except the above mentioned (GLUTs, cathepsins, EGFRs, MMPs), other already in-use cancer hallmarks for FLI includes probes detecting  $\alpha_v\beta_3$  integrin, Her2 receptors, vascular endothelial growth factor receptor (VEGFR) <sup>61,62</sup>. These hallmarks are mostly cellular transporters, proteases, growth factors and extracellular matrix receptors, which are strongly associated with the development and progression of different cancer types <sup>63,64</sup>.

Another research area that greatly benefits from optical imaging is visualizing cell death. The first description about the association between cell death and cancer was raised in 1972 when Kerr *et al* described massive programmed cell death ("apoptosis", a Greek word describing falling leaves) following hormone withdrawal in hormone-dependent tumors where the cells were populating rapidly <sup>65</sup>. Many recent studies have implicated the importance of imaging cell death during tumor growth and invasion because apoptosis and necrosis are two hallmarks of most and perhaps all types of cancer. Moreover, when tumor tissues are undergoing aggressive progression, necrotic core is always found

---

during the tumor development<sup>66,67</sup>. Finally, optical imaging of cell death can be employed as a biomarker, e.g. for anti-tumor strategies to monitor therapeutic efficacy or evaluate drug toxicity<sup>68-70</sup>.

### 1.3.2 Near-infrared fluorescence imaging of cell death

Cell death has been classified into multiple types according to morphological, biochemical or functional differences. But it mainly consists of two distinctive forms, apoptosis and necrosis. Apoptosis appears to be an active process during the regulation of tissue size and the maintenance of a homeostatic status. On the contrary, necrosis is a degenerative phenomenon that always follows irreversible injury<sup>71</sup>. Morphologically, apoptotic cells exhibits condensation of the nuclear chromatin and cytoplasm, fragmentation of the nucleus, blebbing of the intact plasma membrane and budding of the whole cell to produce membrane-bounded bodies (known as apoptotic bodies) in which organelles are intact initially. These bodies are disposed of by adjacent cells without inflammation. Dying cells were originally catalogued as necrotic in a negative fashion. But recent studies reveal that necrotic cells exhibit some distinctive morphological features, including an increasingly transparent cytoplasm, swelling of organelles, minor ultra-structural modifications of the nucleus, increased cell volume and eventually disruption of the plasma membrane. However, their nuclei remain intact and can aggregate and accumulate in necrotic tissues. Biochemically, apoptosis has typical inter-nucleosome cleavage of DNA, which is distinguished from the random DNA degradation observed in necrosis<sup>72,73</sup>. Increased evidence indicated there are other types of cell death, e.g. autophagy, senescence and mitotic catastrophe<sup>74-76</sup>.

In the human body, eventually all cells will undergo cell death. Cell death is not only involved in many biological processes, e.g. to maintain homeostasis but also in various pathological conditions when cell death is unbalanced<sup>77</sup>. An elevated level of cell death is a general phenomenon in many diseases, e.g. traumatic brain injury, reperfusion injury, carotid artery injury, cerebral stroke, acute myocardial infarction, ischemia, rheumatoid arthritis, myelodysplastic syndromes and cancer<sup>66,78-81</sup>. Thus, imaging of cell death plays a pivotal role both physiologically and pathologically. Currently, many biomedical researchers are aiming to facilitate early diagnosis of cell death related diseases or therapies by accurately identify and monitor cell death *in vitro* and *in vivo*.

In order to facilitate accurate and non-invasive detection of cell death both *in vitro* and *in vivo*, current efforts in the NIR fluorescence imaging field are focused on developing targeted or activatable cell death fluorescent probes<sup>82</sup>. Table 1 lists a number of fluorescent probes described in recent studies about detection of apoptosis and necrosis.

Type of detecting agent	Type of targeted biomarker	Type of cell death	Ref.
Peptide DEVD	caspases	apoptosis	83-87
Peptide CQRPPR	histones	apoptosis	88,89
Peptide Duramycin	phosphatidylethanolamine	apoptosis & necrosis	90
Small molecular GSAO	Heat shock protein-90	apoptosis & necrosis	91,92
Small molecular Hoechst-IR	extracellular DNA	necrosis	93
Small molecular DDC	membrane depolarization and phospholipid scrambling	apoptosis	94
Small molecular ML-10	anionic phospholipid surfaces	apoptosis	95
Small molecular ZnDPA	phosphatidylserine	apoptosis & necrosis	96,97
Protein Annexin V	phosphatidylserine	apoptosis & necrosis	98-102
Protein C2A domain of Synaptotagmin-I	phosphatidylserine	apoptosis & necrosis	103
Protein Lactadherin	phosphatidylserine	apoptosis & necrosis	104,105
Antibody 3B9 mAb	La autoantigen	apoptosis & necrosis	106

**Table 1. Summary of fluorescent probes for detecting apoptosis and necrosis.**

As shown, the development of molecular imaging has generated a rich amount of NIR fluorescent probes, which has shed light on various cell death-related research fields. Most of these cell death fluorescent probes are either reacting with intracellular biomarkers, like cytosolic proteins, caspase enzymes, exposed DNA and mitochondrial membrane electronic potential, or targeting extracellular biomarkers, like plasma membrane phospholipids. The biomarkers of apoptosis and necrosis have aroused intensive research interests in monitoring therapeutic effects which are mediated with cell death, either in a pro- or anti-apoptotic manner. For example, caspases can be either activated or inhibited by small-molecule drugs. Important protein-to-protein interactions can be interfered with or mimicked by peptides or organic compounds. Moreover, unwanted proteins, like pro-survival factors in cancer cells, can be specifically down regulated by antisense or other strategies<sup>107-109</sup>. Because of the importance to accurately detect and characterize cell death in different stages of diseases, also because of the need to use cell death as a biomarker for anti-tumor strategies, there is still an urgent demand for the refined optical imaging of cell

---

death in diseases like cancer. Ultimately, new cell death imaging agents which can characterize the progression of apoptosis and necrosis with high sensitivity and high spatial resolution needs to be developed. Such imaging agent can eventually help to diagnose patients that are likely to develop certain disease where cell death is involved at an early stage and finally assess response to the therapy.

## 1.4 Outline of this thesis

The pre-clinical molecular imaging of detecting cancer and cell death is rapidly expanding at the research frontiers of current life sciences. The aim of the work included in this thesis was to explore the diverse application possibility of using NIR fluorescent probes with specific properties to visualize and characterize cancer and cell death.

In **Chapter 2**, we imaged breast tumors and their metastases using combinations of four NIR fluorescent probes that possess different optical imaging properties. In **Chapter 3** and **Chapter 4**, we studied two different NIR fluorescent probes, PSVue and a heat shock protein-90 alkylator (NIR fluorescent conjugate of GSAO), which can be used to non-invasively imaging cell death with different optical modules in a mouse model of traumatic brain injury. **Chapter 5** describes the NIR fluorescently tagged GSAO as a biomarker for monitoring breast cancer cell death after chemotherapy. Next, **Chapter 6** provides a general discussion about the advantages and the challenging that the state-of-art optical imaging is facing and shares some future prospective. This thesis ends with a summary that outlined the major findings of studies described in different chapters and explored the clinical implications (**Chapter 7**).

## References

1. Weissleder, R. & Mahmood, U. Molecular imaging. *Radiology* **219**, 316-333 (2001).
2. Mankoff, D.A. A definition of molecular imaging. *J Nucl Med* **48**, 18N, 21N (2007).
3. Shah, K. & Weissleder, R. Molecular optical imaging: applications leading to the development of present day therapeutics. *NeuroRx* **2**, 215-225 (2005).
4. Weissleder, R. & Pittet, M.J. Imaging in the era of molecular oncology. *Nature* **452**, 580-589 (2008).
5. Contag, C.H. In vivo pathology: seeing with molecular specificity and cellular resolution in the living body. *Annu Rev Pathol* **2**, 277-305 (2007).
6. Corsten, M.F. & Bennaghmouch, A. Optical characterization of arterial apoptosis. *Methods Mol Biol* **680**, 117-129 (2010).
7. Leblond, F., Davis, S.C., Valdes, P.A. & Pogue, B.W. Pre-clinical whole-body fluorescence imaging: Review of instruments, methods and applications. *J Photochem Photobiol B* **98**, 77-94 (2010).
8. Medarova, Z., Bonner-Weir, S., Lipes, M. & Moore, A. Imaging beta-cell death with a near-infrared probe. *Diabetes* **54**, 1780-1788 (2005).
9. James, M.L. & Gambhir, S.S. A molecular imaging primer: modalities, imaging agents, and applications. *Physiol Rev* **92**, 897-965 (2012).
10. Condeelis, J. & Weissleder, R. In vivo imaging in cancer. *Cold Spring Harb Perspect Biol* **2**, a003848 (2010).
11. Skotland, T. Molecular imaging: challenges of bringing imaging of intracellular targets into common clinical use. *Contrast Media Mol Imaging* **7**, 1-6 (2012).
12. Choudhury, R.P. & Fisher, E.A. Molecular Imaging in Atherosclerosis, Thrombosis, and Vascular Inflammation. *Arterioscler Thromb Vasc Biol*, 983-991 (2009).
13. Jaffer, F.A. & Weissleder, R. Seeing within: molecular imaging of the cardiovascular system. *Circ Res* **94**, 433-445 (2004).
14. Barbet, J., et al. Radioimmunodetection of medullary thyroid carcinoma using indium-111 bivalent hapten and anti-CEA x anti-DTPA-indium bispecific antibody. *J Nucl Med* **39**, 1172-1178 (1998).
15. Weissleder, R., Tung, C.H., Mahmood, U. & Bogdanov, A., Jr. In vivo imaging of tumors with protease-activated near-infrared fluorescent probes. *Nat Biotechnol* **17**, 375-378 (1999).
16. Wolters, S.L., Corsten, M.F., Reutelingsperger, C.P., Narula, J. & Hofstra, L. Cardiovascular molecular imaging of apoptosis. *Eur J Nucl Med Mol Imaging* **34 Suppl 1**, S86-98 (2007).
17. Weissleder, R. & Ntziachristos, V. Shedding light onto live molecular targets. *Nat Med* **9**, 123-128 (2003).
18. Brogan, J., et al. Imaging molecular pathways: reporter genes. *Radiat Res* **177**, 508-513 (2012).
19. Choudhury, R.P., Fuster, V. & Fayad, Z.A. Molecular, cellular and functional imaging of atherothrombosis. *Nat Rev Drug Discov* **3**, 913-925 (2004).
20. Rudd, J.H., et al. Imaging atherosclerotic plaque inflammation with [18F]-fluorodeoxyglucose positron emission tomography. *Circulation* **105**, 2708-2711 (2002).
21. Ke, S., et al. Near-infrared optical imaging of epidermal growth factor receptor in breast cancer xenografts. *Cancer Res* **63**, 7870-7875 (2003).
22. Hsu, A.R., et al. In vivo near-infrared fluorescence imaging of integrin alphavbeta3 in an orthotopic glioblastoma model. *Mol Imaging Biol* **8**, 315-323 (2006).
23. Kovar, J.L., Volcheck, W., Sevick-Muraca, E., Simpson, M.A. & Olive, D.M. Characterization and performance of a near-infrared 2-deoxyglucose optical imaging agent for mouse cancer models. *Anal Biochem* **384**, 254-262 (2009).
24. Bremer, C., Tung, C.H. & Weissleder, R. In vivo molecular target assessment of matrix metalloproteinase inhibition. *Nat Med* **7**, 743-748 (2001).
25. Zorko, M. & Langel, U. Cell-penetrating peptides: mechanism and kinetics of cargo delivery. *Adv Drug Deliv Rev* **57**, 529-545 (2005).
26. Jiang, T., et al. Tumor imaging by means of proteolytic activation of cell-penetrating peptides. *Proc Natl Acad Sci U S A* **101**, 17867-17872 (2004).
27. Olson, E.S., et al. In vivo characterization of activatable cell penetrating peptides for targeting protease activity in cancer. *Integr Biol (Camb)* **1**, 382-393 (2009).
28. Olson, E.S., et al. Activatable cell penetrating peptides linked to

- nanoparticles as dual probes for in vivo fluorescence and MR imaging of proteases. *Proc Natl Acad Sci U S A* (2010).
29. Luke, G.P., Yeager, D. & Emelianov, S.Y. Biomedical applications of photoacoustic imaging with exogenous contrast agents. *Ann Biomed Eng* **40**, 422-437 (2011).
  30. Levenson, R.M., Lynch, D.T., Kobayashi, H., Backer, J.M. & Backer, M.V. Multiplexing with multispectral imaging: from mice to microscopy. *ILAR J* **49**, 78-88 (2008).
  31. Hilderbrand, S.A. & Weissleder, R. Near-infrared fluorescence: application to in vivo molecular imaging. *Curr Opin Chem Biol* **14**, 71-79 (2010).
  32. Thorek, D.L. & Grimm, J. Enzymatically activatable diagnostic probes. *Curr Pharm Biotechnol* **13**, 523-536 (2012).
  33. Anderson, C.J., *et al.* Design of targeted cardiovascular molecular imaging probes. *J Nucl Med* **51 Suppl 1**, 3S-17S (2010).
  34. Kaijzel, E.L., van der Pluijm, G. & Lowik, C.W. Whole-body optical imaging in animal models to assess cancer development and progression. *Clin Cancer Res* **13**, 3490-3497 (2007).
  35. Ntziachristos, V., Bremer, C., Graves, E.E., Ripoll, J. & Weissleder, R. In vivo tomographic imaging of near-infrared fluorescent probes. *Mol Imaging* **1**, 82-88 (2002).
  36. Razansky, D., Buehler, A. & Ntziachristos, V. Volumetric real-time multispectral optoacoustic tomography of biomarkers. *Nat Protoc* **6**, 1121-1129 (2011).
  37. Luke, G.P., Yeager, D. & Emelianov, S.Y. Biomedical applications of photoacoustic imaging with exogenous contrast agents. *Ann Biomed Eng* **40**, 422-437 (2012).
  38. Hutchens, M. & Luker, G.D. Applications of bioluminescence imaging to the study of infectious diseases. *Cell Microbiol* **9**, 2315-2322 (2007).
  39. Banaszynski, L.A., Sellmyer, M.A., Contag, C.H., Wandless, T.J. & Thorne, S.H. Chemical control of protein stability and function in living mice. *Nat Med* **14**, 1123-1127 (2008).
  40. Luker, K.E. & Luker, G.D. Applications of bioluminescence imaging to antiviral research and therapy: multiple luciferase enzymes and quantitation. *Antiviral Res* **78**, 179-187 (2008).
  41. Wang, G., *et al.* Overview of bioluminescence tomography--a new molecular imaging modality. *Front Biosci* **13**, 1281-1293 (2008).
  42. Ciampricotti, M., *et al.* Development of metastatic HER2(+) breast cancer is independent of the adaptive immune system. *J Pathol* (2010).
  43. Bharadwaj, A.G., *et al.* Spontaneous metastasis of prostate cancer is promoted by excess hyaluronan synthesis and processing. *Am J Pathol* **174**, 1027-1036 (2009).
  44. Bhardwaj, V., *et al.* PLGA nanoparticles stabilized with cationic surfactant: safety studies and application in oral delivery of paclitaxel to treat chemical-induced breast cancer in rat. *Pharm Res* **26**, 2495-2503 (2009).
  45. Prescher, J.A. & Contag, C.H. Guided by the light: visualizing biomolecular processes in living animals with bioluminescence. *Curr Opin Chem Biol* **14**, 80-89 (2010).
  46. Rice, B.W. & Contag, C.H. The importance of being red. *Nat Biotechnol* **27**, 624-625 (2009).
  47. Keereweer, S., *et al.* Optical Image-guided Surgery-Where Do We Stand? *Mol Imaging Biol* (2010).
  48. Ghoroghchian, P.P., Therien, M.J. & Hammer, D.A. In vivo fluorescence imaging: a personal perspective. *Wiley Interdiscip Rev Nanomed Nanobiotechnol* **1**, 156-167 (2009).
  49. Weissleder, R. A clearer vision for in vivo imaging. *Nat Biotechnol* **19**, 316-317 (2001).
  50. Murakami, K., *et al.* Cold injury in mice: a model to study mechanisms of brain edema and neuronal apoptosis. *Prog Neurobiol* **57**, 289-299 (1999).
  51. Fujiwara, M., Mizukami, T., Suzuki, A. & Fukamizu, H. Sentinel lymph node detection in skin cancer patients using real-time fluorescence navigation with indocyanine green: preliminary experience. *J Plast Reconstr Aesthet Surg* **13**, 1-6 (2008).
  52. Muller, J., Wunder, A. & Licha, K. Optical imaging. *Recent Results Cancer Res* **187**, 221-246 (2013).
  53. Ntziachristos, V. & Razansky, D. Optical and opto-acoustic imaging. *Recent Results Cancer Res* **187**, 133-150 (2013).
  54. Histed, S.N., *et al.* Review of functional/

- anatomical imaging in oncology. *Nucl Med Commun* **33**, 349-361 (2012).
55. Kovar, J.L., Volcheck, W.M., Chen, J. & Simpson, M.A. Purification method directly influences effectiveness of an epidermal growth factor-coupled targeting agent for noninvasive tumor detection in mice. *Anal Biochem* **361**, 47-54 (2007).
  56. Xie, B.W., *et al.* Dual-wavelength imaging of tumor progression by activatable and targeting near-infrared fluorescent probes in a bioluminescent breast cancer model. *PLoS One* **7**, e31875 (2012).
  57. Chen, J., *et al.* Near-infrared fluorescent imaging of matrix metalloproteinase activity after myocardial infarction. *Circulation* **111**, 1800-1805 (2005).
  58. Tung, C.H., Bredow, S., Mahmood, U. & Weissleder, R. Preparation of a cathepsin D sensitive near-infrared fluorescence probe for imaging. *Bioconjug Chem* **10**, 892-896 (1999).
  59. Bremer, C., Bredow, S., Mahmood, U., Weissleder, R. & Tung, C.H. Optical imaging of matrix metalloproteinase-2 activity in tumors: feasibility study in a mouse model. *Radiology* **221**, 523-529 (2001).
  60. Jaffer, F.A. & Weissleder, R. Molecular imaging in the clinical arena. *JAMA* **293**, 855-862 (2005).
  61. Kwon, H., *et al.* In vitro and in vivo imaging of prostate cancer angiogenesis using anti-vascular endothelial growth factor receptor 2 antibody-conjugated quantum dot. *Korean J Radiol* **14**, 30-37 (2013).
  62. Ardeshirpour, Y., *et al.* In vivo fluorescence lifetime imaging monitors binding of specific probes to cancer biomarkers. *PLoS One* **7**, e31881 (2012).
  63. Hanahan, D. & Weinberg, R.A. The hallmarks of cancer. *Cell* **100**, 57-70 (2000).
  64. Czernin, J., Weber, W.A. & Herschman, H.R. Molecular imaging in the development of cancer therapeutics. *Annu Rev Med* **57**, 99-118 (2006).
  65. Walker, N.I., Harmon, B.V., Gobe, G.C. & Kerr, J.F. Patterns of cell death. *Methods Achiev Exp Pathol* **13**, 18-54 (1988).
  66. De Saint-Hubert, M., Prinsen, K., Mortelmans, L., Verbruggen, A. & Mottaghy, F.M. Molecular imaging of cell death. *Methods* **48**, 178-187 (2009).
  67. Haberkorn, U., Markert, A., Mier, W., Askoxylakis, V. & Altmann, A. Molecular imaging of tumor metabolism and apoptosis. *Oncogene* (2011).
  68. Darzynkiewicz, Z. Apoptosis in antitumor strategies: modulation of cell cycle or differentiation. *J Cell Biochem* **58**, 151-159 (1995).
  69. Fischer, U. & Schulze-Osthoff, K. Apoptosis-based therapies and drug targets. *Cell Death Differ* **12 Suppl 1**, 942-961 (2005).
  70. Fischer, U., Janssen, K. & Schulze-Osthoff, K. Cutting-edge apoptosis-based therapeutics: a panacea for cancer? *BioDrugs* **21**, 273-297 (2007).
  71. Galluzzi, L., *et al.* Cell death modalities: classification and pathophysiological implications. *Cell Death Differ* **14**, 1237-1243 (2007).
  72. Vaux, D.L. & Korsmeyer, S.J. Cell death in development. *Cell* **96**, 245-254 (1999).
  73. Vandenabeele, P., Galluzzi, L., Vanden Berghe, T. & Kroemer, G. Molecular mechanisms of necroptosis: an ordered cellular explosion. *Nat Rev Mol Cell Biol* **11**, 700-714 (2010).
  74. Kroemer, G. & Levine, B. Autophagic cell death: the story of a misnomer. *Nat Rev Mol Cell Biol* **9**, 1004-1010 (2008).
  75. Kuilman, T., Michaloglou, C., Mooi, W.J. & Peeper, D.S. The essence of senescence. *Genes Dev* **24**, 2463-2479 (2010).
  76. Okada, H. & Mak, T.W. Pathways of apoptotic and non-apoptotic death in tumour cells. *Nat Rev Cancer* **4**, 592-603 (2004).
  77. Lee, M.J., Wang, K., Kim, I.S., Lee, B.H. & Han, H.S. Molecular imaging of cell death in an experimental model of Parkinson's disease with a novel apoptosis-targeting peptide. *Mol Imaging Biol* **14**, 147-155 (2011).
  78. Kelly, G.L. & Strasser, A. The essential role of evasion from cell death in cancer. *Adv Cancer Res* **111**, 39-96 (2011).
  79. Thompson, C.B. Apoptosis in the pathogenesis and treatment of disease. *Science* **267**, 1456-1462 (1995).
  80. Ekert, P.G. & Vaux, D.L. Apoptosis and the immune system. *Br Med Bull* **53**, 591-603 (1997).
  81. Gaetz, M. The neurophysiology of brain

- 
- injury. *Clin Neurophysiol* **115**, 4-18 (2004).
82. Herschman, H.R. Molecular imaging: looking at problems, seeing solutions. *Science* **302**, 605-608 (2003).
83. Joseph, J., Seervi, M., Sobhan, P.K. & Retnabai, S.T. High throughput ratio imaging to profile caspase activity: potential application in multiparameter high content apoptosis analysis and drug screening. *PLoS One* **6**, e20114 (2011).
84. Keese, M., Yagublu, V., Schwenke, K., Post, S. & Bastiaens, P. Fluorescence lifetime imaging microscopy of chemotherapy-induced apoptosis resistance in a syngenic mouse tumor model. *Int J Cancer* **126**, 104-113 (2010).
85. Barnett, E.M., Zhang, X., Maxwell, D., Chang, Q. & Piwnica-Worms, D. Single-cell imaging of retinal ganglion cell apoptosis with a cell-penetrating, activatable peptide probe in an in vivo glaucoma model. *Proc Natl Acad Sci U S A* **106**, 9391-9396 (2009).
86. Maxwell, D., Chang, Q., Zhang, X., Barnett, E.M. & Piwnica-Worms, D. An improved cell-penetrating, caspase-activatable, near-infrared fluorescent peptide for apoptosis imaging. *Bioconjug Chem* **20**, 702-709 (2009).
87. Debunne, M., et al. In vitro and ex vivo evaluation of smart infra-red fluorescent caspase-3 probes for molecular imaging of cardiovascular apoptosis. *Int J Mol Imaging* **2011**, 413290 (2011).
88. Wang, K., et al. In vivo imaging of tumor apoptosis using histone H1-targeting peptide. *J Control Release* **148**, 283-291 (2010).
89. Paidassi, H., et al. C1q binds phosphatidylserine and likely acts as a multiligand-bridging molecule in apoptotic cell recognition. *J Immunol* **180**, 2329-2338 (2008).
90. Hanahan, D. & Weinberg, R.A. Hallmarks of cancer: the next generation. *Cell* **144**, 646-674 (2011).
91. Park, D., et al. Noninvasive imaging of cell death using an Hsp90 ligand. *J Am Chem Soc* **133**, 2832-2835 (2011).
92. Xie, B.W., et al. Optical imaging of cell death in traumatic brain injury using a heat shock protein-90 alkylator. *Cell Death Dis* **4**, e473 (2013).
93. Dasari, M., et al. Hoechst-IR: an imaging agent that detects necrotic tissue in vivo by binding extracellular DNA. *Org Lett* **12**, 3300-3303 (2010).
94. Reshef, A., et al. Targeting cell death in vivo in experimental traumatic brain injury by a novel molecular probe. *J Neurotrauma* **25**, 569-580 (2008).
95. Cohen, A., et al. From the Gla domain to a novel small-molecule detector of apoptosis. *Cell Res* **19**, 625-637 (2009).
96. Smith, B.A., et al. In vivo targeting of cell death using a synthetic fluorescent molecular probe. *Apoptosis* **16**, 722-731 (2011).
97. Smith, B.A., et al. Multicolor fluorescence imaging of traumatic brain injury in a cryolesion mouse model. *ACS Chem Neurosci* **3**, 530-537 (2012).
98. Schellenberger, E.A., et al. Optical imaging of apoptosis as a biomarker of tumor response to chemotherapy. *Neoplasia* **5**, 187-192 (2003).
99. Stafford, J.H. & Thorpe, P.E. Increased exposure of phosphatidylethanolamine on the surface of tumor vascular endothelium. *Neoplasia* **13**, 299-308 (2011).
100. Manning, H.C., et al. Molecular imaging of therapeutic response to epidermal growth factor receptor blockade in colorectal cancer. *Clin Cancer Res* **14**, 7413-7422 (2008).
101. Dasgupta, S.K., Guchhait, P. & Thiagarajan, P. Lactadherin binding and phosphatidylserine expression on cell surface-comparison with annexin A5. *Transl Res* **148**, 19-25 (2006).
102. Petrovsky, A., Schellenberger, E., Josephson, L., Weissleder, R. & Bogdanov, A., Jr. Near-infrared fluorescent imaging of tumor apoptosis. *Cancer Res* **63**, 1936-1942 (2003).
103. Alam, I.S., Neves, A.A., Witney, T.H., Boren, J. & Brindle, K.M. Comparison of the C2A domain of synaptotagmin-I and annexin-V as probes for detecting cell death. *Bioconjug Chem* **21**, 884-891 (2010).
104. Smith, B.A. & Smith, B.D. Biomarkers and molecular probes for cell death imaging and targeted therapeutics. *Bioconjug Chem* **23**, 1989-2006 (2012).
105. Hou, J., et al. Lactadherin functions as a probe for phosphatidylserine exposure

- and as an anticoagulant in the study of stored platelets. *Vox Sang* **100**, 187-195 (2010).
106. Al-Ejeh, F., Darby, J.M. & Brown, M.P. The La autoantigen is a malignancy-associated cell death target that is induced by DNA-damaging drugs. *Clin Cancer Res* **13**, 5509s-5518s (2007).
107. Favalaro, B., Allocati, N., Graziano, V., Di Ilio, C. & De Laurenzi, V. Role of apoptosis in disease. *Aging (Albany NY)* **4**, 330-349 (2012).
108. Olsson, M. & Zhivotovsky, B. Caspases and cancer. *Cell Death Differ* **18**, 1441-1449 (2011).
109. Vorburger, S.A., Pataer, A., Swisher, S.G. & Hunt, K.K. Genetically targeted cancer therapy: tumor destruction by PKR activation. *Am J Pharmacogenomics* **4**, 189-198 (2004).





## CHAPTER TWO

# Dual-Wavelength Imaging of Tumor Progression by Activatable and Targeting Near-Infrared Fluorescent Probes in a Bioluminescent Breast Cancer Model

Based on

Xie BW, Mol IM, Keereweer S, van Beek ER, Que I, Snoeks TJ,  
Chan A, Kaijzel EL, Löwik CW. *PLoS One*. 2012; 7(2):e31875.



## Abstract

Bioluminescence imaging (BLI) has shown its appeal as a sensitive technique for *in vivo* whole body optical imaging. However, the development of injectable tumor-specific near-infrared fluorescent (NIRF) probes makes fluorescence imaging (FLI) a promising alternative to BLI in situations where BLI cannot be used or is unwanted (e.g. spontaneous transgenic tumor models, or syngeneic mice to study immune effects).

In this study, we addressed the questions whether it is possible to detect tumor progression using FLI with appropriate sensitivity, and if there is a good correlation between FLI and BLI measurements. In addition, we explored the possibilities to simultaneously detect multiple tumor characteristics by dual-wavelength FLI (~700 and ~800 nm) in combination with spectral unmixing. Using a luciferase-expressing 4T1-luc2 mouse breast cancer model and combinations of activatable and targeting NIRF probes, we showed that the activatable NIRF probes (ProSense680 and MMPsense680) and the targeting NIRF probes (IRDye 800CW 2-DG and IRDye 800CW EGF) were either activated by or bound to 4T1-luc2 cells. *In vivo*, we implanted 4T1-luc2 cells orthotopically in nude mice and were able to follow tumor progression longitudinally both by BLI and dual-wavelength FLI. We were able to reveal different probe signals within the tumor, which co-localized with the immuno-staining. Moreover, we observed a linear correlation between the internal BLI signals and the FLI signals obtained from the NIRF probes. Finally, we could detect pulmonary metastases both by BLI and FLI, and confirmed their presence histologically.

Taken together, these data suggest that dual-wavelength FLI is a feasible approach to simultaneously detect different features of one tumor and to follow tumor progression with high specificity and sensitivity. This study may open up new perspectives for the detection of tumors and metastases in various experimental models and could also have clinical applications, such as image-guided surgery.

---

## Introduction

Both bioluminescence imaging (BLI) and fluorescence imaging (FLI) are widely used optical modalities for non-invasive detection of tumor progression in small animals. BLI is appealing for *in vivo* whole body imaging because of its exceptional sensitivity and almost negligible bioluminescent background<sup>1-3</sup>. However, under certain circumstances, BLI is not applicable. For example, BLI cannot be employed in tumor models lacking expression of bioluminescent reporters, such as in spontaneous- or chemical-induced cancer models. Moreover, the introduction of a foreign reporter protein, such as luciferase, may induce an immune response directed against the reporter protein itself in syngeneic mouse models of cancer<sup>4-8</sup>. Finally, for clinical applications, such as image-guided surgery<sup>9</sup>, BLI is also not applicable as it requires genetic modification of the targeted cells.

Recent advances in the development of tumor-specific injectable near-infrared fluorescent (NIRF) probes make FLI a promising alternative for BLI. The use of NIRF probes has several advantages. For example, in the near-infrared (NIR) region (600-900 nm), the absorption coefficient of major light absorbers in tissues (e.g., hemoglobin and water) is minimal, which improves the photon penetration depth. Moreover, the autofluorescence of tissues in the NIR region is minimal, which provides a high contrast between target and background fluorescence<sup>10-12</sup>. Currently, there are two main types of commercially available NIRF probes. Firstly, the so-called protease-activatable probes, which can visualize tumors via activation by enzymes, such as matrix metalloproteinases (MMPs) or cathepsins, which are over expressed by various tumors and their surrounding stroma<sup>13-18</sup>. Secondly, targeting probes which can recognize tumor tissues by binding to specific membrane targets like glucose transporters (GLUTs) or epidermal growth factor receptors (e.g., EGFR, HER2)<sup>19-22</sup>. These transporters and cell-surface receptors are over expressed in many different tumor cells because of their elevated glycolysis and proliferation<sup>23-27</sup>. These enzyme activatable and targeting probes were labeled with a 700 nm or 800 nm fluorophore, respectively, enabling their visualization simultaneously using dual-wavelength imaging. This method, with the introduction of spectral unmixing, extends the number of measurements made in the same animal and offers more accurate biologic observations *in vivo*<sup>28</sup>.

The aim of the present study was to explore the use of FLI as a viable and sensitive alternative to BLI. We also investigated the possibilities to simultaneously detect multiple tumor characteristics by using FLI at two wavelengths in combination with spectral unmixing. For this, we employed different combinations of activatable and targeting NIRF probes in a luciferase-expressing 4T1-luc2 mouse breast cancer model and assessed the correlation between FLI and BLI measurements.

## Materials and Methods

### Ethics statement

All animal experiments were approved for animal health, ethics, and research by the Animal Welfare Committee of Leiden University Medical Center, the Netherlands (Approval DEC number 09050). All animals were five week-old BALB/c *nu/nu* female mice (Charles River Laboratories, France) and received humane care and maintenance in compliance with the “Code of Practice Use of Laboratory Animals in Cancer Research” (Inspectie W&V, July 1999).

### Cell culture

The mouse mammary gland cancer cell line, 4T1-luc2, expressing a codon-optimized luciferase gene (*luc2*) was obtained from Caliper Life Sciences (Hopkinton, MA). This cell line has been shown to spontaneously produce highly metastatic tumors which can metastasize to the lung, liver and lymph nodes while the primary tumor is growing in situ<sup>2,29,30</sup>. The cells were maintained in complete RPMI-1640 Medium (Gibco, Invitrogen, Carlsbad, CA).

### *In vitro* cell-based fluorescent assays

The specificities and sensitivities of ProSense680, MMPsense680 (Perkin Elmer Inc., Boston, MA), IRDye 800CW 2-DG and IRDye 800CW EGF (LI-COR Biosciences, Lincoln, NE) to detect 4T1-luc2 cells were assessed in cell-based assays. For dose-dependent experiments,  $1 \times 10^4$  cells were seeded in 96-well plates and maintained in RPMI-1640 medium at 37°C, in a humidified incubator containing 5% CO<sub>2</sub>. After overnight adhesion, probes with different concentrations were added to the cell culture: 0 to 45 nM for ProSense680 and MMPsense680, and 0 to 10 μM for IRDye 800CW 2-DG and IRDye 800CW EGF. The cells were incubated with the activatable probes (ProSense680 and MMPsense680) for 24 hours. Cells were washed twice with phosphate buffered saline (PBS) before imaging, to remove unbound dye. For the targeting probes (IRDye 800CW 2-DG and IRDye 800CW EGF), cells were starved for two hours in serum-free low-glucose DMEM (Gibco, Invitrogen, Carlsbad, CA) to elevate GLUT-1 or EGFR expression levels. Subsequently, the IRDye 800CW 2-DG was added and the cells were incubated for an additional two hours. For the IRDye 800CW EGF, the cells were incubated with the probe for 15 minutes. Both assays were then stopped and fixed for 20 minutes with 4% formaldehyde. Cells were subsequently washed twice with PBS to remove unbound probes. For cell amount-dependent experiment, 4T1-luc2 cells were seeded with a serial of cell dilutions, from  $2 \times 10^4$  to 39 cells/well. After overnight adhesion, cells were incubated either with 22.5nM

---

ProSense680 or with 100nM IRDye 800CW EGF, as described previously. The 96-well plates were scanned with the Odyssey Infrared Imaging System (LI-COR Biosciences, Lincoln, NE), at the 700nm and 800nm channels.

## Microscopic analysis

4T1-luc2 cells were cultivated and incubated with probes following the procedure described previously. At the end of probe incubation, the growth medium was discarded and the cells were washed with pre-warmed fresh medium. The carbocyanine dye DiI, and Hoechst 33342 (Invitrogen, Carlsbad, CA) were then added to stain the cell membrane and nucleus, respectively, according to the manufacturer protocol. Samples with ProSense680 or MMPsense680 were imaged with a confocal TCS SP5 microscope (Leica, Mannheim, Germany) using appropriate laser power. Samples with IRDye 800CW 2-DG or IRDye 800CW EGF were imaged with the Nuance multispectral imaging system (Cri, Inc., Woburn, MA) using a Xenon 75W lamp followed by spectral unmixing<sup>31</sup>.

## *In vivo* optical imaging

To follow tumor growth longitudinally,  $2 \times 10^4$  4T1-luc2 cells were injected subcutaneously into the lateral thoracic mammary fat pad (MFP) of the nude mice. For the tumor cell detection limit experiment, different numbers of 4T1-luc2 cells ( $1 \times 10^5$ ,  $5 \times 10^4$ ,  $2.5 \times 10^4$  and  $1.25 \times 10^4$ ) were injected into four upper thoracic MFPs. The combination of ProSense680 and IRDye 800CW EGF was injected the day before measurement (day 0 and day 3). Throughout tumor inoculation and imaging procedures, the animals were anesthetized with isoflurane. For *in vivo* BLI, 150mg/kg of D-luciferin solution (SynChem, Inc., Elk Grove Village, IL) in PBS in a total volume of 50 $\mu$ L was injected intraperitoneally 10 minutes prior to imaging. The animals were imaged with the IVIS 100 imaging system (Caliper Life Sciences, Hopkinton, MA). Regions of interest (ROI) from displayed images were selected to cover the tumor regions and quantified with Living Image software from Caliper Life Sciences, using protocols as described previously<sup>32</sup>.

For FLI, images were taken with the Maestro imaging system (Cri, Inc., Woburn, MA), 24-hour after probe injection of either the combination of ProSense680 (1.33nmol/100 $\mu$ L in PBS) and IRDye 800CW 2-DG (10nmol/100 $\mu$ L in PBS), or the combination of MMPsense680 (1.33nmol/100 $\mu$ L in PBS) and IRDye 800CW EGF (1.33nmol/100 $\mu$ L in PBS). The probes were injected intravenously in the tail vein. Each mouse was imaged together with a control mouse without probe injection in order to perform spectral unmixing<sup>31</sup>. After spectral unmixing, ROI from displayed images were selected as described before. The tumor-to-background ratio (TBR) was calculated by dividing the mean fluorescence values of the tumor region by

the mean fluorescence values of the tumor border areas (Fig. 1).

For *ex vivo* BLI, 150mg/kg D-luciferin solution was injected into the mice five minutes prior to necropsy. Tissues of interest were excised and re-imaged for BLI and FLI signals. After imaging, excised tissues were subsequently prepared for standard histopathology analysis.

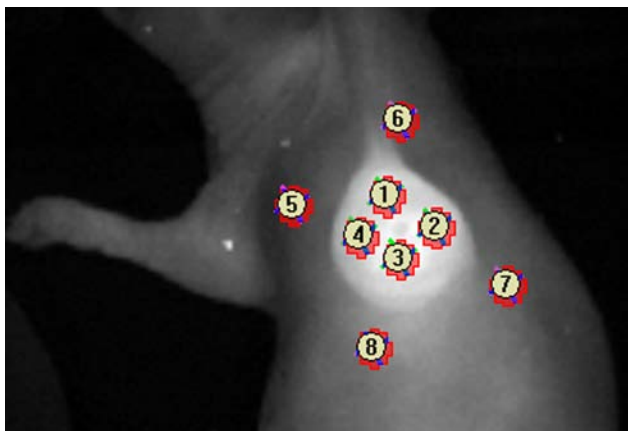


**Figure 1. Schematic representation of the localization of the signal intensity areas used to calculate TBRs.** The TBR was calculated by dividing the mean fluorescence intensity of four areas, of the same size, located inside the tumor region (1-4) by the mean fluorescence intensity of four areas, located approximately 5 mm outside the tumor region (background fluorescence) (5-8).

## Histological analysis

Primary tumors and possible metastatic tissues (lungs) were surgically removed and processed, either for paraffin-embedding or for cryosectioning. 8  $\mu\text{m}$  slices of excised tumor tissues were scanned on the Odyssey machine using the 700nm and 800nm channels. The tumor sections containing ProSense680 and IRDye 800CW 2-DG were processed for CathpsinB (Calbiochem, Darmstadt, Germany) and GLUT-1 (abcam, San Francisco, CA) antibody staining. Sections containing MMPsense680 and IRDye 800CW EGF were used for MMP-9 (Santa Cruz Biotechnology, Inc., Heidelberg, Germany) and EGFR (abcam, San Francisco, CA) immuno-staining, respectively. Finally, the presence of metastases in lungs was confirmed by a pathologist in hematoxylin and eosin (H&E) stained sections.

## Statistical analysis

In order to analyze the correlation of FLI signals obtained from the NIRF probes with BLI signals from tumor cells, Pearson's *r* test was applied for statistical analysis, as a descriptor of the degree of linear association.

## Results

### *In vitro* characterization of different activatable and targeting NIRF probes

Activation of ProSense680 and MMPsense680, and binding of IRDye 800CW 2-DG and IRDye 800CW EGF by 4T1-luc2 cells were examined. Activation/binding assays, using a fixed initial number of cells incubated with different probe concentrations, were performed. A dose-dependent increase in the fluorescent signal intensity was found at increasing concentrations of each probe (Fig. 2A and B). As shown by microscopic analysis (Fig. 2C and D), the fluorescent signal (red) representing ProSense680 and IRDye 800CW 2-DG was found localized specifically in the cytosol of the cells. Similar results were found with MMPsense680 and IRDye 800CW EGF (data not shown).

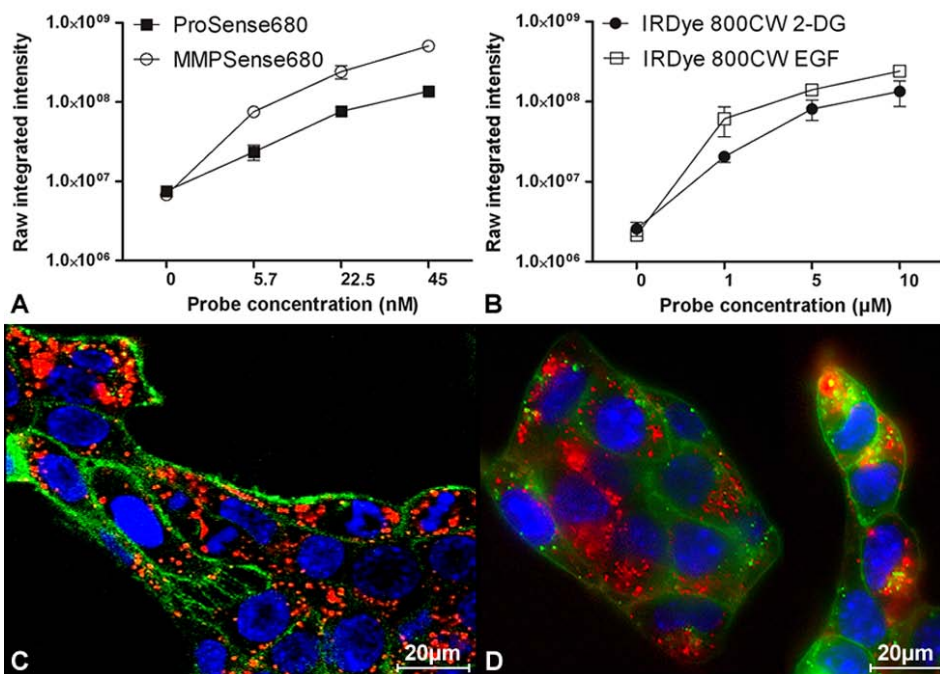


**Figure 2. *In vitro* NIRF probe activation/binding assays.** 4T1-luc2 breast cancer cells were seeded in 96-well plates and incubated with increasing concentrations of ProSense680 or MMPsense680 (A) and IRDye 800CW EGF or IRDye 800CW 2-DG (B) and were subsequently imaged. Intracellular accumulation of ProSense680 (45nM; 24h incubation) was visualized by confocal microscopy (C). Intracellular accumulation of IRDye 800CW 2-DG (10μM; 2h incubation) was visualized by the Nuance multispectral imaging system (D). NIRF probes, cell nuclei and membranes are indicated in red, blue and green, respectively.

## Sensitivity of FLI versus BLI measurements *in vitro* and *in vivo*

In order to assess the sensitivity of FLI versus BLI measurements, cell limit detection assays were performed. *In vitro*, as shown in Fig. 3, both the bioluminescent and fluorescent signals elevated with increasing cell numbers. However, the sensitivity of BLI was found to be superior to that of FLI. In our study, the cell detection limit for BLI was  $<39$  cells/well ( $P < 0.001$ ), 625 cells/well ( $P < 0.05$ ) for ProSense680 and 1,250 cells/well ( $P < 0.05$ ) for IRDye 800CW EGF.

*In vivo*, cell detection limit experiments were performed after orthotopical tumor cell implantation. ProSense680 and IRDye 800CW EGF were used for dual-wavelength FLI, in comparison to BLI. As shown in Fig. 4A and 4C, one day after implantation all MFP cell implants, including the ones with the lowest number ( $1.25 \times 10^4$  cells), were detectable with BLI. However, using ProSense680 and IRDye 800CW EGF, the lowest detectable number for FLI was  $5 \times 10^5$  cells (Fig. 4B and 4C). Moreover, four days after implantation, all MFP cell implants could be detected both by BLI and FLI (Fig. 4D-F).

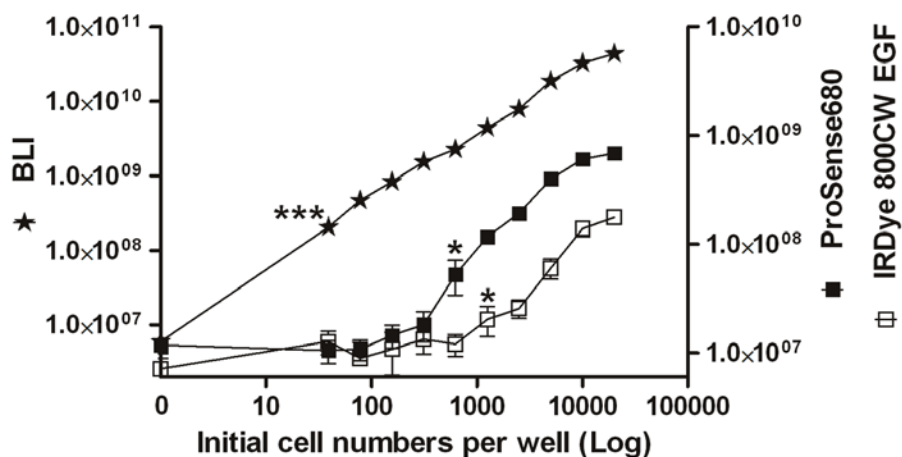


**Figure 3.** *In vitro* detection of different cell numbers by BLI and FLI. 4T1-luc2 cells with an initial density from 39 to  $2 \times 10^4$  cells per well were seeded in three 96-well plates. The next day, cells in one plate were used for BLI measurement. Cells in the other two plates were incubated with either ProSense680 or with IRDye 800CW EGF, and then used for FLI measurements. The star signs indicated the first significant difference between signals from wells without and with cells.

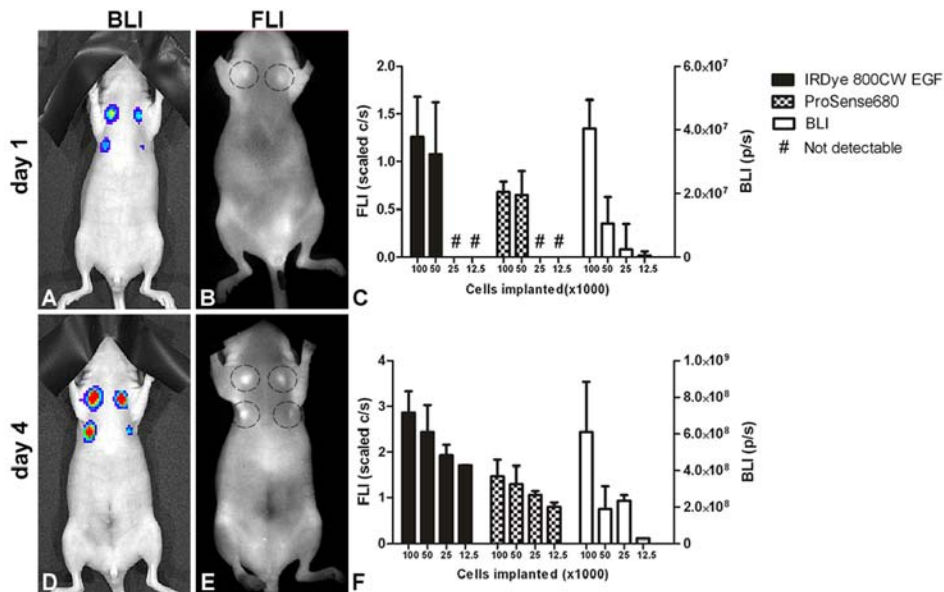


**Figure 4. In vivo tumor cell detection limit experiment.** Different numbers of 4T1-luc2 cells were implanted orthotopically into nude mice. The cell amounts implanted were  $1 \times 10^5$ ,  $5 \times 10^4$ ,  $2.5 \times 10^4$  and  $1.25 \times 10^4$ , as indicated by the injection sites on the upper left, upper right, lower left and lower right positions of each mouse, respectively. Days 1 and 4 BLI signals obtained are shown by panels A and D. The combination of ProSense680 and IRDye 800CW EGF probe was injected 24h prior FLI measurement. The representative FLI pictures (B, E) were from IRDye 800CW EGF probe. Quantitative analysis of the BLI and FLI measurements illustrated the corresponding tumor growth pattern (C, F).

## In vivo detection of tumor progression

The ability of the four different NIRF probes to detect tumor progression was examined in a mouse model of breast cancer. Both BLI and FLI signals were measured at different time points of tumor progression (day 4 to 18). Dual-wavelength images of MMPsense680 and IRDye 800CW EGF, at different time points of tumor progression, were shown in Fig. 5. As expected, tumors could be detected on day 4 after cell implantation, both by BLI and FLI. The tumor signal intensity increased up to day 18, the final day of the experiment (Fig. 5A-C, E-G and I-K). Some fluorescence was observed in the bladder on day 4 (Fig. 5E and I), due to the excretion of the probes into the urine. However, the bladder signal was invisible at later time points of tumor progression, as at these stages the bladder signal is superseded by the stronger signal from the tumor. At the end of the experiment, the mice were sacrificed and thoracic cavities were exposed and reimaged to reveal possible metastases. As shown in (Fig. 5D, H, L), both BLI and FLI signals were found at corresponding sites in the lungs.

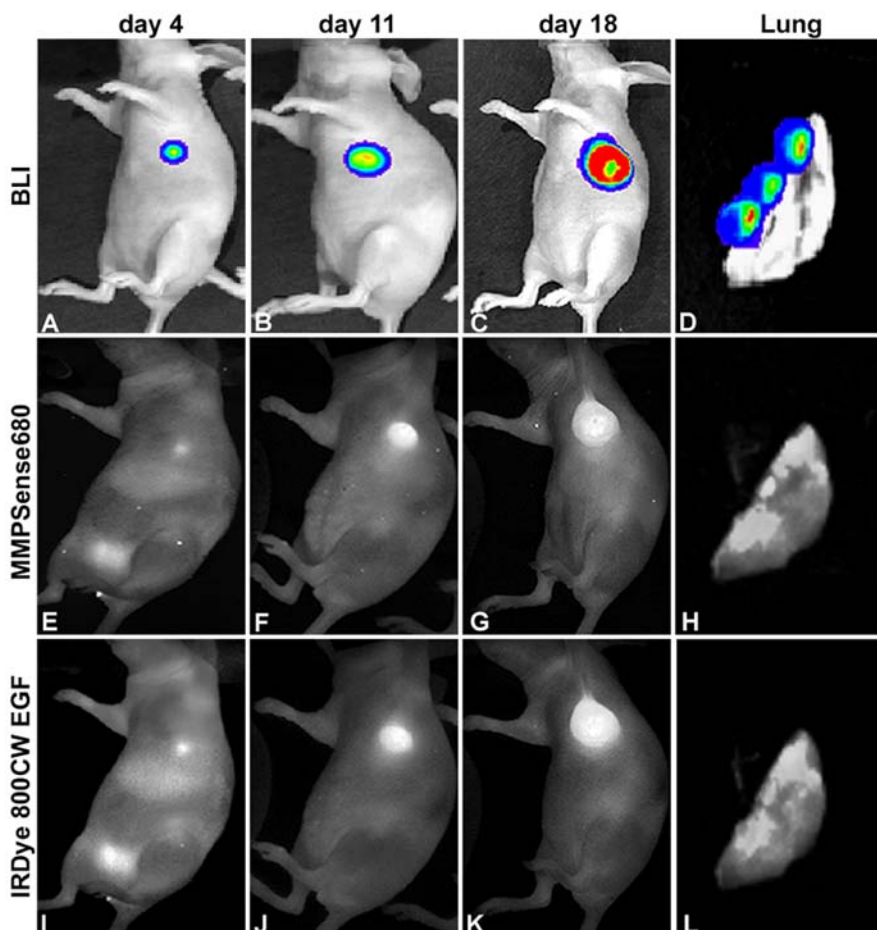


**Figure 5. Longitudinal imaging of tumor growth by BLI and FLI.** Representative images of tumor progression by BLI (A-D) and FLI utilizing MMPsense680 (E-H) in combination with IRDye 800CW EGF (I-L) are shown. At the end of the experiment, the lungs of the tumor-bearing mice were re-imaged and co-localizing BLI and FLI signals were observed, indicating the presence of pulmonary metastases (D, H and L).

Histological analysis of the primary 4T1-luc2 breast tumor revealed that it composed of actively proliferating neoplastic cells, growing with an incomplete tumor capsule and infiltrating the surrounding tissues (Fig. 6A). The pulmonary metastases of 4T1-luc2 breast tumor, which were detected by FLI and BLI, were confirmed histologically (Fig. 6B). Moreover, in the tumor sections, the presence of the GLUT-1 and EGFR, as well as the expression of MMP-9 and Cathepsin B, was shown by immunohistochemistry (Fig. 7 A-D). The localization of these markers was also revealed by FLI (Fig. 7 E-H).

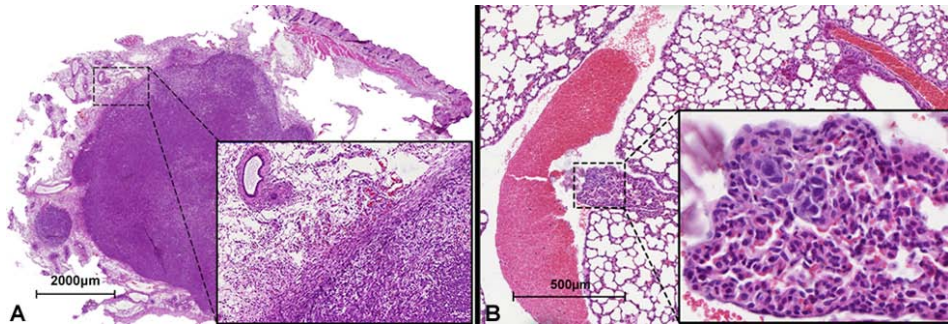


**Figure 6.** H&E stained paraffin sections of a 4T1-luc2 tumor in the MFP and its pulmonary metastases. Fig 6A shows a section of a primary 4T1-luc2 breast tumor indicating neoplastic, actively proliferating cells invading the healthy surrounding tissues. Fig. 6B shows subpleural pulmonary metastases of the tumor.

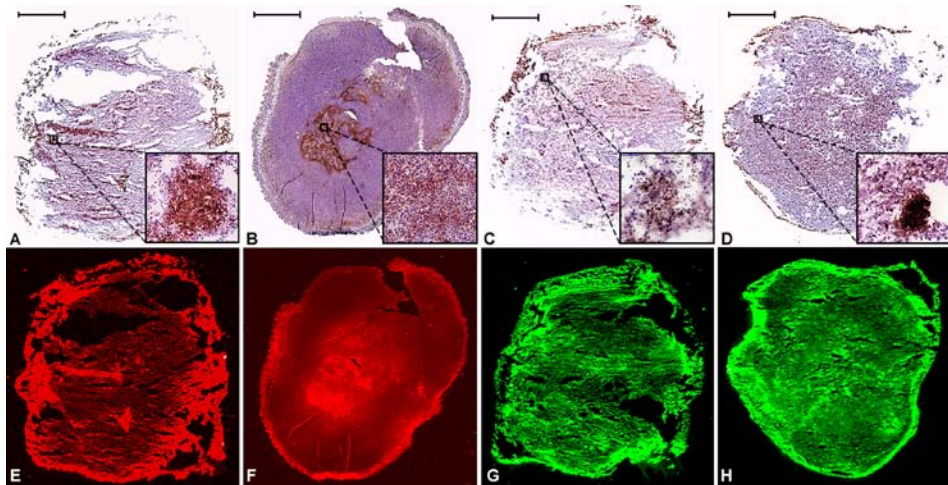


**Figure 7.** Immunohistological and fluorescent analysis of tumor sections. The upper panels showed the tumor sections stained with EGFR (A), GLUT-1 (B), MMP-9 (C) and CathpsinB (D) antibodies, respectively. The lower panels showed the fluorescent signal from tumors injected with IRDye 800CW EGF (E), IRDye 800CW 2-DG (F), MMPsense680 (G) and ProSense680 (H), respectively. Scale bar = 2000µm.

## Correlation between BLI and FLI measurements

Fig. 8 shows the growth curves of 4T1-luc2 breast tumors detected by BLI and by FLI, using the four different NIRF probes. The correlation plots of the BLI versus FLI signals from the various probes are shown in Fig. 9. A good linear relationship between the obtained tumor BLI and FLI signals from each of the four probes was found: Prosense680 ( $r=0.73$ ,  $p<0.01$ ), IRDye 800CW 2-DG ( $r=0.70$ ,  $p<0.01$ ), MMPsense680 ( $r=0.92$ ,  $p<0.0001$ ) and IRDye 800CW EGF ( $r=0.88$ ,  $p<0.0001$ ).

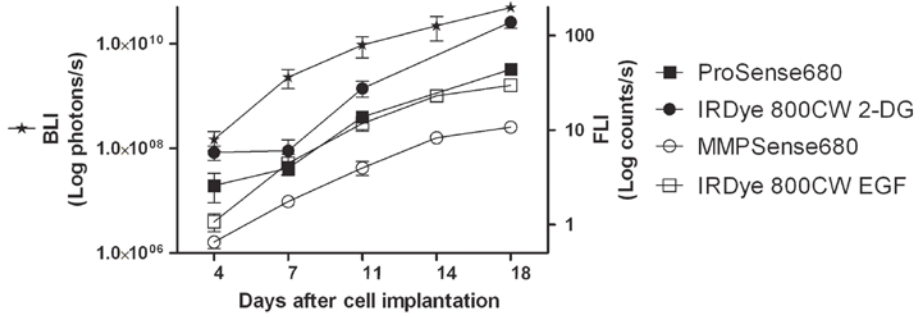


**Figure 8. Longitudinal imaging of 4T1-luc2 tumor growth with BLI and FLI.** During tumor progression, from day 4 to day 18, there was a steady increase in both BLI and FLI signal intensities.

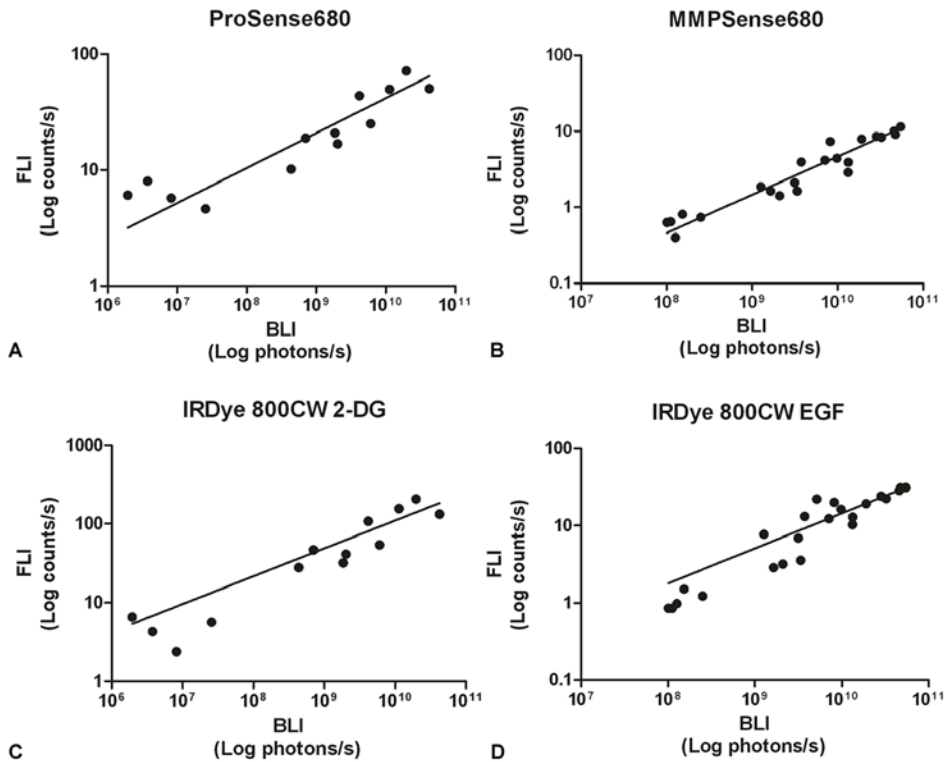


**Figure 9. Correlation plots of BLI against FLI signals obtained longitudinally, utilizing four different NIRF probes.** The Pearson's  $r$  values of the NIRF probes were: ProSense680 ( $r=0.72$ ,  $p<0.01$ ), IRDye 800CW 2-DG ( $r=0.70$ ,  $p<0.01$ ), MMPSense680 ( $r=0.92$ ,  $p<0.0001$ ) and IRDye 800CW EGF ( $r=0.88$ ,  $p<0.0001$ ).

---

## Calculation of the tumor-to-background ratio

The calculated TBRs of the different NIRF probes on day 18, the last day of the experiment, were: ProSense680  $2.29 \pm 0.38$ ; IRDye 800CW 2-DG  $2.14 \pm 0.27$ ; MMPsense680  $2.62 \pm 0.1$  and IRDye 800CW EGF  $4.02 \pm 0.24$ , respectively (Fig. 10).

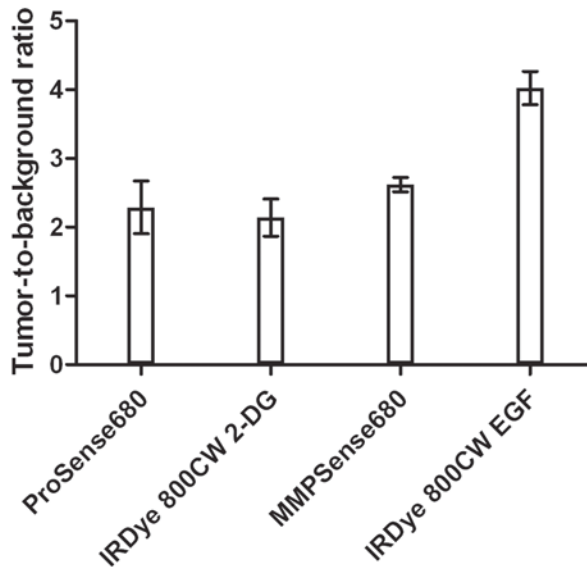


**Figure 10. TBRs of 4T1-luc2 tumors exploiting four different NIRF probes.** The TBRs, measured on the final day of the experiment, for ProSense680, IRDye 800CW 2-DG, MMPsense680 and IRDye 800CW EGF ranged from  $2.29 \pm 0.38$  to  $4.02 \pm 0.24$ .

## Discussion

Given its high sensitivity and negligible background in living tissues, BLI is extensively used for the non-invasive whole body optical imaging of tumor progression in small animals. However, in particular situations, FLI utilizing NIRF injectable probes is a promising alternative to BLI<sup>4-8</sup>. Contrary to BLI, FLI can be applied for clinical use. Recently we have successfully implemented FLI in the clinic for sentinel lymph node detection using the NIRF dye indocyanine green (ICG)<sup>33,34</sup>. In the near future, injectable tumor detecting NIRF probes may enter the clinic, for e.g. image-guided surgery, to facilitate radical tumor resection<sup>9</sup>.

To determine if FLI can be used as an alternative for BLI to follow tumor progression, we employed an orthotopic mouse model using the 4T1-luc2 breast cancer cell line. As orthotopically implanted 4T1-luc2 breast cancer cells grow at the primary injection site and can metastasize to various organs within 2-6 weeks,

this is an excellent mouse model that closely mimics human breast cancer <sup>29</sup>. Moreover, the introduction of a codon-optimized firefly luciferase (*Luc2*) gene into these cells strongly increases the brightness of the bioluminescent signal, allowing for more sensitive and early-stage non-invasive detection of the tumor <sup>2</sup>.

In the 4T1-luc2 model, we first examined the tumor detecting abilities of four different NIRF probes, which are able to detect general tumor cell characteristics. These include: increased expression of growth factor receptors (e.g., EGFR) <sup>25-27,35</sup>, elevated glucose metabolism and up-regulated glucose transporters (e.g., GLUT-1) <sup>23,24</sup> and an increased tissue proteolysis by the tumor, through upregulation of proteolytic enzymes such as MMP-2, -9 <sup>18,22,36</sup> and cathepsin B and D <sup>13,14</sup>.

*In vitro*, we examined the activity and binding properties of the four NIRF probes towards 4T1-luc2 cells and observed a dose-dependent uptake of each probe. This indicates that 4T1-luc2 cells express both GLUTs and EGFRs and also possess MMP- and cathepsin- activity *in vitro*. This is in line with previous studies showing that several mammary carcinoma cells, including 4T1 cells, express GLUTs and EGFRs <sup>37-39</sup> as well as MMP- and cathepsin- activity <sup>40-43</sup>. Using multispectral microscopy, we demonstrated that the activatable as well as the targeting probes were localized intracellularly. Consistently, Kovar *et al.* previously showed that the membrane targeting probe enters the cytoplasm via internalization of the probe/receptor complex shortly after the probe binds to its receptor <sup>21</sup>.

*In vivo*, tumor development and progression was studied using BLI and FLI, exploiting dual-wavelength imaging of a combination of an activatable (~700nm) and a targeting (~800 nm) NIRF probe. Tumors could be detected at an early stage of the development (day 4) and a strong linear correlation between FLI and BLI measurements was observed for all probes tested.

Metastases, present in the lungs, could only be detected *ex vivo* both by BLI and FLI and signals co-localized. Histological examination confirmed the presence of subpleural lung metastases. To further examine the specificity of the NIRF probes, immunohistochemistry was performed. Expression of GLUT-1, EGFR, MMP-9 and Cathepsin B was found throughout the tumor area and the expression pattern closely corresponded to that obtained with FLI. As can be appreciated from these immunohistological and FLI data, the distribution of the examined probes is rather inhomogeneous in this breast tumor model. The strong immuno-stained areas of each marker coincided with the more intense fluorescent areas. Thus, by using dual-wavelengths, combined with spectral unmixing, it is possible to detect multiple tumor features simultaneously. This may provide a more comprehensive image of the tumor, as different types of tumors are often heterogeneous in structure and molecular characteristics.

The sensitivities of both BLI and FLI *in vitro* and *in vivo* were assessed by tumor cell detection limit experiments. In our study, the *in vitro* detection limit of BLI was lower than 39cells/well. For FLI, the detection limits were 625 and

---

1,250 cells/well using Prosense680 and IRDye 800CW EGF, respectively. *In vivo*, one day after implantation, the lowest cell amount used for these experiments ( $1.25 \times 10^4$  cells) was well within the detection limit of BLI, as expected based on previous findings by Kim *et al*<sup>2</sup>. The detection limits of FLI using IRDye 800CW EGF and Prosense680 were approximately  $5 \times 10^5$  cells. Our findings indicate that although the sensitivity of FLI is lower than that of BLI, FLI is a reliable alternative in experimental settings where BLI cannot be used or is not wanted.

The TBR is a ratio, which expresses the specificity of a fluorescent probe, and as such it is used to discriminate between tumor tissue and healthy tissue. IRDye 800CW EGF had the highest TBR (TBR=4.02). The TBRs of the other NIRF probes examined in this study were all above two. Probes with a TBR above two can be considered applicable for clinical applications such as image-guided surgery<sup>9,44</sup>.

## Conclusions

Using various injectable tumor specific NIRF probes is a feasible approach to follow tumor growth and to detect metastasis. This was shown in sensitivity and specificity studies and by a linear correlation between the FLI and BLI tumor signals. Moreover, dual-wavelength imaging using spectral unmixing enables the simultaneous detection of multiple tumor characteristics. Taken together, dual-wavelength imaging of tumor progression by activatable and targeting NIRF probes is useful in pre-clinical studies and can possibly be translated towards clinical applications, such as image-guided surgery.

## Acknowledgements

We thank Professor P.C.W. Hogendoorn for the histological validation. The assistance of A.M.A. van der Laan in microscopic analysis is highly appreciated. This research was performed within the framework of CTMM, the Center for Translational Molecular Medicine, project MUSIS (grant 03O-202). This study is also supported by Dutch Cancer Society Koningin Wilhelmina Fonds (UL2007-3801).

## References

1. Kaijzel, E.L., Snoeks, T.J., Buijs, J.T., van der Pluijm, G. & Lowik, C.W. Multimodal imaging and treatment of bone metastasis. *Clin Exp Metastasis* **26**, 371-379 (2009).
2. Kim, J.B., *et al.* Non-invasive detection of a small number of bioluminescent cancer cells in vivo. *PLoS One* **5**, e9364 (2010).
3. Mezzanotte, L., *et al.* Sensitive dual color in vivo bioluminescence imaging using a new red codon optimized firefly luciferase and a green click beetle luciferase. *PLoS One* **6**, e19277 (2011).
4. Bhardwaj, V., *et al.* PLGA nanoparticles stabilized with cationic surfactant: safety studies and application in oral delivery of paclitaxel to treat chemical-induced breast cancer in rat. *Pharm Res* **26**, 2495-2503 (2009).
5. Bharadwaj, A.G., *et al.* Spontaneous metastasis of prostate cancer is promoted by excess hyaluronan synthesis and processing. *Am J Pathol* **174**, 1027-1036 (2009).
6. Chia, J.S., *et al.* Inhibition of metastasis, angiogenesis, and tumor growth by Chinese herbal cocktail Tien-Hsien Liquid. *BMC Cancer* **10**, 175 (2010).
7. Ciampicotti, M., *et al.* Development of metastatic HER2(+) breast cancer is independent of the adaptive immune system. *J Pathol* (2010).
8. Castano, A.P., Liu, Q. & Hamblin, M.R. A green fluorescent protein-expressing murine tumour but not its wild-type counterpart is cured by photodynamic therapy. *Br J Cancer* **94**, 391-397 (2006).
9. Keereweer, S., *et al.* Optical Image-guided Surgery-Where Do We Stand? *Mol Imaging Biol* (2010).
10. Weissleder, R. & Ntziachristos, V. Shedding light onto live molecular targets. *Nat Med* **9**, 123-128 (2003).
11. Kovar, J.L., Simpson, M.A., Schutz-Geschwender, A. & Olive, D.M. A systematic approach to the development of fluorescent contrast agents for optical imaging of mouse cancer models. *Anal Biochem* **367**, 1-12 (2007).
12. Rice, B.W. & Contag, C.H. The importance of being red. *Nat Biotechnol* **27**, 624-625 (2009).
13. Keppler, D., *et al.* Tumor progression and angiogenesis: cathepsin B & Co. *Biochem Cell Biol* **74**, 799-810 (1996).
14. Garcia, M., *et al.* Biological and clinical significance of cathepsin D in breast cancer metastasis. *Stem Cells* **14**, 642-650 (1996).
15. Kim, J., Yu, W., Kovalski, K. & Ossowski, L. Requirement for specific proteases in cancer cell intravasation as revealed by a novel semiquantitative PCR-based assay. *Cell* **94**, 353-362 (1998).
16. Jiang, T., *et al.* Tumor imaging by means of proteolytic activation of cell-penetrating peptides. *Proc Natl Acad Sci U S A* **101**, 17867-17872 (2004).
17. Chen, J., *et al.* Near-infrared fluorescent imaging of matrix metalloproteinase activity after myocardial infarction. *Circulation* **111**, 1800-1805 (2005).
18. Zhang, W., Matrisian, L.M., Holmbeck, K., Vick, C.C. & Rosenthal, E.L. Fibroblast-derived MT1-MMP promotes tumor progression in vitro and in vivo. *BMC Cancer* **6**, 52 (2006).
19. Kovar, J.L., Johnson, M.A., Volcheck, W.M., Chen, J. & Simpson, M.A. Hyaluronidase expression induces prostate tumor metastasis in an orthotopic mouse model. *Am J Pathol* **169**, 1415-1426 (2006).
20. Kovar, J.L., Volcheck, W.M., Chen, J. & Simpson, M.A. Purification method directly influences effectiveness of an epidermal growth factor-coupled targeting agent for noninvasive tumor detection in mice. *Anal Biochem* **361**, 47-54 (2007).
21. Kovar, J.L., Volcheck, W., Sevick-Muraca, E., Simpson, M.A. & Olive, D.M. Characterization and performance of a near-infrared 2-deoxyglucose optical imaging agent for mouse cancer models. *Anal Biochem* **384**, 254-262 (2009).
22. Zhou, H., *et al.* Dynamic near-infrared optical imaging of 2-deoxyglucose uptake by intracranial glioma of athymic mice. *PLoS One* **4**, e8051 (2009).
23. Pelicano, H., Martin, D.S., Xu, R.H. & Huang, P. Glycolysis inhibition for anticancer treatment. *Oncogene* **25**, 4633-4646 (2006).
24. Flier, J.S., Mueckler, M.M., Usher, P. & Lodish, H.F. Elevated levels of glucose transport and transporter messenger RNA are induced by ras or src oncogenes. *Science* **235**, 1492-1495 (1987).

25. Kraus, M.H., Popescu, N.C., Amsbaugh, S.C. & King, C.R. Overexpression of the EGF receptor-related proto-oncogene erbB-2 in human mammary tumor cell lines by different molecular mechanisms. *EMBO J* **6**, 605-610 (1987).
26. Lacroix, H., Iglehart, J.D., Skinner, M.A. & Kraus, M.H. Overexpression of erbB-2 or EGF receptor proteins present in early stage mammary carcinoma is detected simultaneously in matched primary tumors and regional metastases. *Oncogene* **4**, 145-151 (1989).
27. Stebbing, J., *et al.* Epidermal growth factor receptor status in early stage breast cancer is associated with cellular proliferation but not cross-talk. *J Clin Pathol* (2011).
28. Mayes, P., Dicker, D., Liu, Y. & El-Deiry, W. Noninvasive vascular imaging in fluorescent tumors using multispectral unmixing. *Biotechniques* **45**, 459-460, 461-454 (2008).
29. Pulaski, B.A. & Ostrand-Rosenberg, S. Reduction of established spontaneous mammary carcinoma metastases following immunotherapy with major histocompatibility complex class II and B7.1 cell-based tumor vaccines. *Cancer Res* **58**, 1486-1493 (1998).
30. Aslakson, C.J. & Miller, F.R. Selective events in the metastatic process defined by analysis of the sequential dissemination of subpopulations of a mouse mammary tumor. *Cancer Res* **52**, 1399-1405 (1992).
31. Levenson, R.M., Lynch, D.T., Kobayashi, H., Backer, J.M. & Backer, M.V. Multiplexing with multispectral imaging: from mice to microscopy. *ILAR J* **49**, 78-88 (2008).
32. Jenkins, D.E., *et al.* Bioluminescent imaging (BLI) to improve and refine traditional murine models of tumor growth and metastasis. *Clin Exp Metastasis* **20**, 733-744 (2003).
33. van der Vorst, J.R., *et al.* Optimization of near-infrared fluorescent sentinel lymph node mapping in cervical cancer patients. *Int J Gynecol Cancer* **21**, 1472-1478 (2011).
34. Schaafsma, B.E., *et al.* The clinical use of indocyanine green as a near-infrared fluorescent contrast agent for image-guided oncologic surgery. *J Surg Oncol* **104**, 323-332 (2011).
35. Levitzki, A. EGF receptor as a therapeutic target. *Lung Cancer* **41 Suppl 1**, S9-14 (2003).
36. Patel, S., Sumitra, G., Koner, B.C. & Saxena, A. Role of serum matrix metalloproteinase-2 and -9 to predict breast cancer progression. *Clin Biochem* (2011).
37. Bonine-Summers, A.R., *et al.* Epidermal growth factor receptor plays a significant role in hepatocyte growth factor mediated biological responses in mammary epithelial cells. *Cancer Biol Ther* **6**, 561-570 (2007).
38. Ke, S., *et al.* Near-infrared optical imaging of epidermal growth factor receptor in breast cancer xenografts. *Cancer Res* **63**, 7870-7875 (2003).
39. Wendt, M.K., Smith, J.A. & Schiemann, W.P. Transforming growth factor-beta-induced epithelial-mesenchymal transition facilitates epidermal growth factor-dependent breast cancer progression. *Oncogene* **29**, 6485-6498 (2010).
40. Giancotti, V. Breast cancer markers. *Cancer Lett* **243**, 145-159 (2006).
41. Gocheva, V. & Joyce, J.A. Cysteine cathepsins and the cutting edge of cancer invasion. *Cell Cycle* **6**, 60-64 (2007).
42. Parker, B.S., *et al.* Primary tumour expression of the cysteine cathepsin inhibitor Stefin A inhibits distant metastasis in breast cancer. *J Pathol* **214**, 337-346 (2008).
43. Kim, E.J., Hong, J.E., Eom, S.J., Lee, J.Y. & Park, J.H. Oral administration of benzylisothiocyanate inhibits solid tumor growth and lung metastasis of 4T1 murine mammary carcinoma cells in BALB/c mice. *Breast Cancer Res Treat* (2010).
44. Frangioni, J.V. New technologies for human cancer imaging. *J Clin Oncol* **26**, 4012-4021 (2008).







## CHAPTER THREE

# Multicolor Fluorescence Imaging of Traumatic Brain Injury in a Cryolesion Mouse Model

Based on

Smith BA\*, Xie BW\*, van Beek ER, Que I, Blankevoort V, Xiao S,  
Cole E, Hoehn M, Kaijzel EL, Lowik CW, Smith BD. *ACS Chem. Neurosci.*  
2012 Jul 18; 3(7):530-7.



## Abstract

Traumatic brain injury is characterized by initial tissue damage, which then can lead to secondary processes such as cell death and blood-brain-barrier disruption. Clinical and preclinical studies of traumatic brain injury typically employ anatomical imaging techniques and there is a need for new molecular imaging methods that provide complementary biochemical information. Here, we assess the ability of a targeted, near-infrared fluorescent probe, named PSS-794, to detect cell death in a brain cryolesion mouse model that replicates certain features of traumatic brain injury. In short, the model involves brief contact of a cold rod to the head of a living, anesthetized mouse. Using noninvasive whole-body fluorescence imaging, PSS-794 permitted visualization of the cryolesion in the living animal. *Ex vivo* imaging and histological analysis confirmed PSS-794 localization to site of brain cell death. The nontargeted, deep-red Tracer-653 was validated as a tracer dye for monitoring blood-brain-barrier disruption, and a binary mixture of PSS-794 and Tracer-653 was employed for multicolor imaging of cell death and blood-brain-barrier permeability in a single animal. The imaging data indicates that at 3 days after brain cryoinjury the amount of cell death had decreased significantly, but the integrity of the blood-brain-barrier was still impaired; at 7 days, the blood-brain-barrier was still three times more permeable than before cryoinjury.

## Keywords

Traumatic brain injury, multicolor fluorescence imaging, cell death imaging, blood-brain-barrier, annexin V, zinc(II)-dipicolylamine

---

## Introduction

Traumatic brain injury (TBI) is a major public health concern in the United States with 1.7 million people sustaining a TBI annually <sup>1</sup>. Over 2 % of the US population is believed to experience TBI-associated disabilities, accounting for approximately \$60 billion annually in direct and indirect costs <sup>2</sup>. TBI is a highly heterogeneous disorder that can manifest different pathophysiological changes depending on the type, severity, and location of the brain injury. TBI is typically characterized in two stages: 1) the primary injury at the site of impact which results in tissue damage and hemorrhaging, and 2) the delayed secondary insult that represents non-mechanical damage due to continuous pathological processes. These pathological processes include blood-brain barrier disruption, edema, oxidative stress, inflammation and cell death <sup>3</sup>. Clinical presentation of the secondary insult is usually delayed and believed to be sensitive to therapeutic intervention. Thus, the secondary pathological processes may be viable options as therapeutic and imaging targets for treatment and diagnosis of TBI.

In the clinic, computed tomography and magnetic resonance imaging are routinely used for brain imaging of TBI <sup>4,5</sup>. Both modalities rely on morphological changes which occur later in the disease process; thus, TBI diagnosis and prognosis would be better served using molecular imaging techniques that target early-stage biochemical changes <sup>6</sup>. Fluorescence optical imaging is an attractive option for preclinical research due to its inherent safety and high sensitivity, but very few optical imaging probes have been evaluated in animal models of TBI <sup>7</sup>. There is a specific need for deep-red and near-infrared fluorescent probes that allow relatively deep penetration of the light through skin and tissue. An attractive concept is the possibility of multicolor imaging using multiple probes in a single animal; each probe with its distinctive wavelength and ability to report on different biomolecular processes. At present, there is a small but growing number of literature examples of simultaneous multicolor *in vivo* optical imaging <sup>8,9,10</sup>. In the case of TBI, imaging studies would be greatly facilitated by the development of protocols that employ a mixture of a targeted probe for cell death and a non-targeted tracer for blood-brain-barrier (BBB) permeability. This requires two sets of technical advances: 1) development and validation of deep-red and near-infrared fluorescent imaging and tracer probes that enable multicolor *in vivo* imaging in living animals, and 2) straightforward pre-clinical TBI models that are amenable to optical imaging. Here we address both needs by adapting a preclinical mouse model for TBI and investigating a set of complementary fluorescent imaging probes.

Numerous fluorescent imaging probes have been developed to specifically target biomarkers associated with cell death, but the most popular biomarker for *in vivo* imaging is phosphatidylserine exposure on the plasma membrane <sup>11,12,13</sup>. Imaging results with protein-based probes are promising, but technical problems such as the

poor pharmacokinetics have combined to limit translation into the clinic<sup>14,15,16,17</sup>. It is quite challenging to alter the pharmacokinetics of proteins, so there is motivation to develop cell death imaging probes with low molecular weight<sup>18,19,20</sup>. We have contributed to this research topic by designing synthetic fluorescent zinc(II)-dipicolylamine probes that can distinguish the anionic membranes of dead and dying cells over the near neutral membranes of healthy cells<sup>21</sup>. To facilitate *in vivo* imaging, we developed PSS-794, a zinc(II)-dipicolylamine probe containing a near-infrared carbocyanine fluorophore. PSS-794 can identify cell death in a number of animal models<sup>22,23,24</sup>. In this current study, we demonstrate the ability of PSS-794 to non-invasively detect cell death in a brain cryolesion TBI mouse model using whole-body, epi-fluorescence imaging. Specifically, we compare cell death imaging performance of PSS-794 and fluorescently labeled Annexin V, a well-known protein-based probe for cell death imaging<sup>25</sup>. We also describe the non-targeted, deep-red dye, Tracer-653, for monitoring blood-brain-barrier disruption, and a binary mixture of PSS-794 and Tracer-653 for multicolor imaging of cell death and blood-brain-barrier permeability in a single animal.

## Results

The study examined four fluorescent imaging probes (Fig. 1). Two of the probes, the synthetic zinc(II)-dipicolylamine complex, PSS-794, and the dye-labeled protein, Annexin-Vivo 750, are known to selectively target the anionic membranes of dead and dying cells via bridging cations (zinc and calcium respectively). It is worth noting that PSS-794 is formulated as a zinc complex primarily to improve water solubility. Although the zinc complex is labile, the bloodstream concentration of  $Zn^{2+}$  (10-20  $\mu M$ ) is high enough to not limit the three component assembly of apo-PSS-794,  $Zn^{2+}$ , and phosphatidylserine at the membrane surface<sup>26</sup>. The other two probes, Tracer-794 and Tracer-653, are non-targeted fluorophores that diffuse through the blood pool, and thus serve to measure permeability of the BBB<sup>27,28</sup>. Tracer-794 has the same near-infrared fluorophore as PSS-794 and so is an excellent control compound to evaluate the effect of the attached zinc(II)-dipicolylamine targeting unit. Tracer-653 is a bright and stable deep-red dye that does not self-aggregate or associate with serum proteins. Furthermore, it has a narrow emission band that can be monitored simultaneously with near-infrared PSS-794 in the same animal using different imaging filter sets (filter sets for PSS-794 ex: 705-780 nm, em: 810- 885 nm; filter sets for Tracer-653 ex: 615-665 nm, em: 695-770 nm). The specific targeting of the four fluorescent probes was tested in an adapted brain cryolesion mouse model that induces rapid breakdown of the BBB causing vasogenic brain edema and tissue damage<sup>29</sup>. In short, two separate cohorts of athymic mice ( $n = 5$ ) were anesthetized by isoflurane inhalation. A metal cylinder with a 3 mm diameter

was pre-cooled in liquid nitrogen and applied to each mouse's head for 60 s. Individual mice then received an intracardiac injection of either PSS-794 (3.0 mg/kg), Tracer-794 (3.0 mg/kg), or Annexin-Vivo 750 and imaged in an IVIS Spectrum at 3 h, 6 h and 24 h post-probe injection. Figure 2 shows representative images at the different timepoints. Immediately after probe injection, there is apparent accumulation of Tracer-794 at the site of cryolesion but the tracer soon clears from the animal. At 3 h post-probe injection, cell death probes PSS-794 and Annexin-Vivo 750 both produce high contrast signals at the site of cryoinjury. In the case of PSS-794, the image intensity at the site of cryoinjury is higher at the 3 h time point compared to the 0 h time point, indicating a relatively slow rate of probe accumulation on the surface of the dead and dying cells. As expected, the Annexin-Vivo 750 also showed extensive accumulation in the kidneys<sup>16,30</sup>. Target to non-target (T/NT) quantification of *in vivo* images was performed by region of interest (ROI) analysis that compared the mean pixel intensities (MPI) at the cryoinjury site (T) to MPI at a non-target site (NT) on the lower back (Fig. 3). PSS-794 exhibited the highest T/NT at the 3 h timepoint ( $6.77 \pm 0.47$ ; T/NT  $\pm$  SEM;  $P < 0.003$ ), and then decreased. In contrast, the T/NT for Annexin-Vivo 750 increased incrementally to a value of  $4.87 \pm 0.54$  at the 24 h endpoint, reflecting a slower rate of clearance from the non-target site.

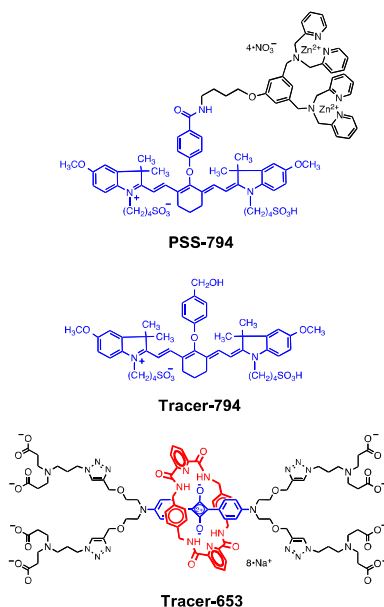


**Figure 1. Chemical structures of PSS-794, Tracer-794, and Tracer-653.**

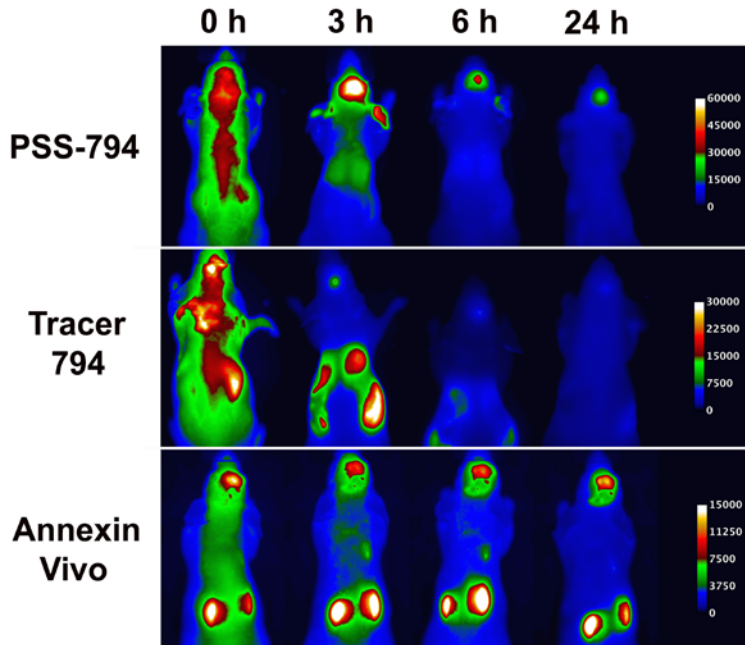


**Figure 2.** Representative in vivo near-infrared fluorescence montages of PSS-794, Tracer-794, and Annexin-Vivo 750 accumulation in a brain cryoinjury mouse model. A pre-cooled metal cylinder was applied to the head of each mouse for 60 s followed by intravenous injection of either PSS-794 (3.0 mg/kg), Tracer-794 (3.0 mg/kg), or Annexin-Vivo 750. Images were acquired at the indicated time points after probe injection. N = 5.

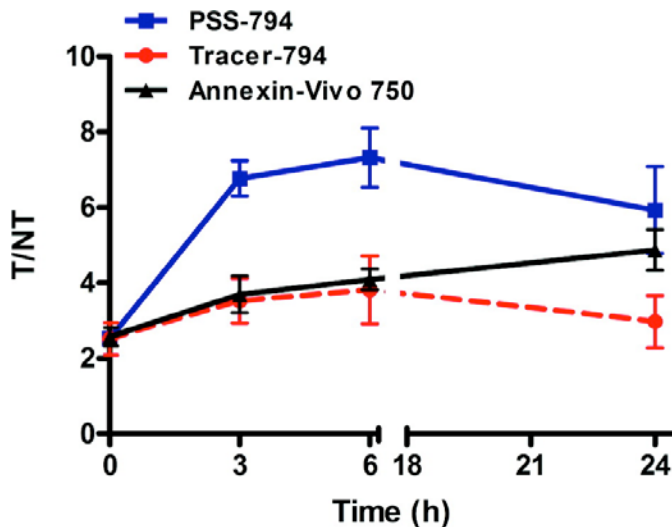


**Figure 3.** In vivo quantification of PSS-794, Tracer-794, and Annexin-Vivo 750 accumulating in a 60 s brain cryoinjury mouse model. Target to non-target ratios (T/NT) were calculated by region of interest (ROI) analysis of the digital images. Shapes were drawn around the site of the cryoinjury (target, T) and around an equivalent site on the lower back (non-target, NT) and the mean pixel intensities (MPI) were recorded. T/NT  $\pm$  SEM. N = 5. Numerical values and statistical significance are shown in Table S1.

---

At 24 h after probe injection, the mice were sacrificed and subjected to *ex vivo* imaging and histological analysis. *Ex vivo* whole-body images were acquired with 1) the skin removed from the head, which exposed the tissue over the skull, and 2) both the skin and the skull removed, which exposed the brain. ROI analysis compared the cryoinjury site *in vivo* just before animal sacrifice (labeled as Normal), to the deceased animal with skin removed (labeled as No Skin), and with both the skin and skull removed (labeled as No Skull). In each case, the MPI were recorded and normalized to the *in vivo* values. The normalized MPI for PSS-794 and Annexin-Vivo 750 decreased with each layer of tissue removed from the head (Fig. S2, Table S2). This is unusual because MPI at a deep-tissue site typically increases as the intervening skin and tissue is removed<sup>31</sup>. It appears that PSS-794 and Annexin-Vivo 750 target the cryolesion-induced cell death that is occurring on the skin, the pericranium, and on the brain. The normalized MPI for Tracer-794 images exhibited a different trend, and increased with removal of the skin followed by a decrease in MPI with removal of the skull (Fig. S2, Table S2). But the absolute MPI for the Tracer-794 images were substantially lower than the values for the PSS-794 images ( $P < 0.0005$  for Normal;  $P < 0.001$  for No Skin;  $P < 0.03$  for No Skull), reflecting the much greater clearance of tracer dye from the cryoinjury (Fig. S3). These spatial and temporal differences in probe localization indicate that the targeted cell death probe PSS-794 and non-targeted Tracer-794 accumulate in the brain cryoinjury by different mechanisms.

H&E micrographs of sectioned cryoinjured brains from mice sacrificed at 24 h after probe injection, showed a focal region of cell death that was surrounded by healthy brain tissue (Fig. 4A). Sections of cryoinjured brains were imaged using a fluorescence scanner to determine probe distribution throughout the brain. There was high accumulation of PSS-794 at the cryolesion site, while only negligible amounts of Tracer-794 were in the cryoinjured brain (Fig. S4). To further confirm that PSS-794 was targeting sites of brain cell death, immunohistochemistry was performed on the cryoinjured brains using an antibody specific for activated caspase-3. Fluorescence microscopy showed extensive staining of activated caspase-3 around the cryolesion, and also strong near-infrared fluorescence signal from the PSS-794 (Fig. 4B). Caspase-3 and PSS-794 staining could not be visualized in healthy regions of the brain (Fig. S6). Fluorescence from Tracer-794 could not be detected in the same regions as caspase-3 in the cryoinjured brains (Fig. S5).

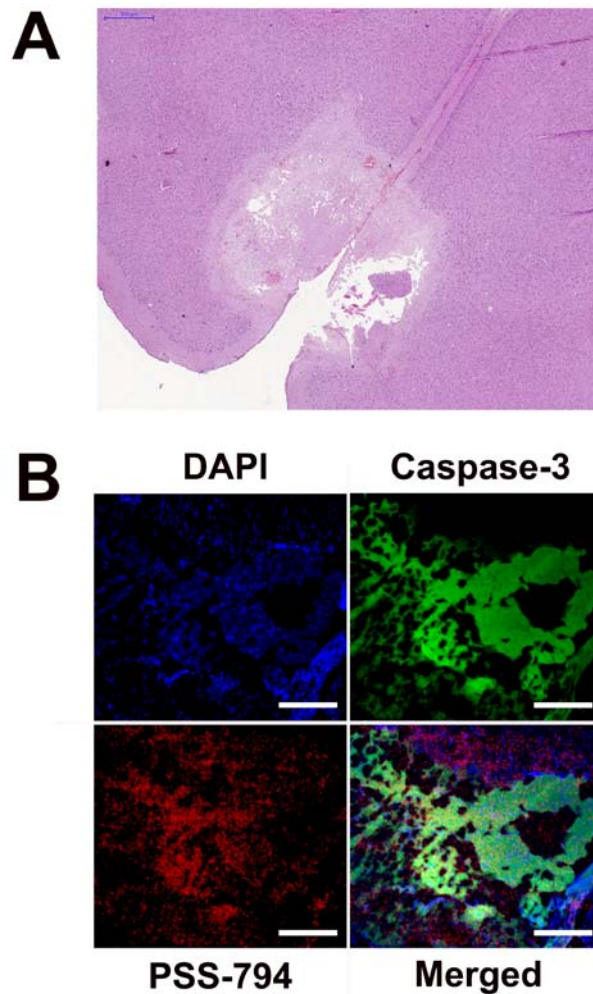


**Figure 4. Representative histological micrographs from cryoinjured mouse brains.** The micrographs were subjected either to H&E staining (A) or counterstained with an anti-caspase-3 antibody and DAPI (B). Images in B are from the region of the brain cryoinjury. Scale bar in A = 500  $\mu\text{m}$ . Scale bar in B = 200  $\mu\text{m}$ .

To determine if PSS-794 could measure TBI severity *in vivo*, the cryolesion experiment was repeated, with the time for contacting the pre-cooled metal cylinder to the mouse's head reduced to 20 s. The animals were subsequently dosed with either PSS-794 or Tracer-794 and then imaged over time (Fig. S7). As shown in Figure 5 and Table S3, T/NT values for PSS-794 and Tracer-794 were lower in the 20 s cryolesion mouse model indicating less tissue damage compared to the 60 s cryolesion. Quantification of the *ex vivo* images with skin or skull removed showed similar PSS-794 and Tracer-794 staining patterns as with the 60 s cryolesion (Fig. S2, Fig. S8).

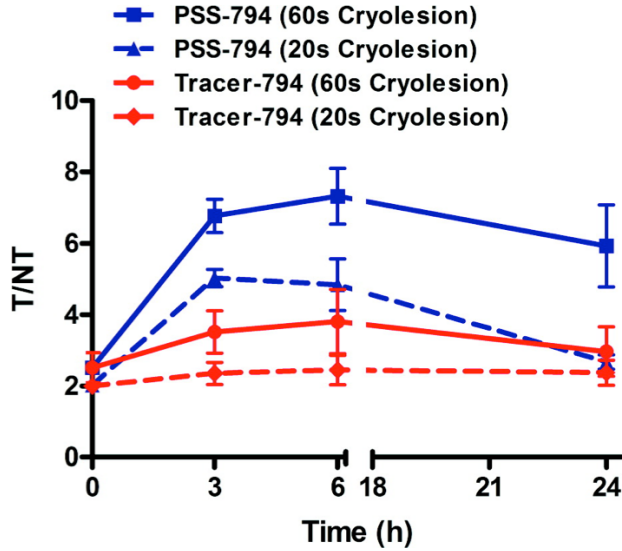


**Figure 5. Comparison of PSS-794 and Tracer-794 accumulation in the 20 s and 60 s brain cryoinjury mouse models.** T/NT ratios were calculated by ROI analysis. T/NT  $\pm$  SEM. N = 5. Numerical values and statistical significance are shown in Table S3.

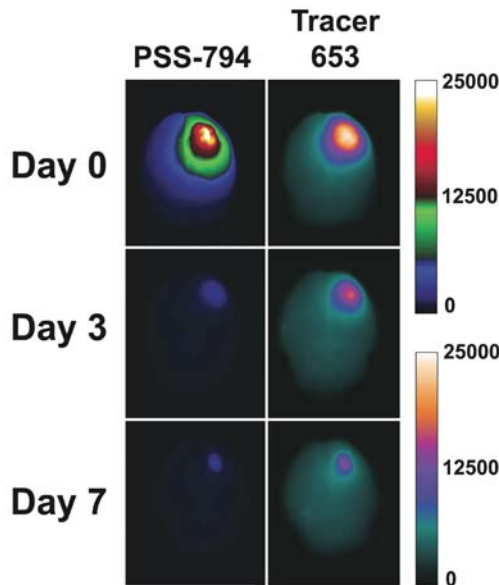


**Figure 6. Multicolor fluorescence imaging of cell death and blood-brain barrier disruption in cryoinjured brains.** Three cohorts of hairless mice were given a 60 s brain cryoinjury. Mice were then injected with a single dose of PSS-794 either immediately following cryoinjury (Day 0), 3 days post-cryoinjury (Day 3), or 7 days post-cryoinjury (Day 7). Each mouse was also injected with Tracer-653 at five hours post-PSS-794 injection. One hour after Tracer-653 injection, the mice were anesthetized and sacrificed. The brains were excised and placed in an epi-fluorescence imaging station for *ex vivo* imaging.

Evans Blue is routinely used to monitor BBB disruption in animal models<sup>32,33</sup>; thus, it served as a positive control for Tracer-653 in this mouse TBI model. Separate cohorts of cryoinjured mice were administered Evans Blue and Tracer-653. Evans Blue extravasation is typically quantified using histology; however, we utilized its weak red fluorescence emission to perform *ex vivo* imaging of the brain sections<sup>34</sup>. The *ex vivo* images of cryoinjured brains clearly showed accumulation of Evans Blue at Day 0 and less so at Day 3 post-injury (Fig. S12). When compared to Tracer-653, the area of Evans Blue staining was more localized at the site of cryoinjury. *In vivo*, Evans Blue binds to albumin proteins causing it to have a significantly higher molecular weight compared to Tracer-653 (67 kDa v.s. 2 kDa)<sup>35</sup>. The smaller effective size of Tracer-653 likely allows it to permeate into areas that are not accessible by the Evans Blue- albumin complex thus increasing the area of tissue that is stained by Tracer-653<sup>36,37</sup>. Taken together, the results indicate that Tracer-653 is an effective substitute for Evans Blue as a tracer probe for monitoring BBB disruption in TBI. Compared to Evans Blue, Tracer-653 exhibits a much brighter and narrower, deep-red emission band, and thus is more amenable to multicolor optical imaging.

To determine if we could simultaneously follow cranial cell death and BBB disruption in a single animal, we injected near-infrared PSS-794 and deep-red, Tracer-653 into mice that had received cryolesions. In short, three cohorts of hairless mice were administered 60 s brain cryolesions, and then injected with PSS-794 either immediately following cryoinjury, at 3 days post-cryoinjury, or at 7 days post-cryoinjury. Each mouse was also injected with Tracer-653 at 5 h post-PSS-794 injection (the injection lag time accounts for the difference in probe clearance rates). At one hour after Tracer-653 injection, the mice were anesthetized and sacrificed. The brains were excised and placed in an epifluorescence imaging station for *ex vivo* imaging. As shown in Figure 6, the amount of PSS-794 accumulation in these cryoinjured brain sections decreased greatly with the age of the injury. For example, the MPI for a cryolesion section on Day 3 was six-fold lower ( $P < 0.0002$ ) than the equivalent section on Day 0 (Fig. S10), indicating a substantial and relatively rapid decrease in the number dead and dying cells. In comparison the Tracer-653 signal in a cryoinjured brain decreased much more slowly with the age of injury. For example, the MPI for a cryolesion section on Day 7 was only about two-fold lower ( $P < 0.05$ ) than the equivalent section on Day 0 (Fig. 6, Fig. S10). Furthermore, the amount of Tracer-653 in a cryoinjured brain on Day 7 (as judged by comparing MPI) was three times higher ( $P < 0.05$ ) than an equivalent brain taken from a healthy control mouse treated with Tracer-653 (Fig. S11). Taken together, the Tracer-653 data consistently indicates that there is a gradual but incomplete improvement in BBB integrity over the seven-day post-cryolesion period.

---

## Discussion

The cryoinjury TBI mouse model used in these studies is a technically simple, high-throughput version of a previously reported model that contacts a pre-cooled rod with the surgically exposed skull of mice<sup>38,39,40</sup>. We chose to not remove the skin around the skull because preliminary studies indicated that the cell death probes target the dead skin cells generated during the surgery, thus complicating the *in vivo* imaging. We find that the lesions caused by this adapted cryoinjury model are highly reproducible in size and location (Fig. S3) and can be clearly delineated from the rest of the brain<sup>41</sup>. However, this model only conditionally mimics human TBI and lacks the diffusion axonal injuries that complicate human head injuries<sup>42</sup>. Other TBI mouse models such as the controlled cortical impact and fluid percussion injury models can mimic the whole spectrum of focal-type brain injuries and produce axonal injuries<sup>43</sup>. But these models have technical drawbacks including the need for specialized equipment and the requirement to perform animal craniotomy.

We evaluated two tracers, Tracer-794 and Tracer-653, and two targeted probes, PSS-794 (2 kDa) and Annexin Vivo-750 (36 kDa), in the adapted cryolesion TBI model. The two targeted probes are functionally similar in that they identify dead and dying cells with membranes that expose phosphatidylserine; however, the probes are quite different in molecular size and blood clearance pathways. Annexin probes are known to accumulate in the kidneys, whereas, PSS-794 clears more through the liver. The *in vivo* epi-fluorescence imaging showed that the maximum T/NT ratio with PSS-794 ( $6.77 \pm 0.47$ ) occurred at about 3 h after probe injection and was about two times higher than the maximum T/NT ratio with Annexin Vivo-750 (Fig. 2, Fig. 3). Both cell death probes cleared fairly slowly from the site of cryolesion. In comparison, Tracer-794 diffused in and completely out of the cryoinjury within a few hours. PSS-794 accumulation at the cryoinjury was observed to increase with injury severity, as judged by comparing the 20 s and 60 s cryolesions (Fig. 5). Thus, for pre-clinical studies that measure TBI severity in mouse models, optical imaging using PSS-794 appears to be a complementary alternate to classical methods that monitor changes in lesion volume<sup>44</sup>.

Multicolor fluorescence imaging is a promising new method to simultaneously monitor different physiological processes<sup>45,46</sup>, but has previously not been exploited to monitor TBI progression in mice. The highly fluorescent Tracer-653 functions like Evans Blue dye and allows optical imaging of BBB disruption. Furthermore, the deep-red emission of Tracer-653 can be distinguished from the near-infrared emission of PSS-794 in the same animal. Multicolor imaging of cryoinjured mice that were dosed with both PSS-794 and Tracer-653 enabled longitudinal tracking of the changes in cell death and BBB

permeability, respectively. The PSS-794 images in Figures 6 and S10 show that the amount of cell death had decreased substantially after Day 3, presumably due to efficient dead cell clearance by animal's innate immune system<sup>47</sup>. But the Tracer-653 images indicate that healing and repair of the BBB was a much slower process. After Day 7, the BBB was still substantially more permeable than before the cryoinjury event, a timeframe that is consistent with previous literature observations<sup>36,37</sup>.

In summary, we report that the synthetic near-infrared fluorescent probe, PSS-794, can be used to visualize cell death in an adapted cryolesion mouse model of TBI. The optical images with PSS-794 produced higher cryolesion signal contrast (higher T/NT ratio) than the mechanistically similar protein probe, Annexin-Vivo 750. Tracer-653 was validated as a low molecular weight, deep-red tracer dye for monitoring BBB disruption, and a binary mixture of PSS-794 and Tracer-653 was employed for multicolor imaging of cell death and BBB permeability in a single animal. The imaging data indicates that at three days after brain cryoinjury the amount of cell death had decreased significantly, but the integrity of the BBB was still impaired; at seven days the BBB was still substantially more permeable than before cryoinjury. The pathophysiological outcomes of TBI are highly heterogeneous in terms of severity and rate of progression. The time between physical trauma and the onset of secondary processes such as BBB breakdown is a potential window for therapeutic treatment<sup>48</sup>. It should be possible to develop this adapted cryoinjury mouse model into a high throughput, optical imaging screen of experimental therapeutics for TBI.

## Methods

### Ethics statement

All animal experiments were approved for animal health, ethics, and research by the Animal Welfare Committee of Leiden University Medical Center and the Institutional Animal Care and Use Committee of the University of Notre Dame. All animals received humane care and maintenance in compliance with the Code of Practice Use of Laboratory Animals in Cancer Research<sup>49</sup>.

### Probe synthesis

The synthesis and properties of Tracer-794 ( $\lambda_{\text{ex}}$ : 794 nm,  $\lambda_{\text{em}}$ : 810 nm), PSS-794 ( $\lambda_{\text{ex}}$ : 794 nm,  $\lambda_{\text{em}}$ : 810 nm) and Tracer-653 ( $\lambda_{\text{ex}}$ : 653 nm,  $\lambda_{\text{em}}$ : 673 nm) have been reported previously<sup>50,51</sup>. PSS-794 is commercially available as PSVue<sup>®</sup> 794 (Molecular Targeting Technologies Inc., West Chester, PA). Annexin-Vivo 750<sup>®</sup> ( $\lambda_{\text{ex}}$ : 755 nm,  $\lambda_{\text{em}}$ : 772 nm) was purchased from PerkinElmer (Waltham, MA).

---

## Traumatic brain injury mouse models

Two cohorts of 4-6 week old athymic mice (male, ~25 g, *nu/nu*) ( $n = 5$ ) were anesthetized by 2-3 % isoflurane inhalation. A metal cylinder, with a 3 mm diameter, was pre-cooled in liquid nitrogen and applied to the parietal region of each mouse's head for either 20 s or 60 s. The mice then received an intracardiac injection of either PSS-794 (3.0 mg/kg, 100  $\mu$ L in 1% DMSO/H<sub>2</sub>O) or Tracer-794 (3.0 mg/kg, 100  $\mu$ L in H<sub>2</sub>O). A cohort of athymic mice ( $n = 5$ ) were subjected to a 60 s cryoinjury and received an intracardiac injection of Annexin-Vivo 750.

To investigate the progression of blood-brain-barrier disruption and cell death in traumatic brain injury, three cohorts of nude mice (male, ~25g, SKH1-E) ( $n=5$ ) were anesthetized by 2-3 % isoflurane inhalation. A metal cylinder, with a 3 mm diameter, was pre-cooled in liquid nitrogen and applied to the parietal region of each mouse's head for 60 s. The mice then received a retro-orbital injection of PSS-794 (3.0 mg/kg, 100  $\mu$ L in 1% DMSO/H<sub>2</sub>O) and placed back into their cages. Five hours later, the mice received a retro-orbital injection of Tracer-653 (2.0 mg/kg, 100  $\mu$ L in H<sub>2</sub>O). One hour later, the mice were anesthetized by isoflurane inhalation and placed inside an IVIS Lumina (Caliper Life Sciences, Hopkinton, MA) configured for whole-body, epi-fluorescence imaging. After *in vivo* imaging, one cohort was sacrificed and *ex vivo* fluorescence imaging was performed on the excised brain. The other cohorts were placed back into their cages. Cohorts were subjected to the same PSS-794 and Tracer-653 injection and imaging procedures, either three or seven days post-injury (Fig. S9).

Evans Blue (Sigma, St. Louis, MO) (25 mg/kg, 100  $\mu$ L in H<sub>2</sub>O) was injected intravenously into hairless mice following 60 s brain cryolesion. The probe was allowed to circulate for one hour, then the mice were anesthetized and sacrificed. The brains were excised and placed inside an IVIS Lumina for *ex vivo* epi-fluorescence imaging. Another cohort of hairless mice was subjected to the same injection and imaging procedure three days post-injury.

### *In vivo* near-infrared fluorescence imaging

Athymic mice were anesthetized by 2-3 % isoflurane inhalation and placed inside an IVIS Spectrum (Caliper Life Sciences, Hopkinton, MA) configured for whole-body epi-fluorescence imaging. For mice injected with PSS-794 or Tracer-794, images were acquired immediately after probe injection and at 3, 6, and 24 h time points (excitation filter: 710 nm, emission filter: 820 nm, exposure time: 1 s, bin: 8, f/stop: 2, field of view: 6.6 cm). For mice injected with Annexin-Vivo 750, images were acquired for 1 s using a 710 nm excitation filter and a 780 nm emission filter (bin: 4, f/stop: 2, field of view: 6.6 cm). After each time point, the mice were returned to their cages and fed *ad libitum*.

Acquired images were exported as 16 bit tiff files and region of interest (ROI)

analysis was performed using ImageJ 1.44. In short, a ROI was drawn around the cryoinjury site (T) and an equal sized ROI was drawn on the lower back (NT) of each mouse (Fig. S1). The mean pixel intensity of the T and NT was measured and recorded for each mouse. The T/NT ratios were then calculated, and statistical analysis was performed to acquire the average of each ratio ( $n = 5$ ) with the standard error of the mean (SEM). The resulting ROI values were plotted using Graphpad Prism 4.

## *Ex vivo* near-infrared fluorescence imaging

Following the 24 h time point, mice were sacrificed by cervical dislocation. *Ex vivo* images were acquired with the skin from the head removed and both the skin and the skull removed to facilitate epi-fluorescence imaging with an IVIS Spectrum (excitation filter: 710 nm, emission filter: 820 nm, exposure time: 1 s, bin: 8, f/stop: 2, field of view: 6.6 cm for PSS-794 and Tracer-794) (excitation filter: 710 nm, emission filter: 780 nm, exposure time: 1 s, bin: 4, f/stop: 2, field of view: 6.6 cm for Annexin-Vivo 750).

All the nude mice were sacrificed, the brains excised and placed inside an IVIS Lumina for multicolor epi-fluorescence imaging (excitation filter: 705-780 nm, emission filter: 810-885 nm, exposure time: 5 s, bin: 2, f/stop: 2, field of view: 5 cm for PSS-794) (excitation filter: 615-665 nm, emission filter: 695-770 nm, exposure time: 8 s, bin: 2, f/stop: 2, field of view: 5 cm for Tracer-653). The ROI analysis was performed by drawing an ROI around the cryoinjury site and recording the mean pixel intensity. The resulting mean pixel intensities were plotted using Graphpad Prism 4.

## Histology

Brains were flash frozen in OCT (Tissue Tek, Torrance, CA) were fixed in 4% formaldehyde, cut into 10  $\mu\text{m}$  paraffin sections. Tissue sections were mounted onto slides and imaged using a LI-COR Odyssey (LI-COR Biosciences, Lincoln, NE) scanner equipped with a 785 nm diode laser. Slides were also subjected to hematoxylin and eosin (H&E) staining to determine the extent of cell death and cellular morphological changes in the cerebral cortex. Selected brain sections were incubated overnight with a rabbit anti-human polyclonal caspase-3 antibody (Abcam Inc.; 1:50). The sections were then incubated with goat anti-rabbit IgG conjugated to Alexa-Fluor 488 (Invitrogen; 1:500) for 15 min, and counterstained with DAPI. Fluorescence images of the sections were acquired using a Nikon TE-2000 U epi-fluorescence microscope equipped with the appropriate UV (ex. 340/80 nm, em. 435/85 nm), GFP (ex. 450/90 nm, em. 500/50 nm), and near-infrared filters (ex. 710/75 nm, em. 810/90 nm). Fluorescence images were captured using Metamorph software (Universal) and analyzed using ImageJ 1.44.

---

## Statistical analysis

Results are depicted as mean  $\pm$  standard error of the mean (SEM). Statistical analysis was performed using a Student's t-test.

## Acknowledgements

We thank the Notre Dame Histology Core and the Notre Dame Integrated Imaging Facility for preparation of histological sections and access to whole animal imaging equipment. This study was supported by the Center for Translational Molecular Medicine, project MUSIS (grant 03O-202); NIH grants R01GM059078 (B.D.S.) and T32GM075762 (B.A.S.), Volkswagen grant I83443, and the ENCITE project 201842.

## Supporting Information:

Additional imaging data and quantitative analysis are available free of charge via the Internet at <http://pubs.acs.org>.

## References

1. Faul, M., Xu, L., Wald, M. M. & Coronado, V. G. Traumatic Brain Injury in the United States: Emergency Department Visits, Hospitalizations, and Deaths, 2002-2006. *National Center for Injury Prevention and Control, Centers for Disease Control and Prevention*, 1-71 (2010).
2. Thurman, D. J., et al. Traumatic Brain Injury in the United States: a Public Health Perspective. *J. Head Trauma Rehabil.* **14**, 602-615 (1999).
3. Werner, C. & Engelhard, K. Pathophysiology of Traumatic Brain Injury. *Br. J. Anaesth.* **99**, 4-9 (2007).
4. Kim, J. J. & Gean, A. D. Imaging for the Diagnosis and Management of Traumatic Brain Injury. *Neurotherapeutics* **8**, 39-53 (2011).
5. Wilson, J. R. F. & Green, A. Acute Traumatic Brain Injury: a Review of Recent Advances in Imaging and Management. *Eur. J. Trauma Emerg. Surg.* **35**, 176-185 (2009).
6. Chapon, C., et al. Imaging E-Selectin Expression Following Traumatic Brain Injury in the Rat using a Targeted USPIO Contrast Agent. *Magn. Reson. Mater. Phys.* **22**, 167-174 (2009).
7. Reshef, A., et al. Targeting Cell Death In Vivo in Experimental Traumatic Brain Injury by a Novel Molecular Probe. *J. Neurotrauma* **25**, 569-580 (2008).
8. Kosaka, N., et al. In Vivo Real-Time, Multicolor, Quantum Dot Lymphatic Imaging. *J. Invest. Dermatol.* **129**, 2818-2822 (2009).
9. Yamamoto, N., Tsuchiya, H. & Hoffman, R. M. Tumor Imaging with Multicolor Fluorescent Protein Expression. *Int. J. Clin. Oncol.* **16**, 84-91 (2011).
10. Mitsunaga, M., et al. In Vivo Longitudinal Imaging of Experimental Human Papillomavirus Infection in Mice with a Multicolor Fluorescence Mini-Endoscopy System. *Cancer Prev. Res.* **4**, 767-773 (2011).
11. Blankenberg, F. G. In Vivo Detection of Apoptosis. *J. Nucl. Med.* **49**, 81S-95S (2008).
12. Zhao, M. In Vivo Apoptosis Imaging Agents and Strategies. *Anti-Cancer Agents Med. Chem.* **9**, 1018- 1023 (2009).
13. Niu, G., & Chen, X. Apoptosis Imaging: Beyond Annexin V. *J. Nucl. Med.* **51**, 1659-1662 (2010).
14. Ntziachristos, V., et al. Visualization of Antitumor Treatment by Means of Fluorescence Molecular Tomography with an Annexin V-Cy5.5 Conjugate. *Proc. Natl. Acad. Sci. U.S.A.* **101**, 12294-12299 (2004).
15. Beekman, C. A., et al. Questioning the Value of (99m)Tc-HYNIC-Annexin V Based Response Monitoring after Docetaxel Treatment in a Mouse Model for Hereditary Breast Cancer. *Appl. Radiat. Isot.* **69**, 656-662 (2011).
16. Vanderheyden, J. L., et al. Evaluation of 99mTc- MAG3-Annexin V: Influence of the Chelate on In Vitro and In Vivo Properties in Mice. *Nuc. Med. Biol.* **33**, 135- 144 (2006).
17. Lederle, W., et al. Failure of Annexin-Based Apoptosis Imaging in the Assessment of Antiangiogenic Therapy Effects. *EJNMMI Research* **1**, 26 (2011).
18. Burtea, C., et al. Peptidic Targeting of Phosphatidylserine for the MRI Detection of Apoptosis in Atherosclerotic Plaques. *Mol. Pharmaceutics* **6**, 1903-1919 (2009).
19. Zheng, H., Wang, F., Wang, Q. & Gao, J. Cofactor-Free Detection of Phosphatidylserine with Cyclic Peptides Mimicking Lactadherin. *J. Am. Chem. Soc.* **131**, 15280-15283 (2011).
20. Xiong, C., et al. Peptide-Based Imaging Agents Targeting Phosphatidylserine for the Detection of Apoptosis. *J. Med. Chem.* **54**, 1825-1835 (2011).
21. Hanshaw, R.G. & Smith, B.D. New Reagents for Phosphatidylserine Recognition and Detection of Apoptosis. *Bioorg. Med. Chem.* **13**, 5035-5042 (2005).
22. Smith, B.A., et al. Optical Imaging of Mammary and Prostate Tumors in Living Animals using a Synthetic Near Infrared Zinc(II)-Dipicolylamine Probe for Anionic Cell Surfaces. *J. Am. Chem. Soc.* **132**, 67-69 (2010).
23. Smith, B.A., et al. In Vivo Optical Imaging of Acute Cell Death using a Near-Infrared Fluorescent Zinc-Dipicolylamine Probe. *Mol. Pharmaceutics* **8**, 583-590 (2011).
24. Smith, B. A., et al. In Vivo Targeting of Cell Death using a Synthetic Fluorescent Molecular Probe. *Apoptosis* **16**, 722-731 (2011).

25. Bahamni, P., *et al.* Visualization of Cell Death in Mice with Focal Cerebral Ischemia using Fluorescent Annexin A5, Propidium Iodide, and TUNEL Staining. *J. Cereb. Blood Flow Metab.* **31**, 1311-1320 (2011).
26. O'Neil, E. J., & Smith, B. D. Anion Recognition using Dimetallic Coordination Complexes. *Coord. Chem. Rev.* **250**, 3068-3080 (2004).
27. Abulrob, A., Brunette, E., Slin, J., Baumann, E., & Stanimirovic, D. Dynamic Analysis of the Blood- Brain Barrier Disruption in Experimental Stroke using Time Domain In Vivo Fluorescence Imaging. *Mol. Imaging* **7**, 248-262 (2008).
28. Hawkins, B. T., & Egleton, R. D. Fluorescence Imaging of Blood-Brain Barrier Disruption. *J. Neurosci. Meth.* **151**, 262-267 (2006).
29. Murakami, K., *et al.* Cold Injury in Mice: a Model to Study Mechanisms of Brain Edema and Neuronal Apoptosis. *Prog. Neurobiol.* **57**, 289-299 (1999).
30. Lin, K. J., *et al.* In Vivo Imaging of Radiation-Induced Tissue Apoptosis by <sup>99m</sup>Tc(I)-his6-Annexin A5. *Ann. Nucl. Med.* DOI: 10.1007/s12149-012-0571-x (2012).
31. Leblond, F., Davis, S.C., Valdés, P.A., & Pogue, B. W. Pre-Clinical Whole-Body Fluorescence Imaging: Review of Instruments, Methods and Applications. *J. Photochem. Photobiol. B* **98**, 77-94 (2010).
32. Belayev, L., Busto, R., Zhao, W., & Ginsberg, M. D. Quantitative Evaluation of Blood-Brain Barrier Permeability Following Middle Cerebral Artery Occlusion in Rats. *Brain Res.* **739**, 88-96 (1996).
33. Del Valle, J., Camins, A., Pallás, M., Vilaplana, J., & Pelegrí, C. A New Method for Determining Blood-Brain Barrier Integrity Based on Intracardiac Perfusion of an Evans Blue-Hoechst Cocktail. *J. Neurosci. Meth.* **174**, 42-49 (2008).
34. Saria, A., & Lundberg, J. M. Evans Blue Fluorescence: Quantitative and Morphological Evaluation of Vascular Permeability in Animal Tissues. *J. Neurosci. Meth.* **8**, 41-49 (1983).
35. Wolman, M. *et al.* Evaluation of the Dye-Protein Tracers in Pathophysiology of the Blood-Brain Barrier. *Acta Neuropathol.* **54**, 55-61 (1981).
36. Habgood, M. D., *et al.* Changes in Blood-Brain Barrier Permeability to Large and Small Molecules Following Traumatic Brain Injury in Mice. *Eur. J. Neurosci.* **25**, 231-238 (2007).
37. Lotocki, G., *et al.* Alterations in Blood-Brain Barrier Permeability to Large and Small Molecules and Leukocyte Accumulation after Traumatic Brain Injury: Effects of Post-Traumatic Hypothermia. *J. Neurotrauma* **26**, 1123-1134 (2009).
38. Raslan, F., *et al.* Inhibition of Bradykinin Receptor B1 Protects Mice from Focal Brain Injury by Reducing Blood-Brain Barrier Leakage and Inflammation. *J. Cereb. Blood Flow Metab.* **30**, 1477-1486 (2010).
39. Stoffel, M., *et al.* Identification of Brain Tissue Necrosis by MRI: Validation by Histomorphometry. *J. Neurotrauma* **21**, 733-740 (2004).
40. Spaeth, N., *et al.* Uptake of <sup>18</sup>F-Fluorocholine, <sup>18</sup>F-Fluoroethyl-L-Tyrosine, and <sup>18</sup>F-FDG in Acute Cerebral Radiation Injury in the Rat: Implications for Separation of Radiation Necrosis from Tumor Recurrence. *J. Nucl. Med.* **45**, 1931-1938 (2004).
41. Albert-Weissenberger, C. & Sirén, A. L. Experimental Traumatic Brain Injury. *Exp. Trans. Stroke Med.* **2**, 16-23 (2010).
42. Gaetz, M. The Neurophysiology of Brain Injury. *Clin. Neurophysiol.* **115**, 4-18 (2004).
43. O'Connor, W. T., Smyth, A. & Gilchrist, M. D. Animal Models of Traumatic Brain Injury: a Critical Evaluation. *Pharmacol. Therapeut.* **130**, 106-113 (2011).
44. Eriskat, J., Fürst, M., Stoffel, M. & Baethmann, A. Correlation of Lesion Volume and Brain Swelling from a Focal Brain Trauma. *Acta Neurochir.* **86**, 265-266 (2003).
45. Kobayashi, H., *et al.* Simultaneous Multicolor Imaging of Five Different Lymphatic Basins using Quantum Dots. *Nano Lett.* **7**, 1711- 1716 (2007).
46. Yang, M., Jiang, P. & Hoffman, R. M. Whole-Body Subcellular Multicolor Imaging of Tumor-Host Interaction and Drug Response in Real Time. *Cancer Res.* **67**, 5195-5200 (2007).
47. Giulian, D., *et al.* The Role of Mononuclear

- Phagocytes in Wound Healing After Traumatic Injury to Adult Mammalian Brain. *J. Neurosci.* **9**, 4416-4429 (1989).
48. Shloesberg, D., Benifa, M., Kaufer, D. & Friedman, A. Blood-Brain Barrier Breakdown as a Therapeutic Target in Traumatic Brain Injury. *Nat. Rev. Neurol.* **6**, 393-403 (2010).
49. Netherlands Inspectorate for Health Protection, Commodities and Veterinary Public Health Code of Practice Animal Experiments in Cancer Research. Inspectie W&V, 1-22 (1999).
50. Leevy, W. M., *et al.* Optical Imaging of Bacterial Infection in Living Mice using a Near-Infrared Molecular Probe. *J. Am. Chem. Soc.* **128**, 16476-16477 (2006).
51. Cole, E. L., *et al.* Water-Soluble, Deep-Red Fluorescent Squaraine Rotaxanes. *Org. Biomol. Chem.* DOI: 10/1039/c2ob06783h (2011).





## CHAPTER FOUR

# Optical Imaging of Cell Death in Traumatic Brain Injury Using a Heat Shock Protein-90 Alkylator

Based on

Xie BW\*, Park D\*, Van Beek ER, Blankevoort V, Orabi Y, Que I,  
Kaijzel EL, Chan A, Hogg PJ, Löwik CW. *Cell Death Dis.* 2013; 4: e473.



## Abstract

Traumatic brain injury is a major public health concern and is characterized by both apoptotic and necrotic cell death in the lesion. Anatomical imaging is usually employed to assess traumatic brain injuries and there is a need for imaging modalities that provide complementary cellular information. We sought to non-invasively image cell death in a mouse model of traumatic brain injury using a near-infrared fluorescent conjugate of a synthetic heat shock protein-90 alkylator, 4-(N-(S-glutathionylacetyl) amino) phenylarsonous acid (GSAO). GSAO labels both apoptotic and necrotic cells coincident with loss of plasma membrane integrity. The optical GSAO specifically labelled apoptotic and necrotic cells in culture and did not accumulate in healthy organs or tissues in the living mouse body. The conjugate is a very effective imager of cell death in brain lesions. The optical GSAO was detected by fluorescence intensity and GSAO bound to dying/dead cells was detected from prolongation of the fluorescence lifetime. An optimal signal-to-background ratio was achieved as early as three hours after injection of the probe and the signal intensity positively correlated with both lesion size and probe concentration. This optical GSAO offers a convenient and robust means to non-invasively image apoptotic and necrotic cell death in brain and other lesions.

## Keywords

Traumatic brain injury, cryolesion, apoptosis, necrosis, GSAO, optical imaging

## Abbreviations

DMP, dimercaptopropanol; GSAO, 4-(N-(S-glutathionylacetyl) amino) phenylarsonous acid; GSCA, 4-(N-((S-glutathionyl)acetyl)amino)benzoic acid; AF750, Alex Flour 750; Hsp90, heat shock protein 90; PI, propidium iodide; ROI, region of interest; TUNEL, TdT-mediated dUTP nick-end labelling

---

## Introduction

Traumatic brain injury is estimated to affect 2% of the US population and cost about \$60 billion annually<sup>1,2</sup>. The nature of the injuries depends on the type, severity and location of the insult but are usually characterized by primary mechanical damage and hemorrhage followed by secondary damage due to disruption of the blood-brain-barrier and associated inflammation<sup>3</sup>. The secondary insult occurs hours to days after the primary insult and is amenable to therapeutic intervention. Computer tomography and magnetic resonance imaging are used to assess morphological changes in traumatic brain injury that occur in the later stages of the injury<sup>4</sup>. Treatment of the secondary damage would be facilitated by imaging modalities that report on changes in the lesion at the cellular level. Traumatic brain injury is characterized by both apoptotic and necrotic cell death in the lesion<sup>3</sup> and this is what we sought to image in this study.

An established model of traumatic brain injury in mice is the cryolesion. A sharp delineated area of neuronal cell death is induced in the mouse brain by applying a liquid nitrogen cooled rod to the skull<sup>5</sup>. Cell death within brain cryolesions occurs via two distinct mechanisms. Firstly, intracellular ice crystals rupture the cell membrane causing direct cell damage<sup>6</sup>. Secondly, injury to endothelial cell junctions results in increased vascular permeability, oedema, thrombosis, and ultimately failure of the microcirculation, leading to a secondary ischemic assault<sup>7</sup>. Whilst the centre of the lesion is characterized by tissue necrosis, apoptosis is also observed in the periphery as early as 12 hours post injury<sup>5</sup>. The latter is thought to occur via mitochondrial permeabilization following increased expression of Bax<sup>8</sup>. Upregulation of genes involved in neuronal survival or regeneration is also observed<sup>9,10</sup>. This lesion bears many features of neurotrauma<sup>6,7</sup>. Here we have non-invasively imaged the cell death in these lesions using a heat shock protein 90 (Hsp90) alkylator<sup>11</sup>.

GSAO (4-(N-(S-glutathionylacetyl) amino)phenylarsonous acid) is a tripeptide trivalent arsenical that rapidly accumulates in the cytoplasm of dying cells in culture and in murine tumors<sup>11</sup>. It is retained in the cell predominantly through covalent reaction with the Cys597 and Cys598 residues of Hsp90, which is the most abundant protein chaperone in mammalian cells<sup>12</sup>. The As(III) atom of GSAO cross-links the Hsp90 Cys597 and Cys598 sulfur atoms forming a stable cyclic dithioarsinite<sup>13,14</sup>. This complex is effectively irreversible in biological milieu. There are very few appropriately spaced cysteine thiols in the extracellular environment so GSAO is largely unreactive until it crosses the plasma membrane. GSAO does not cross the intact plasma membrane of viable or early-stage apoptotic cells but enters mid- to late-stage apoptotic cells when the plasma membrane is compromised.

In this study we have investigated the utility of a near-infrared fluorescent conjugate of GSAO to non-invasively detect cell death in mouse brain cryolesions<sup>15-19</sup>. GSAO was conjugated to the near-infrared fluorophore, Alex Flour 750 (GSAO-

AF750), to maximize tissue penetration of the fluorescent signal and to minimize the complications of tissue auto-fluorescence<sup>20</sup>.

## Results

### GSAO-AF750 specifically labels apoptotic and necrotic cells in culture

Conjugation of AF750 to the primary amine of the  $\lambda$ -glutamyl residue of GSAO did not affect its capacity to specifically label dying cells. The specificity and sensitivity of labelling of dying/dead cells by AF750-tagged GSAO was examined in *in vitro* models of apoptotic (human Jurkat T cells treated with staurosporine) and necrotic (4T1-luc2 mouse breast cancer cells treated with dry ice) cell death. Staurosporine is a microbial alkaloid and broad spectrum protein kinase inhibitor that triggers mitochondrial-mediated apoptotic cell death, while snap freezing of cells ruptures the plasma membrane resulting in necrotic cell death. The probe was detected from the fluorescence intensity of the AF750 tag.

Apoptotic Jurkat T cells were labelled with the late stage apoptosis/necrosis marker, propidium iodide (PI), and either GSAO-AF750 or the phosphatidylserine ligand, PSVue<sup>®</sup>794<sup>18</sup>. GSAO-AF750 and PSVue<sup>®</sup>794 labelled dying and dead PI-positive cells in staurosporine treated samples (Fig. 1a). There were subpopulations of cells that labelled with PSVue<sup>®</sup>794 but not PI (Fig. 1a, top panels) and labelled with PI but not GSAO-AF750 (Fig. 1a, middle panels). PSVue<sup>®</sup>794, like annexinV, binds exteriorized phosphatidylserine on cell membranes of early- and late-stage apoptotic cells<sup>21</sup>, so the PSVue<sup>®</sup>794-positive, PI-negative population likely represents early stage apoptotic cells. The PI-positive cells that did not label with GSAO-AF750 possibly represents cell fragments that are devoid of the GSAO-AF750 ligand, Hsp-90.

The selectivity of GSAO-AF750 for dying and dead cells is mediated by the trivalent arsenic moiety. This was confirmed using two different controls. The synthetic dithiol, dimercaptopropanol (DMP), sequesters the trivalent arsenic moiety of GSAO, while GSCA-AF750 contains a chemically inert carboxylic acid group in place of the reactive trivalent arsenic moiety. Pre-treatment with DMP effectively ablated labelling of dying/dead cells by GSAO-AF750, but not by PSVue<sup>®</sup>794 (Fig. 1a, right panels). The mean GSAO-AF750 fluorescence intensity of PI-positive cells was ~60-fold less when cells were pre-treated with DMP. In addition, GSCA-AF750 did not label dying/dead PI-positive cells in staurosporine treated samples. The mean GSCA-AF750 fluorescence intensity of PI-positive cells was > 250-fold less than cells stained with GSAO-AF750 (Fig. 1a, bottom panels). Viable untreated cells did not stain with any of the compounds. These findings are consistent with our initial characterization of the compound<sup>11</sup> and are in accordance with its reaction with Hsp-90.

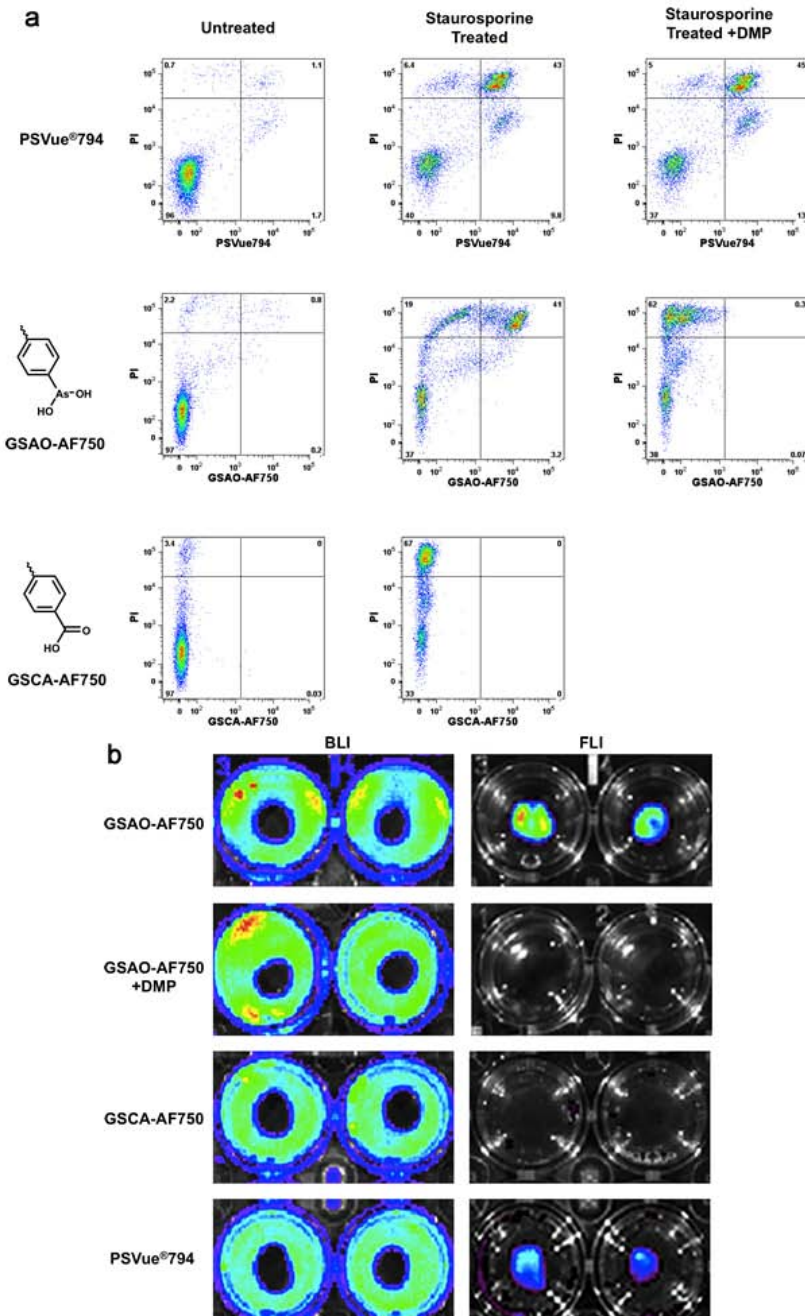


**Figure 1. GSAO-AF750 specifically labels apoptotic and necrotic cells in culture.** (a) Apoptotic death in Jurkat A3 T cells was triggered with staurosporine for 24 h and the cells subsequently incubated with PI (all panels) and either with PSVue<sup>®</sup>794 (upper panels), GSAO-AF750 (middle panels), or control GSCA-AF750 (lower panels) and labelling analysed by flow cytometry. In some samples (right panels), cells were pre-incubated with the trivalent arsenic ligand, DMP, prior to GSAO-AF750 or PSVue<sup>®</sup>794 staining. The numbers depicted in the scatter

plots represent the percentage of cells in the quadrants. (b) Necrotic death in confluent monolayers of 4T1-luc2 mouse breast cancer cells was induced by applying dry ice to the underside of the culture well and the cells subsequently incubated either with GSAO-AF750, GSCA-AF750 or PSVue<sup>®</sup>794. In some wells, cells were pre-treated with DMP prior to incubation with GSAO-AF750. Cells were imaged for fluorescence (right panels) and then for bioluminescence following by incubation with D-luciferin (left panels).

Necrotic 4T1 mouse breast cancer cells expressing the *luc2* luciferase reporter gene were incubated with either GSAO-AF750, GSCA-AF750 or PSVue<sup>®</sup>794. Necrotic cell death was induced by applying dry ice to the underside of the culture well, resulting in a discrete central region of dead cells surrounded by an external ring of healthy cells. The external ring of viable cells was imaged by bioluminescence following incubation with D-luciferin (Fig. 1b, indicated by blue/green). Necrotic cells are deficient in ATP, which is a substrate for the luciferin/luciferase reaction, so they do not emit light. Fluorescence imaging revealed that both GSAO-AF750 and PSVue<sup>®</sup>794, but not control GSCA-AF750, selectively labelled the area of dead cells in the centre of the well (Fig. 1b). Any probe did not stain the ring of healthy cells. Pre-treatment of the cultures with DMP totally abolished staining by GSAO-AF750.

## *In vivo* and *ex vivo* imaging of brain lesion cell death in mice with GSAO-AF750

The suitability of GSAO-AF750 for non-invasive imaging of apoptotic and necrotic cell death in the living animal was examined in a murine model of traumatic brain injury. A focal area of cell death is induced in the mouse brain by applying a liquid nitrogen insult to the skull<sup>5</sup>. The cryolesion is characterized by both apoptotic and necrotic cell death and shares many features with neurotrauma<sup>6,7</sup>.

A 60 sec brain cryolesion was induced in the front part of the right parietal lobe, followed by tail vein injection of GSAO-AF750 or GSCA-AF750 (1 mg/kg). Whole body fluorescence imaging was performed at 1, 3, 6 and 24 h after probe injection. GSAO-AF750 and GSCA-AF750 were, with the exception of the kidneys, eliminated from the body within 3 h of administration (Fig. 2a). Both compounds were observed to be excreted in the urine, in accordance with the kidney localization at earlier time points. A strong GSAO-AF750 signal, but not for control GSCA-AF750, was observed at all time points at the brain lesion site (Fig. 2a). In one mouse, a 3D sectional view was formed to depict the relative concentration of GSAO-AF750 in the brain lesion (Fig. 3). The GSAO-AF750 signal in brain lesions remained steady between 1 and 6 h after probe injection and dropped by 24 h (Fig. 2b). The control GSCA-AF750 signals were 50-100 fold lower than those obtained with GSAO-AF750 at all time points ( $p < 0.001$ ). The signal to background ratio for GSAO-AF750 (lesion versus adjacent healthy hemisphere) was approximately 3:1 at all time points.

The brains of the mice were excised for *ex vivo* imaging 24 h after probe injection. Accumulation of GSAO-AF750 in the lesion site was clearly evident (Fig. 2c). Some GSCA-AF750 was also detected in the lesion site, however the signal intensity was ~7-fold lower than that for GSAO-AF750 ( $p < 0.001$ ) (Fig. 2d).

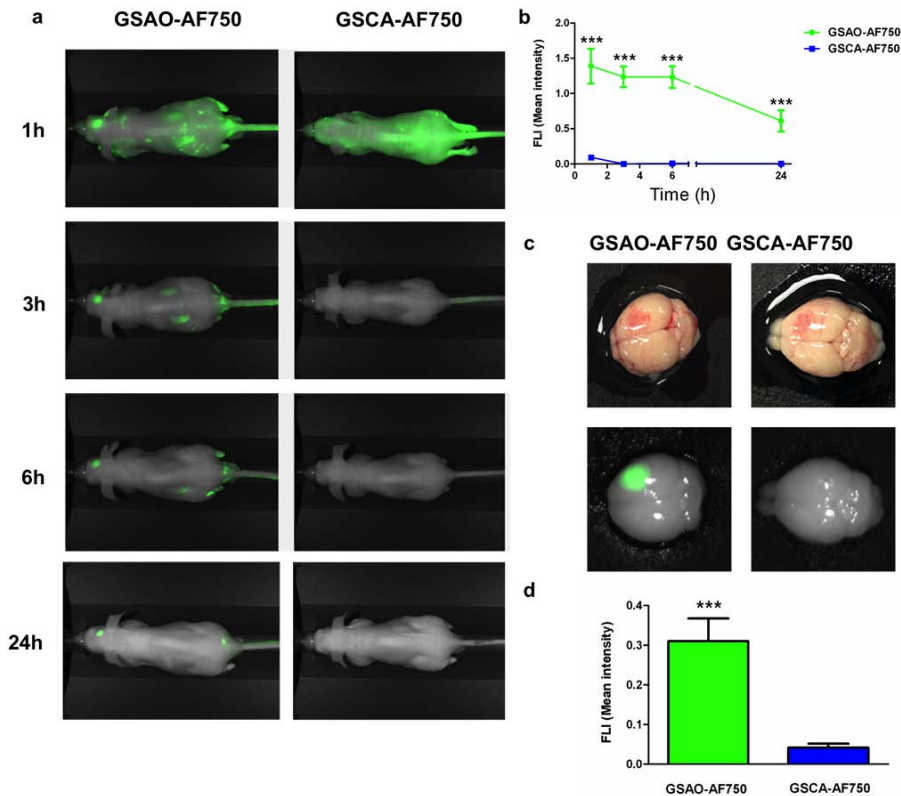


**Figure 2. In vivo and ex vivo imaging of brain lesion cell death in mice with GSAO-AF750.** (a) A 60 sec brain cryosection was induced in the front part of the right parietal lobe, followed by tail vein injection of 1 mg/kg GSAO-AF750 (left panels) or GSCA-AF750 (right panels) and whole body fluorescence imaging was performed at 1, 3, 6 and 24 h after probe injection. (b) Quantification of the integrated mean intensity of GSAO-AF750 and GSCA-AF750 signals in the brain lesion over time. GSAO-AF750 versus GSCA-AF750 intensities were calculated at 1, 3, 6 and 24 h (\*\*\*,  $p < 0.001$ ). (c) The brains of the mice were excised for *ex vivo* imaging 24 h after probe injection. Bright field images of a representative GSAO-AF750 and control GSCA-AF750 brain, showing a red discolouration of the lesion site, are shown in the top panel, while the fluorescence images of the same brains are shown in the bottom panel. (d) Quantification of the *ex vivo* integrated mean intensity of the AF750 signal. GSAO-AF750 versus GSCA-AF750 fluorescence intensity was calculated (\*\*\*,  $p < 0.001$ ).

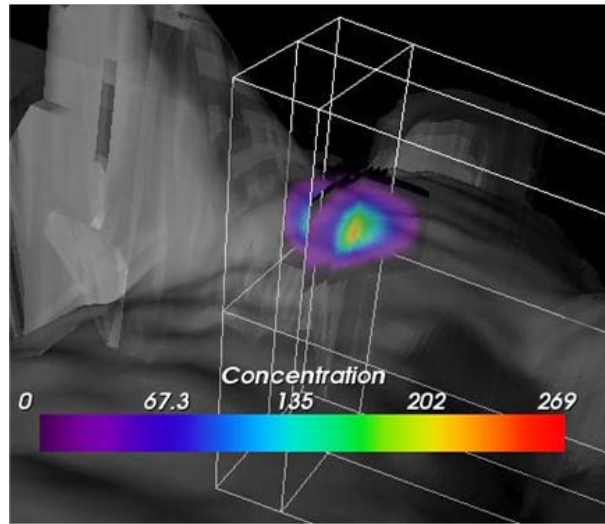


**Figure 3.** 3D sectional view depicting the relative concentration of GSAO-AF750 in a brain cryolesion. A concentration gradient of GSAO-AF750 radiates from the centre of the lesion.

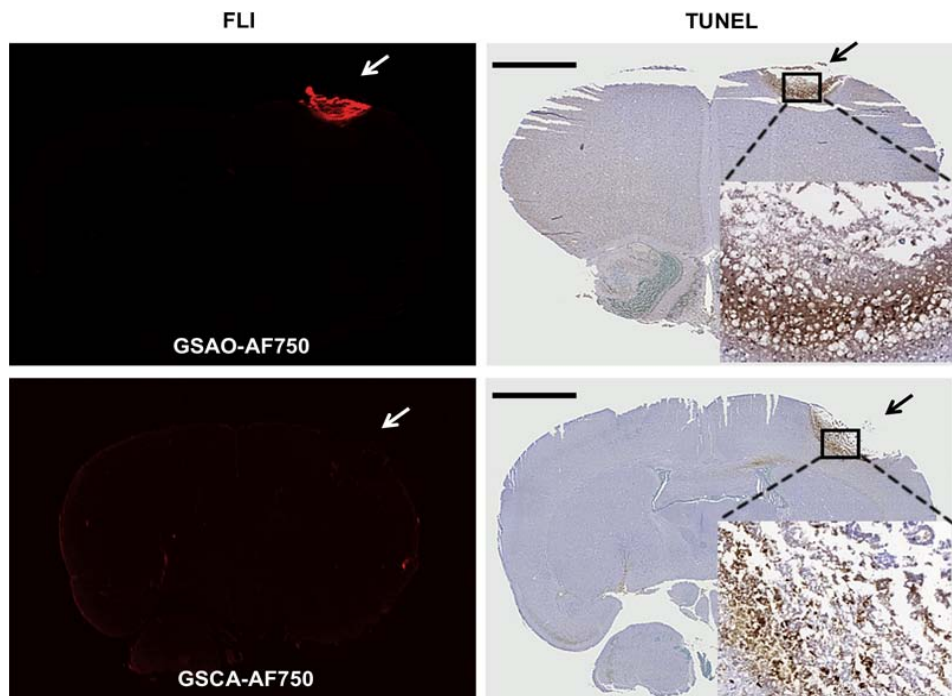


**Figure 4.** GSAO-AF750 labels dying/dead brain lesion cells in mice. The brains of mice subjected to a cryolesion were excised and sectioned 24 h after GSAO-AF750 or control GSCA-AF750 injection. The sections were examined for AF750 fluorescence (left panels) and cell death using TUNEL staining (right panels). GSAO-AF750, but not control GSCA-AF750, was observed in the lesion and co-localised with TUNEL-positive areas.

The specificity of GSAO-AF750 for dying and dead brain cells was confirmed *ex vivo* by analysis of brain sections. Fluorescence imaging and immunohistochemistry revealed co-localisation of GSAO-AF750 with TUNEL-positive cells in the cryolesion (Fig. 4).

## *In vivo* and *ex vivo* imaging of brain lesion cell death with GSAO-AF750 is a function of lesion size and probe concentration

The influence of brain lesion size and the dose of GSAO-AF750 on the signal intensity was evaluated. Mice bearing a 60 sec cryolesion were administered 0.1 or 1 mg/kg GSAO-AF750, and mice bearing a 5 sec cryolesion were administered 1 mg/kg GSAO-AF750 (Fig. 5a). All mice were imaged at 1, 3 and 6 h following probe injection. At all time points, total fluorescence intensity in the lesions of mice injected with 0.1 mg/kg GSAO-AF750 was 30- to 50-fold less than in those injected with 1 mg/kg GSAO-AF750 ( $p < 0.01$  at 1 and 6 h and  $p < 0.05$  at 3 h). In addition, the total fluorescence intensity of lesions in mice injected with 1 mg/kg GSAO-AF750 was ~5-fold lower in mice with a 5 sec cryolesion compared to those with a 60 sec cryolesion ( $p < 0.05$  at all time points). These findings were confirmed *ex vivo* by measuring the fluorescence intensity of the excised brains 6 h after GSAO-AF750 injection (Fig. 5b).

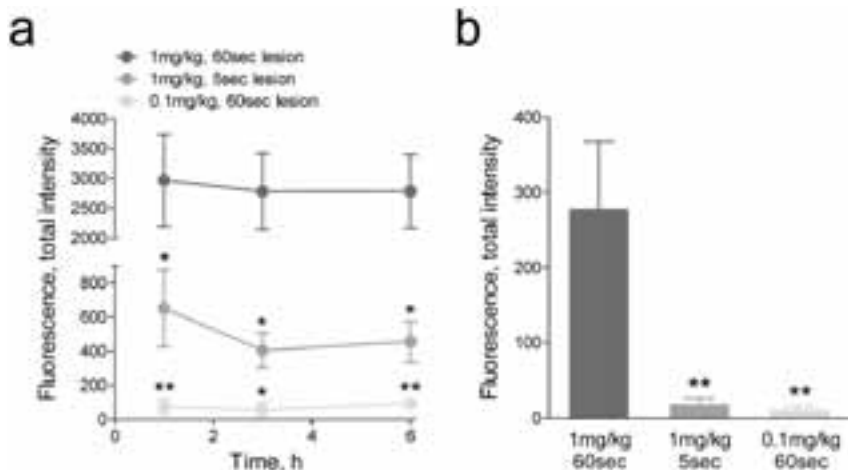


**Figure 5. In vivo and ex vivo imaging of brain lesion cell death with GSAO-AF750 is a function of lesion size and probe concentration.** (a) *In vivo* quantification of GSAO-AF750 signal intensity in the cryolesion over time. GSAO-AF750 fluorescence intensity was compared between mice bearing 5 s and 60 s cryolesions (\*\*,  $p < 0.01$ ; \*,  $p < 0.05$ ), or injected with a lower concentration of GSAO-AF750 (\*,  $p < 0.05$  at 1, 3 and 6 h). (b) The brains of the mice were excised for *ex vivo* imaging 6 h after probe injection and the integrated mean intensity of the AF750 signal was measured. GSAO-AF750 fluorescence intensity was significantly lower in brains bearing a 5 s cryolesion or injected with 0.1 mg/kg GSAO-AF750 (\*\*,  $p < 0.01$ ).

## Fluorescence lifetime imaging of GSAO-AF750 bound to dying/dead cells in culture and in brain lesions

The fluorescence lifetime of unbound GSAO-AF750 versus bound to dying/dead cells was measured in necrotic breast cancer cells and in brain cryolesions. The lifetime of free GSAO-AF750 and control GSCA-AF750 in phosphate buffered saline was 0.58-0.61 ns, while the weighted average single fluorescence lifetime of GSAO-AF750 lengthened to 0.89 ns when bound to necrotic breast cancer cells (Fig. 6a). Negative controls were no binding of GSAO-AF650 in the presence of DMP and no binding of GSCA-AF750 (Fig. 6a). A single exponential fit of the time point spread function curve produced a weighted average fluorescence lifetime of 0.97-1.05 ns for GSAO-AF750 in brain cryolesions (Fig. 6b), which is comparable to the lifetime measured in cultured dying/dead cells.

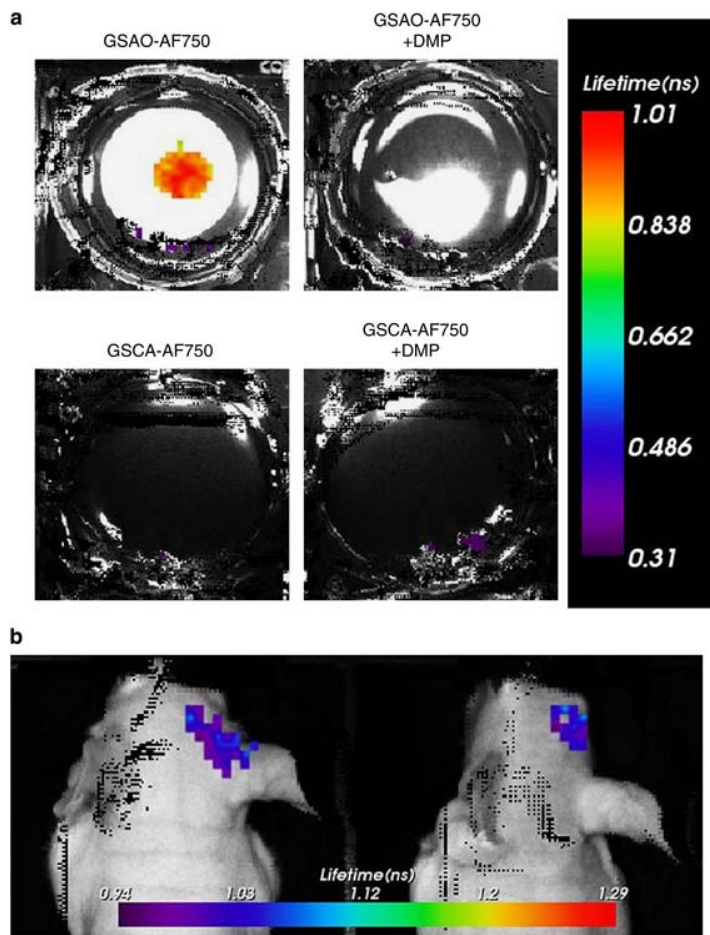


Figure 6. Fluorescence lifetime imaging of GSAO-AF750 bound to dying/dead cells. (a) Single exponential

---

fluorescence lifetime analysis of GSAO-AF750 labelling of dying/dead cells in culture. Focal cell death in confluent monolayers of 4T1-luc2 mouse breast cancer cells was induced by applying dry ice to the underside of the culture well and the cells subsequently incubated with GSAO-AF750 (top left well), GSAO-AF750 with DMP (top right well), GSCA-AF750 (bottom left well) or GSCA-AF750 with DMP (bottom right well). (b) Single exponential fluorescence lifetime analysis of GSAO-AF750 labelling of dying/dead cells in brain cryolesions of two different mice.

## Discussion

The effectiveness of a non-invasive imaging agent is mostly a product of the selectivity for its biological target and the volume of its distribution. Imaging sensitivity and resolution is enhanced when the reporter agent accumulates in high concentration in a small volume. We employed herein a small molecule that targets Hsp90 of apoptotic and/or necrotic cells.

Hsp90 is, in principle, an attractive imaging target as it is one of the most abundant proteins in the mammalian cell cytoplasm. Alkylation of Hsp90 by GSAO in dying/dead cells results in high concentration of the compound in the largest compartment of the cell<sup>11</sup>. This is in contrast to the ligands that target phosphatidylserine exposed on the exterior of the plasma membrane during apoptosis<sup>22-24</sup>, for instance, which are restricted to the cell surface compartment. Conjugation of the near-infrared fluorophore, AF750, to the  $\lambda$ -glutamyl amine of GSAO did not affect its specific labelling of apoptotic and necrotic cells in culture. In accordance with previous studies<sup>11</sup>, the labelling was a function of the dithiol alkylating chemistry of the As(III) moiety of GSAO-AF750.

Importantly, as shown herein, GSAO-AF750 has very favorable pharmacokinetics and biodistribution in mice. It is secreted via the renal circulation and does not accumulate in healthy organs or tissues. Three hours after intravenous administration it is found only in the kidneys. Less than optimal pharmacokinetics and biodistribution has limited the development of a number of cell death imaging agents to date. This has been the case for the protein ligands that recognize phosphatidylserine<sup>25,26</sup>, although a new generation of small molecule phosphatidylserine ligands may overcome these issues<sup>18,27</sup>.

GSAO-AF750 specifically labels dying and dead cells in brain cryolesions. The AF750 signal was apparent as early as one hour in the lesions and remained unchanged for approximately six hours. The signal to background ratio was  $\sim$ 3:1 at all time points and signal intensity was a function of both lesion size and probe concentration. The specificity of GSAO-AF750 for dying and dead brain cells was confirmed *ex vivo*. Notably, cells in the periphery of the brain lesion stained strongly by TUNEL, while cells in the centre stained weakly. This is indicative of the apoptotic and necrotic cells, respectively, in the lesion<sup>5</sup>. Both cell types in the lesion stained with GSAO-AF750, which is in accordance with the cell culture results showing that GSAO-AF750 labels both apoptotic and necrotic cells.

An advantage that optical agents can have over other reporter groups is a change in the fluorescence properties of the fluorophore when it is bound to its

target<sup>28-33</sup>. Alteration of the microenvironment of the fluorescent moiety upon target binding can result in a shortening or lengthening of the fluorescence lifetime. This difference can be used to distinguish between unbound and bound agent in the target tissue as it is independent of intensity variations or local concentrations of the fluorophore. The fluorescence lifetime of GSAO-AF750 increased from 0.58-0.61 to 0.89 ns when bound to necrotic breast cancer cells and to 0.97-1.05 ns when bound in brain cryolesions. The significantly longer fluorescence lifetime when bound to its target will be a useful parameter when optimizing the signal-to-background contrast in future studies that explore other experimental and clinical applications of GSAO-AF750.

Optical imaging technologies, including fluorescence-guided surgery and endoscopy, intravascular fluorescence imaging and photoacoustic applications in cardiovascular disease, dermatology and cancer, have advanced rapidly in recent years<sup>34,35</sup>. In the last decade, optical imaging has moved from gross assessment of structure and morphology to imaging of biological processes that underlie disease. Although, the development of the hardware to measure light in the human body has outpaced the development of specific probes that report on cellular events. GSAO-AF750 shows promise for the pre-clinical and clinical imaging of cell death in brain and other lesions.

## Acknowledgments

This study is supported by the Dutch Center for Translational Molecular Medicine, project MUSIS (grant 03O-202), the ENCITE project 201842, the National Health and Medical Research Council of Australia and the Cancer Council New South Wales.

## Materials and Methods

### Ethical statement

All animal experiments were approved for animal health, ethics, and research by the Animal Welfare Committee of Leiden University Medical Center, the Netherlands (Approval DEC number 11198). All the mice were purchased from Charles River Laboratories, France and received humane care and maintenance in compliance with the “Code of Practice Use of Laboratory Animals in Cancer Research” (Inspectie W&V, July 1999).

---

## Synthesis of near-infrared GSAO and GSCA conjugates

A solution of AF750 ( $\lambda_{\text{ex}}$ :752nm,  $\lambda_{\text{em}}$ :776nm) succinimidyl ester (10 mg/mL in DMSO, Invitrogen) was added to GSAO (4.2 mg/mL) or control 4-(N-((S-glutathionyl)acetyl)amino)benzoic acid (GSCA, 5.9 mg/mL), in 0.1 M bicarbonate buffer, pH 8.3 and incubated for 60 min in the dark in the presence of nitrogen. The molar ratio of fluorophore to pendant was  $\sim$ 1:1. Unreacted fluorophore was quenched by adding 10 mM glycine. The conjugate was separated from unreacted fluorophore by passing the reaction through at least two Sephadex G10 spin columns equilibrated with 0.1 M bicarbonate buffer, pH 8.3 (Sigma). The unreacted dye binds to the Sephadex matrix while the conjugate elutes in the void volume. Purity of the conjugates was confirmed by HPLC (1200 Series; Agilent Technologies) on a Zorbax Eclipse XDB-C18 column (4.6 x 150 mm, 5  $\mu$ m; Agilent Technologies) using a mobile phase of acetonitrile-water (25:75 vol/vol), flow rate of 0.5 mL per min and detection by absorbance at 256 nm. The conjugates were resolved from unreacted GSAO or GSCA by this method. Purity was also assessed by thin layer chromatography using a 3:1:1 butanol/acetic acid/water mobile phase. The purity of GSAO-AF750 and GSCA-AF750 was >95%.

## Cell culture

Jurkat A3 cells (ATCC) and mouse breast cancer cells 4T1-luc2 expressing the codon-optimized luciferase gene *luc2* (Caliper Life Sciences) were cultured in RPMI-1640 medium supplemented with 10% fetal bovine serum and 1 U/mL penicillin/streptomycin. All other cell culture reagents were from Gibco.

## *In vitro* validation of GSAO-AF750 and GSCA-AF750 via flow cytometry

Jurkat A3 cells were seeded at a density of  $5 \times 10^5$  cells per mL and incubated with or without 4  $\mu$ M staurosporine (Sigma) for 24 h. Cells were washed twice with ice cold phosphate-buffered saline and incubated at room temperature with 1  $\mu$ M GSAO-AF750 or control GSCA-AF750 for 15 min with shaking. Alternatively, cells were washed in phenol red free RPMI-1640 medium and stained with PSVue<sup>®</sup>794 (Polysciences, Inc), as per the manufacturer's instructions. On some occasions the cells were pre-treated with DMP (50  $\mu$ M, Sigma), for 1 min. Cells were washed again and incubated with PI (1  $\mu$ g/mL, Invitrogen) for 15 min in the dark. Flow cytometry was performed using a BD<sup>™</sup> LSR II Flow Cytometer with a

high power 200mW, 628 nm red excitation laser, a 40mW, 786nm near-infrared excitation laser and a 100mW, 488nm excitation laser (BD Biosciences). Data were analyzed using FlowJo software version 8.7.

## *In vitro* cryo-induced cell death assay

4T1-luc2 cells were seeded onto 12-well plates and grown to confluency in complete RPMI-1640 medium. The medium was discarded and a bar of dry ice 3-5 mm in diameter applied to the underside of the culture well for 15 sec. GSAO-AF750, GSCA-AF750, or PSVue<sup>®</sup>794 (0.4  $\mu$ M in 500  $\mu$ L medium) was added to the cells and incubated for 15 min at 37 °C. The cells were gently washed twice with phosphate-buffered saline and imaged using the IVIS Spectrum (Caliper Life Sciences) (excitation 710 nm, emission 780 nm). Subsequently, D-luciferin (150 mg/kg in 5  $\mu$ L PBS) (SynChem, Inc) was added to each well for 10 min and bioluminescence images acquired using the same machine. To complement the intensity measurements, fluorescence lifetime images of 4T1-luc2 cells on 12-well plates in the presence of GSAO-AF750 or control GSCA-AF750 were determined using a time domain optical imager (Optix MX3). Tubes of GSAO-AF750 and GSCA-AF750 in their free state were also scanned in order to establish a fluorescence lifetime reference for the subsequent *in vivo* studies.

## *In vivo* murine model of cryo-induced traumatic brain injury

A brain cryolesion was applied as described previously with minor modifications<sup>18</sup>. In short, six-week old male BALB/c nu/nu mice (Charles River Laboratories, France) were sedated with 2-3% isoflurane and a cryolesion induced in the parietal lobe of the right cerebral hemisphere. A metal rod of 3 mm in diameter was pre-cooled with liquid nitrogen and applied to the skull for 5 or 60 sec. Mice were allowed to recover from the anaesthetic and observed for any adverse symptoms resulting from the cryolesion. Mice were then injected intravenously with either GSAO-AF750 or control GSCA-AF750 (0.1 mg/kg or 1 mg/kg in 100  $\mu$ L PBS) and imaged with the Pearl<sup>®</sup> Impulse Small Animal Imaging System (LI-COR Biosciences) at 1, 3, 6 and 24 h. Prior to imaging mice were wiped with 70% v/v ethanol to remove any of the compounds excreted in the urine and contaminating the skin. At the experiment endpoint the mice were sacrificed by cervical dislocation and the brains excised for *ex vivo* fluorescence imaging. Images were acquired at 800 nm at a resolution of 85  $\mu$ m.

The fluorescent signal was digitized and electronically displayed as a pseudocolor overlay on a gray scale white light image of the animal. The data was analyzed using Pearl<sup>®</sup> Impulse Software, Version 2.0. Total AF750 fluorescence intensity was determined by drawing a region of interest (ROI) over the area in

---

which the cryolesion was induced. The size and shape of the ROI was the same for each time point. An ROI of equivalent size was then drawn over the adjacent hemisphere to determine the background signal and this was subtracted from the lesion signal. Where integrated mean fluorescence intensity of AF750 is shown, the value has been corrected for the area of the ROI. Results are depicted as mean  $\pm$  standard error of the mean. Statistical analysis was performed using a Student's t-test.

Whole mouse fluorescence imaging was performed using the Optix MX3. Animals were placed on a heated five-mouse bed imaging platform so that mice administered GSAO-AF750 and control GSCA-AF750 could be compared side-by-side. A 735 nm, 80 MHz pulse diode laser was used for excitation and raster-scanning, performed in 1 mm steps. Photon emission was captured by time-correlated single photon counting with a 755 nm long pass filter and data were recorded as temporal point spread functions. Image analysis and fluorescence lifetime calculations were performed using Optiview 3.0 software (ART). Rectangular ROIs were drawn around the head region to initially determine the single exponential fluorescence lifetime. This is the weighted average of all the fluorescence lifetime values.

## Histological validation

Brains were fixed in 4% formaldehyde, embedded in paraffin and 8  $\mu$ m sections were prepared and imaged using the LI-COR Odyssey Infrared Imager 9120 (LI-COR Biosciences) at 800 nm. Afterwards, the sections were subjected to TdT-mediated dUTP nick-end labelling (TUNEL) staining (Promega) to confirm accumulation of GSAO-AF750 in dying and dead cells.

## References

1. Faul, M., Xu, L., Wald, M.M. & Coronado, V.G. Traumatic brain injury in the United States: emergency department visits, hospitalizations, and deaths, 2002-2006. *National Center for Injury Prevention and Control, Centers for Disease Control and Prevention*, 1-71 (2010).
2. Thurman, D.J., Alverson, C., Dunn, K.A., Guerrero, J. & Sniezek, J.E. Traumatic brain injury in the United States: A public health perspective. *The Journal of head trauma rehabilitation* **14**, 602-615 (1999).
3. Werner, C. & Engelhard, K. Pathophysiology of traumatic brain injury. *British journal of anaesthesia* **99**, 4-9 (2007).
4. Kim, J.J. & Gean, A.D. Imaging for the diagnosis and management of traumatic brain injury. *Neurotherapeutics* **8**, 39-53 (2011).
5. Steinbach, J.P., Weissenberger, J. & Aguzzi, A. Distinct phases of cryogenic tissue damage in the cerebral cortex of wild-type and c-fos deficient mice. *Neuropathol. Appl. Neurobiol.* **25**, 468-480 (1999).
6. Meryman, H.T. Mechanics of freezing in living cells and tissues. *Science* **124**, 515-521 (1956).
7. Gage, A.A., Baust, J.M. & Baust, J.G. Experimental cryosurgery investigations in vivo. *Cryobiology* **59**, 229-243 (2009).
8. Wen, J., et al. Cryoablation induces necrosis and apoptosis in lung adenocarcinoma in mice. *Technol Cancer Res Treat* **6**, 635-640 (2007).
9. Margulies, S. & Hicks, R. Combination therapies for traumatic brain injury: prospective considerations. *J. Neurotrauma* **26**, 925-939 (2009).
10. Quintana, A., et al. Differential role of tumor necrosis factor receptors in mouse brain inflammatory responses in cryolesion brain injury. *Journal of neuroscience research* **82**, 701-716 (2005).
11. Park, D., et al. Noninvasive imaging of cell death using an Hsp90 ligand. *J Am Chem Soc* **133**, 2832-2835 (2011).
12. Nardai, G., Sass, B., Eber, J., Orosz, G. & Csermely, P. Reactive cysteines of the 90-kDa heat shock protein, Hsp90. *Arch. Biochem. Biophys.* **384**, 59-67 (2000).
13. Adams, E., Jeter, D., Cordes, A.W. & Kolis, J.W. Chemistry of Organometalloid Complexes with Potential Antidotes - Structure of an Organoarsenic(III) Dithiolate Ring. *Inorg Chem* **29**, 1500-1503 (1990).
14. Dilda, P.J. & Hogg, P.J. Arsenical-based cancer drugs. *Cancer treatment reviews* **33**, 542-564 (2007).
15. Grzybicki, D., et al. Expression of monocyte chemoattractant protein (MCP-1) and nitric oxide synthase-2 following cerebral trauma. *Acta Neuropathol* **95**, 98-103 (1998).
16. Hotta, N., et al. Expression of glia maturation factor beta after cryogenic brain injury. *Brain Res. Mol. Brain Res.* **133**, 71-77 (2005).
17. Siren, A.L., et al. Global brain atrophy after unilateral parietal lesion and its prevention by erythropoietin. *Brain* **129**, 480-489 (2006).
18. Smith, B.A., et al. Multicolor fluorescence imaging of traumatic brain injury in a cryolesion mouse model. *ACS Chem Neurosci* **3**, 530-537 (2012).
19. Stoffel, M., et al. Identification of brain tissue necrosis by MRI: validation by histomorphometry. *J. Neurotrauma* **21**, 733-740 (2004).
20. Xie, B.W., et al. Dual-wavelength imaging of tumor progression by activatable and targeting near-infrared fluorescent probes in a bioluminescent breast cancer model. *PLoS One* **7**, e31875 (2012).
21. Hanshaw, R.G. & Smith, B.D. New reagents for phosphatidylserine recognition and detection of apoptosis. *Bioorg. Med. Chem.* **13**, 5035-5042 (2005).
22. Blankenberg, F.G. In vivo imaging of apoptosis. *Cancer Biol Ther* **7**, 1525-1532 (2008).
23. Zhao, M. In vivo apoptosis imaging agents and strategies. *Anticancer Agents Med Chem* **9**, 1018-1023 (2009).
24. Niu, G. & Chen, X. Apoptosis imaging: beyond annexin V. *J. Nucl. Med.* **51**, 1659-1662 (2010).
25. Kahlem, P., Dorken, B. & Schmitt, C.A. Cellular senescence in cancer treatment: friend or foe? *The Journal of clinical investigation* **113**, 169-174 (2004).
26. Lederle, W., et al. Failure of annexin-based apoptosis imaging in the assessment of antiangiogenic therapy effects. *EJNMMI Res* **1**, 26 (2011).

- 
27. Beekman, C.A., *et al.* Questioning the value of (99m)Tc-HYNIC-annexin V based response monitoring after docetaxel treatment in a mouse model for hereditary breast cancer. *Applied radiation and isotopes : including data, instrumentation and methods for use in agriculture, industry and medicine* **69**, 656-662 (2011).
  28. Akers, W.J., Berezin, M.Y., Lee, H. & Achilefu, S. Predicting in vivo fluorescence lifetime behavior of near-infrared fluorescent contrast agents using in vitro measurements. *J Biomed Opt* **13**, 054042 (2008).
  29. Ardeshirpour, Y., *et al.* In vivo fluorescence lifetime imaging monitors binding of specific probes to cancer biomarkers. *PLoS One* **7**, e31881 (2012).
  30. Erten, A., *et al.* Enhancing magnetic resonance imaging tumor detection with fluorescence intensity and lifetime imaging. *J Biomed Opt* **15**, 066012 (2010).
  31. Goiffon, R.J., Akers, W.J., Berezin, M.Y., Lee, H. & Achilefu, S. Dynamic noninvasive monitoring of renal function in vivo by fluorescence lifetime imaging. *J Biomed Opt* **14**, 020501 (2009).
  32. Hall, D.J., *et al.* Dynamic optical imaging of metabolic and NADPH oxidase-derived superoxide in live mouse brain using fluorescence lifetime unmixing. *J. Cereb. Blood Flow Metab.* **32**, 23-32 (2012).
  33. Wang, J., *et al.* A novel brain metastases model developed in immunodeficient rats closely mimics the growth of metastatic brain tumours in patients. *Neuropathol. Appl. Neurobiol.* **37**, 189-205 (2011).
  34. Taruttis, A. & Ntziachristos, V. Translational optical imaging. *AJR. American journal of roentgenology* **199**, 263-271 (2012).
  35. Herron, T.J., Lee, P. & Jalife, J. Optical imaging of voltage and calcium in cardiac cells & tissues. *Circulation research* **110**, 609-623 (2012).







## CHAPTER FIVE

# Optical Imaging of Treatment-related Tumor Cell Death Using a Heat Shock Protein-90 Alkylator

Based on

Park D\*, Xie BW\*, Van Beek ER, Blankevoort V, Que I, Löwik CW, Hogg PJ.  
*Mol Pharm.* 2013 Aug 22. [Epub ahead of print].



## Abstract

The ability to assess in near-real time the tumor cell-killing efficacy of chemotherapy regimens would improve patient treatment and survival. An ineffective regimen could be abandoned early in favor of a more effective treatment. We sought to non-invasively image treatment-related tumor cell death in mice using an optically labelled synthetic heat shock protein-90 (Hsp90) alkylator, 4-(N-(S-glutathionylacetyl)amino)phenylarsonous acid (GSAO). The Hsp90 chaperone is an important element in oncogene addiction and tumor cell survival and its expression is enhanced by chemotherapy. These factors were predicted to favor the detection of tumor cell death using GSAO. Fluorescent conjugates of GSAO specifically labelled apoptotic and necrotic cancer cells in culture and a biotin conjugate of GSAO labelled cells of the same morphology in subcutaneous human pancreatic tumors in mice. A near-infrared conjugate of GSAO was further used to non-invasively image cyclophosphamide-induced tumor cell death in orthotopic murine mammary tumors in mice. The GSAO conjugate did not accumulate in healthy organs or tissues in the mouse and unbound compound was excreted rapidly via the kidneys. There was a significant increase in the GSAO fluorescence signal in the treated tumors measured either *in vivo* or *ex vivo* and the fluorescence signal co-localized with apoptotic cells in sectioned tumors. The favourable biodistribution of optically labelled GSAO, the nature of its tumor cell target and its capacity to non-invasively detect tumor cell death should facilitate the application of this compound in studies of the efficacy of existing and new chemotherapeutics.

## Keywords

Tumor cell death, chemotherapy, apoptosis, necrosis, GSAO, optical imaging

## Abbreviations

GSAA, 4-(N-(S-glutathionylacetyl)amino)phenylarsonic acid; GSAO, 4-(N-(S-glutathionylacetyl)amino)phenylarsonous acid; GSCA, 4-(N-((S-glutathionyl)acetyl)amino)benzoic acid; AF750, Alex Flour 750; Hsp90, heat shock protein 90; PI, propidium iodide; ROI, region of interest; TUNEL, TdT-mediated dUTP nick-end labelling

---

## Introduction

Cancer results from an imbalance between rates of cellular proliferation and survival in a given tissue. Successful treatment controls cancer cell growth by inhibiting cellular proliferation and/or promoting cell death. Cancer patients with metastatic disease are often treated with cytotoxic chemotherapy to control tumor burden and/or to prolong life. To determine if chemotherapy is working, tumor size is usually assessed by computed tomography after six to nine weeks of treatment. This measure is used in decisions about further treatment. Being able to rapidly assess tumor cell proliferation and death in response to treatment would improve the management of this disease <sup>1</sup>.

Technologies that monitor therapy response have and are being developed. The measure in the widest clinical use is <sup>18</sup>F-fluorodeoxyglucose-positron emission tomography (FDG-PET) <sup>1-3</sup>. FDG uptake *in vivo*, though, is a composite measure of several biological processes. Decreased FDG uptake by tumors can reflect decreased glucose utilization by viable tumor cells and/or tumor cell death <sup>4,5</sup>. Moreover, FDG is also taken up by inflammatory cells <sup>4</sup>. A robust, minimally invasive, and universally applicable measure of early tumor response to treatment would significantly enhance patient care and the pace of new pharmaceutical development <sup>1,6</sup>. By reporting on the efficacy of new cytotoxic drugs and possibly the toxicity of these drugs in other tissues, 'go/no go' decisions will be easier to make.

There has been a particular focus on the development of imaging agents that measure tumor cell death in response to treatment. Chemotherapy and radiotherapy can result in many different types of tumor cell death, including apoptosis, necrosis, autophagy, mitotic catastrophe and cell senescence <sup>7-9</sup>. Probes that detect exteriorized phosphatidylserine on the surface of apoptotic cells <sup>10-18</sup>, activated caspase-3/7 in apoptotic cells <sup>19</sup> and a ribonucleoprotein exposed during apoptotic and necrotic cell death <sup>20,21</sup> have been tested as indicators of treatment-related tumor cell death.

In this study we have tested an optically labelled small molecule alkylator of heat shock protein-90 (Hsp90) as an indicator of response to tumor treatment in mice. The *in principle* advantages of this compound is that it selectively recognizes both apoptotic and necrotic cell death and its tumor target, Hsp90, is an abundant cytoplasmic chaperone that plays a fundamental role in tumorigenesis. The Hsp90 chaperone machine protects a number of mutated and overexpressed oncoproteins from misfolding and degradation <sup>22,23</sup>. As such, it is considered an important factor in oncogene addiction and tumor cell survival. In addition, the cellular expression of Hsp90 increases in response to stresses such as hypoxia and chemotherapeutics in an attempt to restore cellular homeostasis <sup>22,23</sup>.

Hsp90 contains a Cys597, Cys598 dithiol in the C-terminal domain <sup>24</sup> and the sulphur atoms are involved in redox reactions in the cytoplasm <sup>25</sup>. The Hsp90

alkylator is a tripeptide trivalent arsenical called GSAO (4-(N-(S-glutathionylacetyl) amino)phenylarsonous acid). The As(III) atom of GSAO cross-links the Cys597, Cys598 dithiol of Hsp90, forming a stable cyclic dithioarsinite that is effectively irreversible in biological milieu. When tagged with optical or radio reporter molecules, GSAO specifically labels dying/dead cells. The compound accumulates in the cytosol of dying cells coincident with loss of plasma membrane integrity and is retained in the cytoplasm by reacting predominantly with Hsp90<sup>26</sup>. It has a favorable biodistribution in the living animal and is cleared quickly from the circulation via the kidneys<sup>27</sup>. In this study, a near-infrared conjugate of GSAO has been used to non-invasively image cyclophosphamide-induced cell death in breast carcinoma tumors in mice.

## Results

Fluorescent conjugates of GSAO have been shown to label apoptotic and necrotic cells<sup>26,27</sup>. We sought to confirm the specificity of this labelling using a T cell hybridoma cell line and to define the cellular distribution of the labelling. The cell death targeting specificity of GSAO in labelling dying/dead cells in culture was examined, followed by validating its targeting specificity in labelling apoptotic and necrotic tissues in solid tumors in mice.

### GSAO-OG specifically labels apoptotic and necrotic cells in culture

The microbial alkaloid, staurosporine, is a broad spectrum protein kinase inhibitor that activates the intrinsic/mitochondrial-mediated pathway of apoptotic cell death<sup>28,29</sup>, while freeze/thaw ruptures the plasma membrane resulting in necrotic cell death<sup>30</sup>.

Apoptotic and necrotic Jurkat T cells were labelled with GSAO-OG and the late stage apoptosis/necrosis marker, propidium iodide (PI). GSAO-OG labelled PI-positive cells resulting from both types of cell death (Fig. 1, upper panel). There were subpopulations of cells that labelled with GSAO-OG and not PI and vice versa, but these were <10% of the total cell population. The selectivity of GSAO-OG for apoptotic and necrotic cells is mediated by the trivalent arsenic moiety, as has been described previously<sup>26,27</sup>. This was confirmed using control GSCA-OG that contains a chemically inert carboxylic acid group in place of the reactive trivalent arsenic moiety. GSCA-OG did not label apoptotic or necrotic PI-positive cells (Fig. 1, lower panel).

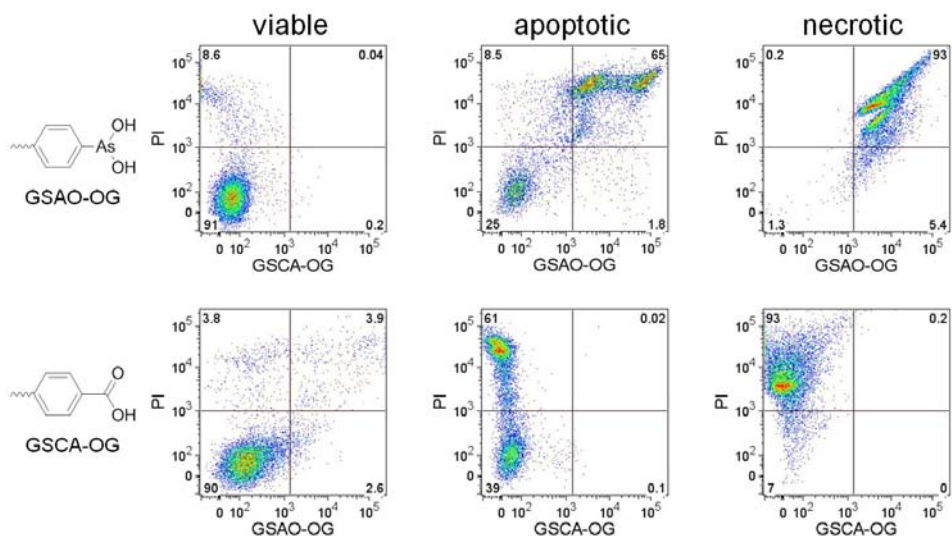


**Figure 1. GSAO-OG specifically labels apoptotic and necrotic cells in culture.** Apoptotic or necrotic death of Jurkat A3 T cells was triggered with staurosporine or freeze/thaw, respectively. The cells were subsequently incubated with PI (all panels) and either GSAO-OG (upper panels) or control GSCA-OG (lower panels) and labelling analysed by flow cytometry. The numbers depicted in the scatter plots represent the percentage of cells in the quadrants.

## GSAO-OG labels the cytoplasm of apoptotic and necrotic cells in culture

To determine the subcellular localization of GSAO-OG, apoptotic or necrotic Jurkat T cells were incubated with GSAO-OG, the phosphatidylserine ligand, annexin V-APC, and the nucleic acid stain, DAPI. The cells were imaged by confocal microscopy. GSAO-OG distributed in the cytoplasm of annexin V-positive apoptotic cells and the necrotic cell fragments resulting from freeze/thaw (Fig. 2). Only a few cell necrotic cell fragments labelled with annexin V, although most labelled with DAPI indicating the presence of nuclei.

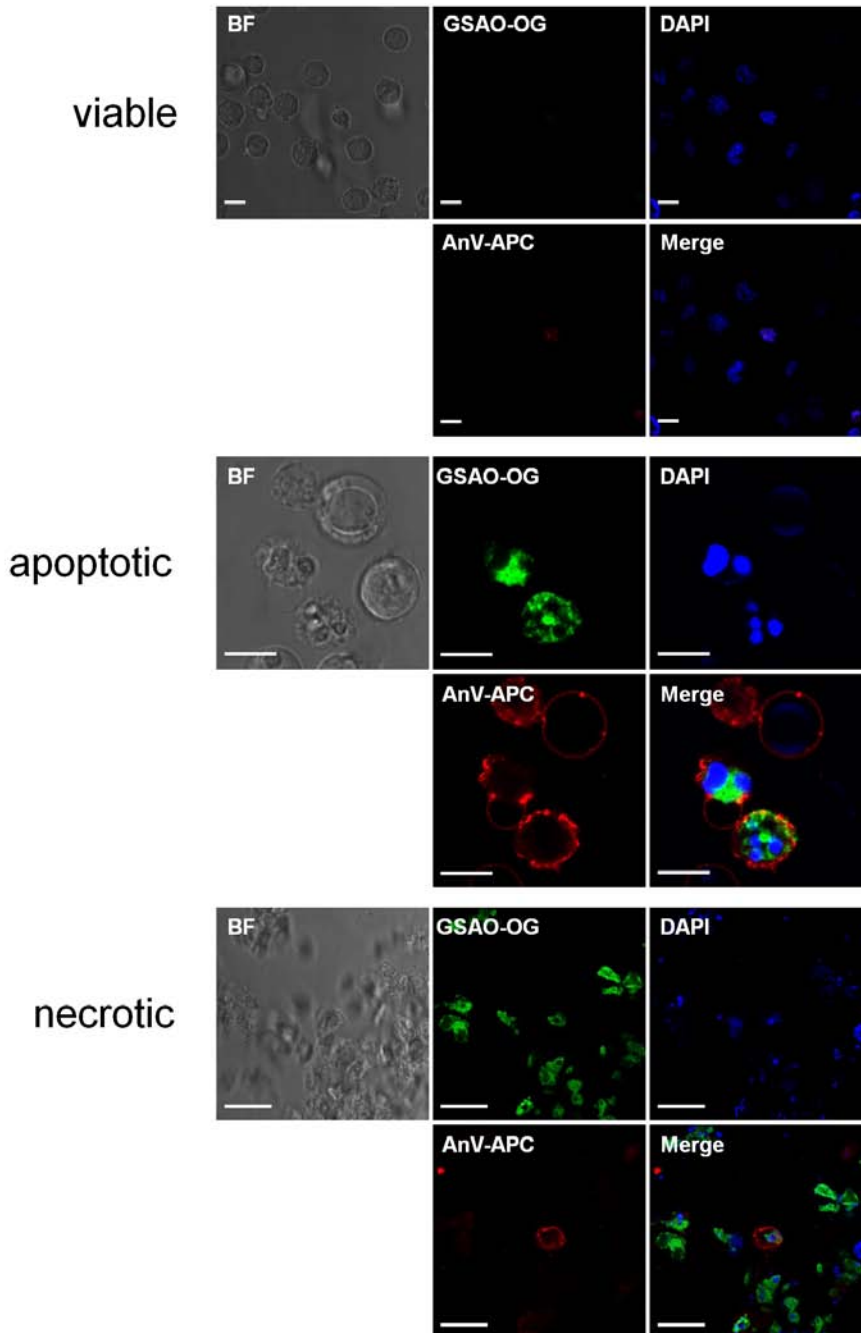


**Figure 2. GSAO-OG labels the cytoplasm of apoptotic and necrotic cells in culture.** Apoptotic or necrotic death of Jurkat A3 T cells was triggered with staurosporine or freeze/thaw, respectively. The cells were subsequently incubated with GSAO-OG (green), DAPI (blue) and annexin V-APC (red) and imaged by confocal microscopy. The bottom right-hand images are a merge of all three colors. The bar represents 20  $\mu\text{m}$ .

---

## GSAO-biotin labels tumor cells of apoptotic and necrotic morphology *in vivo*

We next sought to identify the morphology of GSAO-labelled cells in tumors. Biotin-tagged GSAO was administered to immunodeficient mice bearing subcutaneous human pancreatic carcinoma tumors. The tumors were excised 6 h later and sections stained for the biotin moiety of the label using streptavidin-peroxidase, and counterstained with haematoxylin to identify viable tumor cells. This method allowed for a better characterization of the tumor morphology and labelled regions that could be revealed using fluorescent conjugates of GSAO. There was an accumulation of GSAO-biotin in regions of the tumor where apoptotic and necrotic cells were prevalent (Fig. 3). GSAO-biotin stained cells that showed signs of apoptosis, including a condensed nucleus and shrunken cytoplasm, and cell fragments that resemble the necrotic fragments labelled by GSAO-OG in culture (see Fig. 2). There was no staining of viable tumor cells by GSAO-biotin. There was no detectable control GSAA-biotin in tumor sections from mice administered with this compound (not shown).

The capacity of an optically labelled GSAO to image treatment-related cell death in murine tumors was investigated. The treatment model was first established using immunodeficient mice bearing orthotopic mammary carcinoma tumors. This tumor model was selected for two reasons. First, orthotopic inoculation of 4T1 breast cancer cells can result in the spontaneous generation of lung, liver, bone and brain metastases, mimicking progression of the disease in humans<sup>31-33</sup>. Second, tumor growth in the mammary fat pad provides a more relevant microenvironment than subcutaneous models. This is particularly important with regard to the tumor vasculature, as tagged GSAO is administered intravenously, and the architecture and organization of the vascular network will influence probe dissemination and thus uptake. Variation in tumor vessel density, diameter and/or permeability has been observed in mouse models of renal cell carcinoma, melanoma, glioblastoma, mammary carcinoma, hepatoma and fibrosarcoma depending on the site of implantation<sup>32-35</sup>. The chemotherapeutic employed was cyclophosphamide, a DNA alkylating agent that is used to treat breast cancer<sup>35,36</sup>. This tumor treatment model, therefore, is a clinically relevant system in which to test GSAO imaging of tumor cell death.

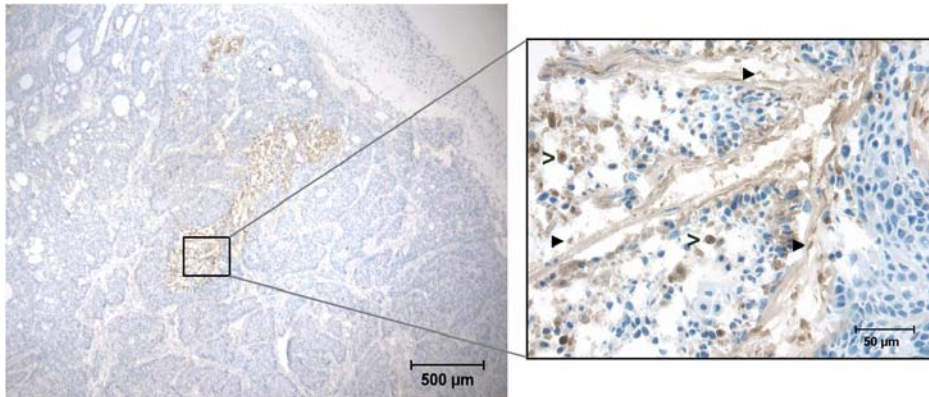


**Figure 3. GSAO-biotin labels tumor cells of apoptotic and necrotic morphology *in vivo*.** Mice bearing subcutaneous BxPC-3 tumors in the proximal dorsum were administered GSAO-biotin or control GSAA-biotin by subcutaneous injection in the hind flank. The tumors were excised after 6 h, sectioned and stained for GSAO-biotin using streptavidin-peroxidase (brown color) and co-stained with haematoxylin to reveal viable tumor cells (blue color). Shown is a low and high power micrograph of a sectioned tumor demonstrating incorporation of GSAO-biotin into cells of apoptotic (open arrowheads) and necrotic morphology (closed arrowheads). There was no detectable labelling of tumors with control GSAA-biotin.

## Establishment of the tumor treatment model

Nude mice bearing orthotopic 4T1-luc2 mammary carcinoma tumors were untreated or treated with a single intravenous injection of 250 mg/kg cyclophosphamide, and 24 h later the tumors were imaged by bioluminescence and then excised and weighed. There was a statistically significant reduction in the size of the treated tumors measured either *in vivo* by bioluminescence (Fig. 4A,  $p < 0.01$ ) or *ex vivo* by weight (Fig. 4B,  $p < 0.01$ ). There were no signs or symptoms of toxicity of the cyclophosphamide in this experimental design. This result indicated that the cyclophosphamide was impairing the proliferation and/or inducing death of the tumor cells over the 24 hour period. We then sought to non-invasively image the tumor cell death using the near infrared fluorescent conjugate of GSAO, GSAO-AF750.

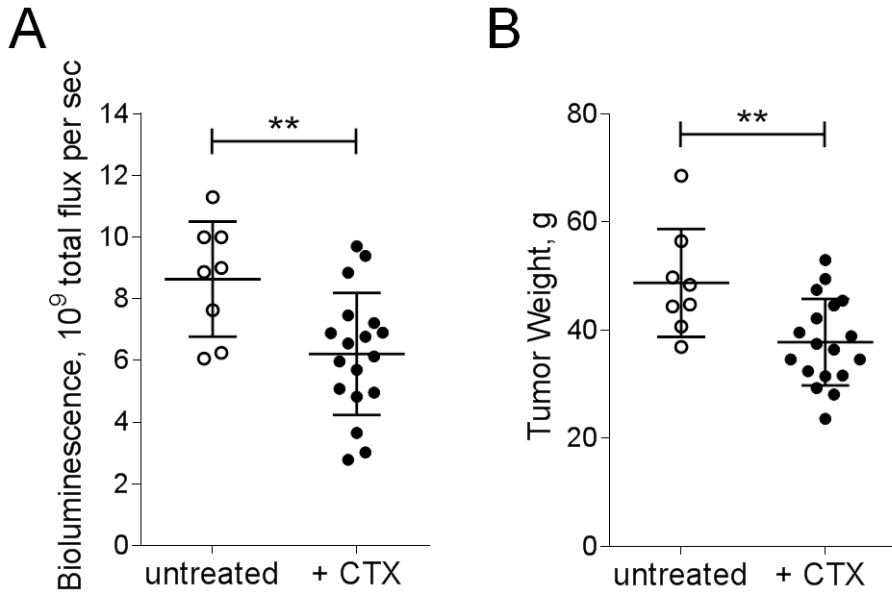


**Figure 4. Establishment of the tumor treatment model.** Nude mice bearing orthotopic 4T1-luc2 mammary carcinoma tumors were untreated or treated with 250 mg/kg cyclophosphamide (CTX). After 24 h, the mice were injected with D-luciferin and imaged for bioluminescent signals and then sacrificed and the tumors excised and weighed. Results are the mean  $\pm$  SD of a total of 18 mice from two separate experiments. \*\*,  $p < 0.01$ .

## Non-invasive imaging of treatment-related tumor cell death using GSAO-AF750

Nude mice bearing orthotopic 4T1-luc2 mammary carcinoma tumors were untreated or treated with 250 mg/kg cyclophosphamide for 24 h as described above. The mice then received a tail vein injection of either 1 mg/kg GSAO-AF750 or control GSCA-AF750 and 60 min later whole body fluorescence images were acquired (Fig. 5A). The tumors were excised three hours later and fluorescence images acquired *ex vivo*. There was a statistically significant increase in the GSAO-AF750 signal in the treated tumors measured either *in vivo* (Fig. 5B,  $p < 0.01$ ) or *ex vivo* three hours later (Fig. 5C,  $p < 0.05$ ). The signal from control GSCA-AF750 in treated tumors was substantially lower in both settings (Fig. 5B and C,  $p < 0.001$ ).

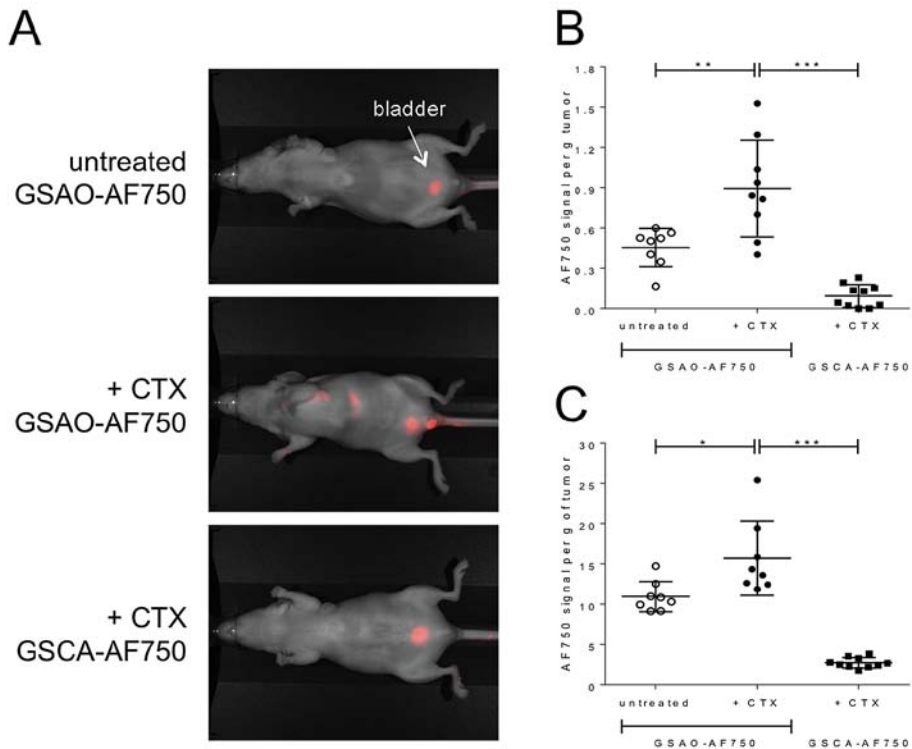


**Figure 5. Non-invasive imaging of treatment-related tumor cell death using GSAO-AF750.** Nude mice bearing orthotopic 4T1-luc2 mammary carcinoma tumors were untreated or treated with 250 mg/kg cyclophosphamide (CTX). After 24 h, the mice were injected with either GSAO-AF750 or control GSCA-AF750, and whole body fluorescence images of the mice were acquired 60 min later. Three hours later the tumors were excised and fluorescence values acquired *ex vivo*. A. Representative fluorescence images of whole mice. A fluorescence signal is observed in the treated tumor and in the kidneys/bladders of all mice, where GSAO-AF750 is excreted. B. Quantitation of the *in vivo* tumor fluorescent intensity, expressed as AF750 signal intensity per gram of tumor. C. Quantitation of the *ex vivo* tumor fluorescent intensity, expressed as AF750 signal per gram of tumor. Results are the mean  $\pm$  SD of a total of 10 mice from two separate experiments. \*\*\*,  $p < 0.001$ ; \*\*,  $p < 0.01$ ; \*,  $p < 0.05$ .

## GSAO-AF750 labels apoptotic cells in the mammary carcinoma tumors

The excised tumors from the experiment described above were sectioned and apoptotic cells visualised by TUNEL staining or with an antibody that recognises activated caspase-3. TUNEL-positive regions of the untreated and treated tumors were strongly positive for GSAO-AF750, which was more pronounced in the treated tumors (Fig. 6A). Individual apoptotic tumor cells were co-labelled with activated caspase-3 antibody staining and GSAO-AF750 (Fig. 6B). There was no labelling of tumors with control GSCA-AF750 (Fig. 6A and B).

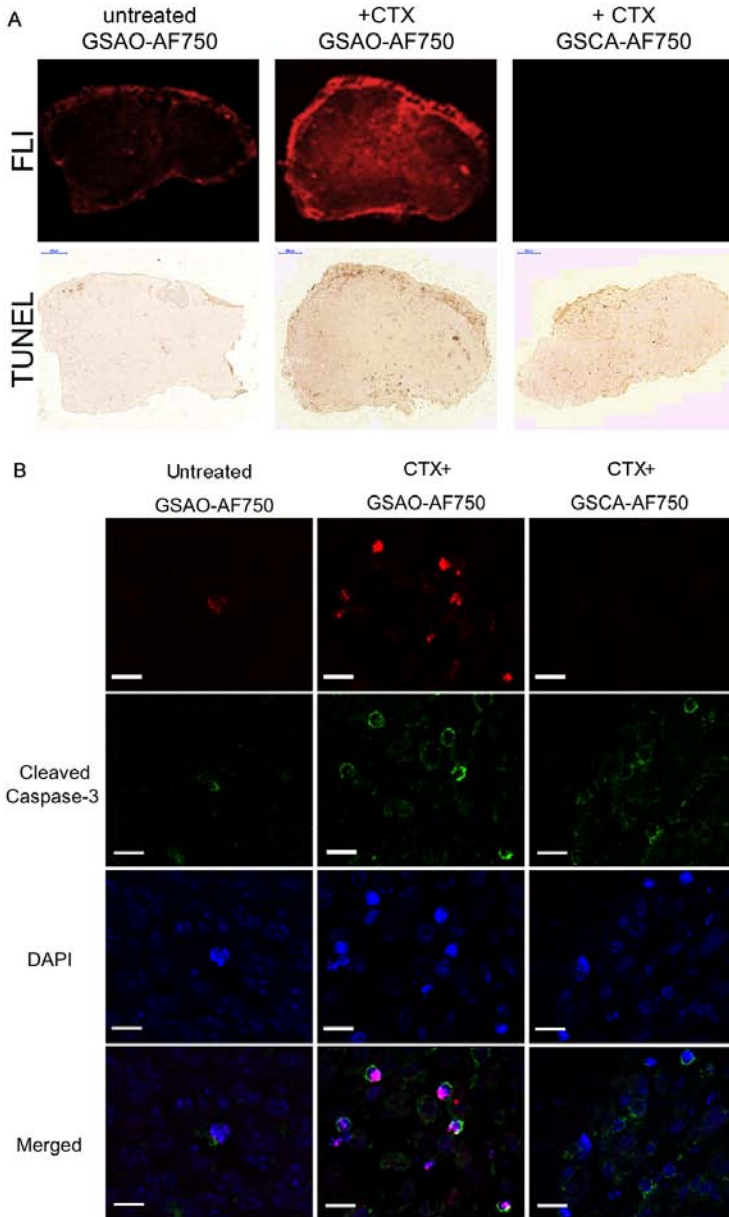


**Figure 6. GSAO-AF750 labels apoptotic cells in the mammary carcinoma tumors.** Nude mice bearing orthotopic 4T1-luc2 mammary carcinoma tumors were untreated or treated with 250 mg/kg cyclophosphamide (CTX). After 24 h, the mice were injected with either GSAO-AF750 or control GSCA-AF750, and three hours later the tumors were excised. Tumors were sectioned and apoptotic cells visualized by TUNEL staining or with an anti-activated caspase-3 antibody. Cell nuclei were stained with DAPI. A. Whole tumor sections showing the co-localization between GSAO-AF750 fluorescence and TUNEL-positive regions. B. Consecutive tumor sections showing co-labelling of cells with GSAO-AF750 and activated caspase-3 antibody. There was no labelling of tumors with control GSCA-AF750. The bar represents 40  $\mu$ m.

## Discussion

A robust and universally applicable measure of early tumor response to treatment would be a valuable tool for patient care and new pharmaceutical discovery, however there are challenges in developing this technology. The main issues are a cell death marker with the appropriate specificity, sensitivity and biodistribution, the nature and timing of the treatment-induced cell death, and distinguishing between the basal and treatment-related tumor cell death. These challenges will be considered in turn.

Phosphatidylserine is exposed on the exterior of the plasma membrane during apoptosis and four different phosphatidylserine ligands have been evaluated for the measurement of treatment-related tumor cell death. The first of these is the protein annexin V, which binds to phosphatidylserine in the presence of calcium ions<sup>37</sup>. An optically and radiolabelled annexin V has been evaluated in mice<sup>10-13</sup>. Some factors that have limited the adoption of annexin V include its large size (>35 kDa), which can result in slow delivery and clearance from the cells of interest, and high renal uptake. The C2A domain of synaptotagmin I binds phosphatidylserine and a radiolabelled molecule has been evaluated using SPECT<sup>14</sup> and MRI<sup>15</sup> imaging. Although the smaller size of this agent (~15 kDa) improves the penetration of tumor tissue, it binds phosphatidylserine with at least two orders of magnitude lower affinity than annexin V and has high hepatic and renal uptake that precludes imaging in the abdominal region. The third agent is zinc(II)-dipicolylamine that binds phosphatidylserine comparably to annexin V and has lower renal uptake, although it also binds bacteria<sup>16,17</sup>. A radiolabelled 14-residue phosphatidylserine-binding peptide has also been developed that labels melanoma tumors in mice and uptake is increased following paclitaxel treatment<sup>18</sup>. A general issue with the phosphatidylserine ligands is cross-reactivity with exteriorised phosphatidylserine in activated platelets, macrophages, endothelial cells and aging erythrocytes. Non-tumor cells under stress, such as hypoxia, will also transiently expose phosphatidylserine, which could lead to overestimation of tumor cell death.

Caspases are cysteine proteases that cleave a range of key structural proteins during the execution phase of apoptosis<sup>38</sup>. Caspase-3 is a central effector caspase in the demolition and clearance of apoptotic cells<sup>39</sup>. A radiolabelled small molecule inhibitor of activated caspase-3/7, an isatin-5 sulfonamide called ICMT-11, has been used to image treatment-related lymphoma cell death in mice by PET<sup>19</sup>. High hepatic uptake of the agent precludes imaging of abdominal region, though, and there is possible cross-reactivity with cathepsins. La antigen is involved in different aspects of RNA metabolism and during apoptosis translocates from the nucleus to cytoplasm<sup>40</sup>, where it is fixed in dying cells by transglutaminase 2<sup>20</sup>. Cytoplasmic La becomes accessible to antibodies when the integrity of the plasma membrane is compromised during the late phase of apoptosis<sup>20,21</sup>. A radiolabelled anti-La antibody has been developed (APOMAB) that shows promise for SPECT

---

imaging of tumor cell death in response to DNA damaging agents<sup>20,21</sup>. In this study, our immunohistology staining of treated tumor sections showed that even there was certain level of co-labelling between GSAO-AF750 and activated caspase-3, there were more cells with caspase-3 staining, indicating that GSAO-AF750 more specifically located in the late apoptotic and/or necrotic cells. This result confirms our previous study that GSAO that accumulates in the cytosol of dying and dead cells, coincident with loss of plasma membrane integrity<sup>26</sup>.

Optically tagged GSAO appears to overcome some of the disadvantages of these agents. It is highly selective for both apoptotic and necrotic cells and is rapidly cleared from the mouse body, being only found in the kidneys and bladder 3 h after intravenous administration to healthy animals<sup>27</sup>. In addition, the abundance of Hsp90 in the cytoplasm leads to high accumulation of GSAO in dying/dead cells, which results in good imaging sensitivity and resolution. The ligands that target phosphatidylserine exposed on the exterior of the plasma membrane during apoptosis, for example, are restricted to the cell surface compartment.

For wide applicability, a tumor cell death marker should ideally report on the different types of cell death mediated by different treatments. The phosphatidylserine and activated caspase-3 ligands were designed to image apoptotic cell death, although there is likely some cross-recognition of necrotic cell death<sup>37</sup>. The anti-La antibody and GSAO recognize both apoptotic and necrotic cell death, however the anti-La antibody may only image tumor cell death mediated by DNA damaging agents<sup>20,21</sup>. To our knowledge, there are currently no agents that image treatment-mediated tumor cell autophagy, mitotic catastrophe or cell senescence.

Perhaps the greatest challenge for this technology, though, is reliably distinguishing between basal and treatment-related cell death. Solid tumors generally contain large numbers of dying and dead cells, which is due to the naturally high rate of tumor cell death coupled with slow rate of clearance of dying and dead cells from tumors. In this study, cyclophosphamide treatment of the mammary carcinoma tumors resulted in a ~2-fold increase in tumor cell death as reported by GSAO-AF750. There was significant basal tumor cell death as indicated by the difference between GSAO-AF750 and control GSCA-AF750 labelling and the basal tumor cell death was also shown in the TUNEL staining (Fig. 6A). This magnitude of increase is in the range of other studies using different tumor treatment models and different cell death probes<sup>10-21</sup>.

A ~10-fold differential between basal and treatment-induced tumor cell death is perhaps required before an unambiguous assessment of treatment efficacy can be made. A solution to this problem may lie in suppressing the signal from basal tumor cell death. For instance, unlabelled (or cold) GSAO could be administered a day before treatment, which would block the Hsp90 binding sites in the basal dying/dead cells and allow for clearance of the compound from the

body. The day after treatment, tagged GSAO could be administered to detect the treatment-related cell death plus any basal cell death since treatment. The differential between basal and treatment-induced tumor cell death is predicted to be greater than that observed without the pre-blocking. This hypothesis will be tested in future studies. This scenario could also be applied to other cell death imaging agents.

## Materials and Methods

### Conjugates of GSAO, GSCA and GSAA

Conjugates of GSAO, GSCA and GSAA with Oregon Green 488 ( $\lambda_{\text{ex}}$ :496 nm,  $\lambda_{\text{em}}$ :542 nm), Alex Flour 750 ( $\lambda_{\text{ex}}$ :752 nm,  $\lambda_{\text{em}}$ :776 nm) or Biotin-XX, SE (Life Technologies, Victoria, Australia) were made and tested for purity as described previously<sup>26,27,41</sup>.

### Labelling or apoptotic and necrotic cells with GSAO-OG

Jurkat A3 cells (ATCC, Manassas, VA) were cultured in RPMI-1640 medium supplemented with 10% fetal bovine serum and 1 U/mL penicillin/streptomycin. The cells were seeded at a density of  $5 \times 10^5$  cells per mL and untreated or incubated with 4  $\mu\text{M}$  staurosporine (Sigma) for 24 h or freeze/thawed 3 times. Cells were washed twice with ice cold phosphate-buffered saline and incubated at room temperature with 1  $\mu\text{M}$  GSAO-OG or control GSCA-OG for 15 min with shaking. Cells were washed again and incubated with PI (1  $\mu\text{g}/\text{mL}$ , Invitrogen) for 10 min in the dark. Flow cytometry was performed using a FACS Canto II Flow Cytometer (Becton Dickinson, Franklin Lakes, NJ) and data analyzed using FlowJo software version 8.7.

### Confocal microscopic analysis of apoptotic and necrotic cells

Jurkat A3 cells were prepared as above and then incubated in 10 mM Hepes, pH 7.4 buffer containing 0.14 M NaCl and 2.5 mM  $\text{CaCl}_2$  and 5  $\mu\text{L}$  per 100  $\mu\text{L}$  annexin V-APC (Becton Dickinson). Cells were washed twice and then incubated with DAPI/AntiFade Reagent-Prolong Gold (Life Technologies). Cells ( $1 \times 10^5$ ) were transferred into FD35-100 Fluorodish Cell Culture Dishes (Coherent Scientific, South Australia, Australia) and images captured using a Leica TCS SP5 inverted laser-scanning confocal microscope running Leica LAS software.

---

## Labelling of apoptotic/necrotic tumor cells in mice with GSAO-biotin

Human pancreatic carcinoma Bx-PC3 cells (ATCC) were cultured in RPMI-1640 medium supplemented with 10% fetal bovine serum and 1 U/mL penicillin/streptomycin. A suspension of  $2.5 \times 10^6$  cells in 0.2 mL of phosphate-buffered saline was injected subcutaneously in the proximal midline dorsum of BALB/c *nu/nu* mice (Biological Resources Centre, University of New South Wales, Sydney). Tumors were allowed to establish and grow to a size of  $\sim 1 \text{ cm}^3$  after which the mice were administered 36 mg/kg GSAO-biotin or control GSAA-biotin in 0.2 mL of phosphate-buffered saline containing 20 mM glycine by subcutaneous injection in the hind flank. Mice were sacrificed 6 h later and tumors were embedded in OCT compound (Sakura, Torrance, CA) and snap frozen in liquid nitrogen. Sections ( $5 \mu\text{m}$ ) of the tumors were fixed with acetone and stained with StreptABComplex/HRP (Dako Corporation, Carpinteria, CA) according to the manufacturer's instructions. The sections were counterstained with haematoxylin and mounted with fluoromount-G (Southern Biotechnology, Birmingham, AL).

## Non-invasive imaging of treatment-related tumor cell death

Mammary carcinoma 4T1-luc2 cells expressing the codon-optimized luciferase gene *luc2* (Perkin Elmer, Hopkinton, MA) were cultured in RPMI-1640 medium supplemented with 10% fetal bovine serum and 1 U/mL penicillin/streptomycin. A suspension of  $0.5 \times 10^6$  cells in 0.1 mL of phosphate-buffered saline was injected orthotopically beneath the mammary fat pad in six-week old female BALB/c *nu/nu* mice (Charles River Laboratories, France). Seven days post tumor cell implantation mice were randomized into three groups and two groups were treated with a single tail vein injection of 250 mg/kg cyclophosphamide. The following day the mice were administered GSAO-Alexa Fluor 750 or control GSCA-Alexa Fluor 750 (1 mg/kg in 0.1 mL of phosphate-buffered saline) in the tail vein and imaged with the Pearl<sup>®</sup> Impulse Small Animal Imaging System (LICOR Biosciences, Lincoln, NE) 1 h later. Prior to imaging, the mice were wiped with 70% v/v ethanol to remove any of the compounds excreted in the urine and contaminating the skin. At the experiment endpoint, the mice were sacrificed by cervical dislocation and the tumors excised for *ex vivo* fluorescence imaging. Images were acquired at 800 nm at a resolution of  $85 \mu\text{m}$ . The fluorescent signal was digitized and electronically displayed as a pseudocolor overlay on a gray scale white light image of the animal. The data was analyzed using Pearl<sup>®</sup> Impulse Software, Version 2.0. Total AF750 fluorescence intensity was determined by drawing a ROI over the tumor. A ROI of equivalent size was then drawn over the adjacent breast to determine the background signal and this was subtracted

from the lesion signal. Tumor volume was calculated using the relationship: width x length x height x 0.523.

For bioluminescence imaging, mice received an intraperitoneal injection of 150 mg/kg D-luciferin (SynChem, Inc., Elk Grove Village, IL) in 50  $\mu$ L of phosphate-buffered saline, and 10 min later were imaged using the IVIS Spectrum (Perkin Elmer, Hopkinton, MA). At the experiment endpoint the mice were sacrificed by cervical dislocation and the tumors were then excised and weighed for statistical analysis.

## *Ex vivo* analysis of tumor labelling

The tumors were fixed in 4% formaldehyde, embedded in paraffin and 8  $\mu$ m sections were prepared and imaged using the LI-COR Odyssey Infrared Imager 9120 (LI-COR Biosciences, Lincoln, NE) at 800 nm. Afterwards, the sections were subjected to TUNEL staining (DeadEnd™ Colorimetric TUNEL System, Promega Benelux, Leiden, The Netherlands) to identify the apoptotic cells. Consecutive sections were also stained for activated caspase-3 using 5A1E rabbit monoclonal antibody (Cell Signaling, Leiden, The Netherlands) and Alexa Fluor 488° Donkey anti-rabbit IgG (Invitrogen, Breda, The Netherlands), and for nuclei using DAPI (Invitrogen, Breda, The Netherlands).

## Ethical statement

All animal experiments were approved for animal health, ethic and research by the Animal Welfare Committee of Leiden University Medical Center, the Netherlands (Approval DEC number 11198). All mice were purchased from Charles River Laboratories, France and received humane care and maintenance in compliance with the “Code of Practice Use of Laboratory Animals in Cancer Research” (Inspectie W&V, July 1999).

## Statistical analysis

We used two-tailed, unpaired Student’s t-test.

## Acknowledgments

This study is supported by the Dutch Center for Translational Molecular Medicine, project MUSIS (grant 03O-202), the National Health and Medical Research Council of Australia and the Cancer Council New South Wales.

---

## References

1. Weber, W.A., Czernin, J., Phelps, M.E. & Herschman, H.R. Technology Insight: novel imaging of molecular targets is an emerging area crucial to the development of targeted drugs. *Nature clinical practice. Oncology* **5**, 44-54 (2008).
2. Larson, S.M. & Schwartz, L.H. 18F-FDG PET as a candidate for "qualified biomarker": functional assessment of treatment response in oncology. *J. Nucl. Med.* **47**, 901-903 (2006).
3. Shankar, L.K., et al. Consensus recommendations for the use of 18F-FDG PET as an indicator of therapeutic response in patients in National Cancer Institute Trials. *J. Nucl. Med.* **47**, 1059-1066 (2006).
4. Workman, P., et al. Minimally invasive pharmacokinetic and pharmacodynamic technologies in hypothesis-testing clinical trials of innovative therapies. *J. Natl. Cancer Inst.* **98**, 580-598 (2006).
5. Su, H., et al. Monitoring tumor glucose utilization by positron emission tomography for the prediction of treatment response to epidermal growth factor receptor kinase inhibitors. *Clin. Cancer Res.* **12**, 5659-5667 (2006).
6. Weissleder, R. & Pittet, M.J. Imaging in the era of molecular oncology. *Nature* **452**, 580-589 (2008).
7. Johnstone, R.W., Ruefli, A.A. & Lowe, S.W. Apoptosis: a link between cancer genetics and chemotherapy. *Cell* **108**, 153-164 (2002).
8. Brown, J.M. & Attardi, L.D. The role of apoptosis in cancer development and treatment response. *Nat Rev Cancer* **5**, 231-237 (2005).
9. Kahlem, P., Dorken, B. & Schmitt, C.A. Cellular senescence in cancer treatment: friend or foe? *J. Clin. Invest.* **113**, 169-174 (2004).
10. Schellenberger, E.A., et al. Optical imaging of apoptosis as a biomarker of tumor response to chemotherapy. *Neoplasia* **5**, 187-192 (2003).
11. Dechsupa, S., et al. Quercetin, Siamois 1 and Siamois 2 induce apoptosis in human breast cancer MDA-mB-435 cells xenograft in vivo. *Cancer Biol Ther* **6**, 56-61 (2007).
12. Beekman, C.A., et al. Questioning the value of (99m)Tc-HYNIC-annexin V based response monitoring after docetaxel treatment in a mouse model for hereditary breast cancer. *Applied radiation and isotopes : including data, instrumentation and methods for use in agriculture, industry and medicine* **69**, 656-662 (2011).
13. Lederle, W., et al. Failure of annexin-based apoptosis imaging in the assessment of antiangiogenic therapy effects. *EJNMMI Res* **1**, 26 (2011).
14. Wang, F., et al. Imaging paclitaxel (chemotherapy)-induced tumor apoptosis with 99mTc C2A, a domain of synaptotagmin I: a preliminary study. *Nucl. Med. Biol.* **35**, 359-364 (2008).
15. Zhao, M., Beaugard, D.A., Loizou, L., Davletov, B. & Brindle, K.M. Non-invasive detection of apoptosis using magnetic resonance imaging and a targeted contrast agent. *Nat Med* **7**, 1241-1244 (2001).
16. Smith, B.A., et al. Optical imaging of mammary and prostate tumors in living animals using a synthetic near infrared zinc(II)-dipicolylamine probe for anionic cell surfaces. *J Am Chem Soc* **132**, 67-69 (2010).
17. Smith, B.A., et al. In vivo targeting of cell death using a synthetic fluorescent molecular probe. *Apoptosis* **16**, 722-731 (2011).
18. Xiong, C., et al. Peptide-based imaging agents targeting phosphatidylserine for the detection of apoptosis. *Journal of medicinal chemistry* **54**, 1825-1835 (2011).
19. Ohnishi, S., et al. Intraoperative detection of cell injury and cell death with an 800 nm near-infrared fluorescent annexin V derivative. *Am J Transplant* **6**, 2321-2331 (2006).
20. Al-Ejeh, F., et al. In vivo targeting of dead tumor cells in a murine tumor model using a monoclonal antibody specific for the La autoantigen. *Clin Cancer Res* **13**, 5519s-5527s (2007).
21. Al-Ejeh, F., et al. APOMAB, a La-specific monoclonal antibody, detects the apoptotic tumor response to life-prolonging and DNA-damaging chemotherapy. *PLoS One* **4**, e4558 (2009).
22. Trepel, J., Mollapour, M., Giaccone, G. & Neckers, L. Targeting the dynamic HSP90

- complex in cancer. *Nat Rev Cancer* **10**, 537-549 (2010).
23. Wandinger, S.K., Richter, K. & Buchner, J. The Hsp90 chaperone machinery. *J. Biol. Chem.* **283**, 18473-18477 (2008).
  24. Lee, C.C., Lin, T.W., Ko, T.P. & Wang, A.H. The hexameric structures of human heat shock protein 90. *PLoS One* **6**, e19961 (2011).
  25. Nardai, G., Sass, B., Eber, J., Orosz, G. & Csermely, P. Reactive cysteines of the 90-kDa heat shock protein, Hsp90. *Arch. Biochem. Biophys.* **384**, 59-67 (2000).
  26. Park, D., *et al.* Noninvasive imaging of cell death using an Hsp90 ligand. *J Am Chem Soc* **133**, 2832-2835 (2011).
  27. Xie, B.W., *et al.* Optical imaging of cell death in traumatic brain injury using a heat shock protein-90 alkylator. *Cell Death Dis* **4**, e473 (2013).
  28. Scarlett, J.L., *et al.* Changes in mitochondrial membrane potential during staurosporine-induced apoptosis in Jurkat cells. *FEBS Lett.* **475**, 267-272 (2000).
  29. Tafani, M., Minchenko, D.A., Serroni, A. & Farber, J.L. Induction of the mitochondrial permeability transition mediates the killing of HeLa cells by staurosporine. *Cancer Res.* **61**, 2459-2466 (2001).
  30. Sauter, B., *et al.* Consequences of cell death: exposure to necrotic tumor cells, but not primary tissue cells or apoptotic cells, induces the maturation of immunostimulatory dendritic cells. *J. Exp. Med.* **191**, 423-434 (2000).
  31. Aslakson, C.J. & Miller, F.R. Selective events in the metastatic process defined by analysis of the sequential dissemination of subpopulations of a mouse mammary tumor. *Cancer Res.* **52**, 1399-1405 (1992).
  32. Hobbs, S.K., *et al.* Regulation of transport pathways in tumor vessels: role of tumor type and microenvironment. *Proceedings of the National Academy of Sciences of the United States of America* **95**, 4607-4612 (1998).
  33. Singh, R.K., *et al.* Organ site-dependent expression of basic fibroblast growth factor in human renal cell carcinoma cells. *The American journal of pathology* **145**, 365-374 (1994).
  34. Kashiwagi, S., *et al.* NO mediates mural cell recruitment and vessel morphogenesis in murine melanomas and tissue-engineered blood vessels. *The Journal of clinical investigation* **115**, 1816-1827 (2005).
  35. Roberts, W.G., *et al.* Host microvasculature influence on tumor vascular morphology and endothelial gene expression. *The American journal of pathology* **153**, 1239-1248 (1998).
  36. Joensuu, H. & Gligorov, J. Adjuvant treatments for triple-negative breast cancers. *Ann. Oncol.* **23 Suppl 6**, vi40-45 (2012).
  37. Yang, T.J., Haimovitz-Friedman, A. & Verheij, M. Anticancer therapy and apoptosis imaging. *Experimental oncology* **34**, 269-276 (2012).
  38. Taylor, R.C., Cullen, S.P. & Martin, S.J. Apoptosis: controlled demolition at the cellular level. *Nat Rev Mol Cell Biol* **9**, 231-241 (2008).
  39. Porter, A.G. & Janicke, R.U. Emerging roles of caspase-3 in apoptosis. *Cell Death Differ.* **6**, 99-104 (1999).
  40. Ayukawa, K., *et al.* La autoantigen is cleaved in the COOH terminus and loses the nuclear localization signal during apoptosis. *J. Biol. Chem.* **275**, 34465-34470 (2000).
  41. Donoghue, N., Yam, P.T., Jiang, X.M. & Hogg, P.J. Presence of closely spaced protein thiols on the surface of mammalian cells. *Protein Sci* **9**, 2436-2445 (2000).





## **CHAPTER SIX**

### **General Discussion and Future Scope**



## 6.1 General Discussion

Optical imaging, both at microscopic and macroscopic level, is developing rapidly and spanning research in all current life sciences. It has been not only employed to study specific promoters, protein-protein interaction and gene transfer at molecular level, but also to follow the fate of GFP, RFP and/or luciferase expressing cells and detect NIR fluorescent probes at whole body scale<sup>1-4</sup>.

At microscopic level, optical imaging benefits from the ongoing development of *in vivo* microscopic technologies. Optical imaging by confocal and multi-photon microscopy can provide images with the highest sensitivity and spatial resolution. Although the limited light penetration depth through biological tissue restrains its diagnostic and therapeutic applications in humans, current development of new tunable lasers in the mid- and far-infrared range will substantially increase the tissue penetration depth. Optical imaging has in this respect the potential to deliver high-resolution, histology-type reconstruction of tumor and tumor microenvironment in the living organism<sup>2,5-8</sup>. Compared to other molecular modalities, optical imaging and optical reporter systems are very cost-effective and time-efficient, so that they are particularly well suited for *in vitro* assays, e.g. to validate different reporter systems.

At macroscopic level, the development of specific injectable NIR fluorescent probes enables the non-invasive and real-time whole body imaging of animal models, offering the potential to translate optical imaging into clinical applications<sup>9</sup>. Particularly, in cancer research, future applications should allow quantitative measurements of tumor progression and micro-metastasis and treatment response<sup>10</sup>. Due to its high sensitivity, optical imaging is extremely useful for early detection of micro-metastases and minimal residual disease states in animal models<sup>11,12</sup>.

However, in term of cancer research, the major challenge of non-invasive optical imaging of cancer is to enhance tumor-to-background ratio (TBR). As described in this thesis, various injectable optical imaging agents, which are specific for detecting hallmarks of cancer, have been developed. These imaging agents in general provide a better TBR compared to the non-specific agents like indocyanine green (ICG), although ICG is the only FDA-approved cyanine dye as an optical imaging agent for medical diagnostics<sup>13,14</sup>. Even though there are already a variety of injectable optical imaging agents becoming available, the current state-of-art *in vivo* optical imaging is still a preclinical research tool. This is mainly because of limitations in penetration depth and light scattering, which consequently lowers the resolution of the image. More efforts should be addressed to make optical imaging agents that yield high local concentrations in deep tumor tissues but have minimal light scattering, minimum non-specific tissue extravasation, internalization by macrophages and rapid renal or hepatic removal. Considering these factors, a broad range of chemical or biological amplification strategies are emerging: 1) Using multivalency to label a single molecule with multiple fluorophores; 2) Using the quenching effect by pairing fluorochromes with

---

quenchers or via distance-dependent interaction between excited states of dyes (FRET); 3) Using covalent reaction to bind targets (activity-based binding); 4) Using photolysis (uncaging) by releasing caged compounds; 5) Using biological processes like enzyme activation, cellular trapping or pre-targeting molecular agents first by a multivalent agent and then by a fluorescent conjugate <sup>15-19</sup>.

Over the last decades, cell death has been considered to be a natural barrier to cancer development. Triggered by anticancer therapy or by various types of physiological stress during tumorigenesis, cancer cells are forced to follow apoptosis and/or necrosis <sup>13,14,20</sup>. However, others elucidated that cancer cells can resist therapy by evolving diverse strategies to circumvent or dampen apoptosis. Compelling functional studies supporting this include: apoptosis could be eliminated by abolishing TP53 tumor suppressor function, or by elevating the expression level of anti-apoptotic regulators (e.g. Bcl-2), or alternatively, by downregulating pro-apoptotic factors (e.g. Bax and Bak) <sup>18,21,22</sup>. Moreover, cell proliferative and apoptotic pathways are often coupled, as many promoters of cell proliferation have been found to also possess pro-apoptotic activity <sup>23</sup>. Thus, the resistance of cell death has been widely accepted as one of the major hallmarks of cancer.

Perhaps more importantly, recent study revealed that another major type of cell death, necrosis, has pro-inflammatory and tumor-promoting potential <sup>24</sup>. As compared to other types of cell death (e.g. apoptosis and autophagy), necrosis can release pro-inflammatory signals into the tumor surrounding tissue and recruit immune inflammatory cells to promote tumor angiogenesis, cancer cell proliferation and invasiveness <sup>21,25,26</sup>. In certain circumstances, cancer cells can undergo programmed necrosis (necroptosis) to release bioactive regulatory factors to stimulate neighboring viable cancer cells to proliferate so that incipient neoplasias can be sustained and facilitated <sup>21,27</sup>. By tolerating certain amount of necrosis, e.g. spontaneously forming a necrotic core during tumor development, aggressive cancer cells can benefit from attracting tumor-promoting inflammatory cells. These cells can then foster growth-stimulating factors to the surviving cells and eventually promote neoplastic progression <sup>25,28</sup>.

Besides the complicated relation between tumor progression and cell death, a rich amount of cell death imaging agents has been developed to imaging tumor cell death, in order to follow the efficacy of anti-tumor therapies. As described earlier in the thesis introduction, most of these cell death imaging agents are either reacting with intracellular biomarkers, like cytosolic proteins, caspase enzymes, exposed DNA and mitochondrial membrane electronic potential, or targeting extracellular biomarkers, like plasma membrane phospholipids. In this thesis, we mainly analyzed two representative cell death optical imaging agent, PSS-794 (targeting the extracellular biomarker phosphatidylserine) and GSAO-AF750 (targeting the intracellular biomarker HSP-90 in cells which have lost membrane integrity). At the end of this chapter, a list has been made to summarize the pros and cons of current available tumor cell death imaging agent (Table 1).

## 6.2 Future Scope

In order to address important needs in clinical translation, new high resolution and deep penetration optical (or multimodal) imaging technologies are required. Simultaneous and combined readouts need to be acquired in order to couple relevant functional information to anatomical and spatial information. For this, optical imaging and SPECT/PET will be thrust together with MRI and/or CT. The advantage of multimodal imaging modality will enable to monitor a wide range of functional parameters especially in relation to molecular events with high sensitivity, great temporal and spatial resolution as well as deep tissue penetration. But the limitation of conventional optical imaging is that the analysis has only been based on two-dimensional planar images and that spatial resolution is relatively poor. To address this problem, optical imaging is now extended to three-dimensional (3D) imaging with volumetric information, e.g. by fluorescence-mediated molecular tomography (FMT) and multispectral optoacoustic tomography (MSOT)<sup>29,30</sup>. These new 3D optical imaging modalities will allow visualization of deeper inside tumor tissues compared to conventional optical imaging<sup>31</sup>. Current preclinical instruments limit optical imaging depth to 2-3 cm and resolutions of 1-2 mm. This would explain why optical *in vivo* imaging has remained mostly in the preclinical research arena. MSOT, for example, could be the promising next generation for cancer imaging, representing a paradigm shift for optical imaging, with resolutions in the 20-200  $\mu\text{m}$  range and with penetration depths of several centimeters<sup>30,32</sup>. Moreover, multimodality imaging, in which optical technologies are combined with clinical technologies, will be an important and promising non-invasive approach to acquire structural and anatomical information<sup>33-35</sup>. The ongoing efforts will greatly facilitate the translation of multimodal molecular imaging into the clinic. The first new clinical application of optical imaging will be in image-guided surgery to visualize tumor tissue or to find sentinel lymph node. This will be done either during open surgery where tumor tissue is near the surface or during minimal invasive laparoscopic or endoscopic surgery. For this purpose, new sensitive NIRF camera systems have been developed<sup>36</sup>.

Until now, only indocyanine green (ICG) has been used as a non-targeted probe, since it is the only FDA approved probe. The NIRF dye ICG has mostly been used to find sentinel lymph nodes but also to detect liver metastasis of colon cancer. In the later case, one takes the advantage that ICG, which strongly binds to serum albumin, leaks into the tumor tissue based on the EPR effect and retains as a ring around the tumor margin, mainly due to lack of proper clearance<sup>37</sup>. Such translation will be important for the clinic in providing sensitive, specific, and real-time intra-operative visualization of the molecular features of physiological and pathological processes<sup>4,38-40</sup>.

All in all, compared to other imaging modalities, optical imaging offers superior sensitivity (e.g. single molecular level), great temporal resolution (e.g. picoseconds) as well as reasonable spatial resolution (1-2 millimeter)<sup>19,41</sup>. Thanks to these advantages, optical imaging can broaden its way for other clinical applications.

Cell death imaging agent	Mechanism of action	Animal Model	Treat-ment	Imaging Modality
<b>PSS-794</b> Zinc(II)-dipicolylamine	Binds to multianionic phosphorylated biomolecules, including the binding of PS at the outer surfaces of anionic vesicles and cell membranes	Subcutaneous PAIII prostate adenocarcinoma in rats and EMT6 mammary tumours in mice	None	FLI
		Subcutaneous PAIII prostate adenocarcinoma in rats	Radiation	
<b>GSAO</b> 4-(N-(S-glutathionylacetyl) amino) phenylarsenoxide	Binds cytoplasmic Hsp90 following loss of plasma membrane integrity	Orthotopic human 4T1 breast tumour in mice	Cyclophosphamide	FLI
		Subcutaneous mouse Lewis lung carcinoma and human CT26 colorectal carcinoma in mice	None	SPECT
<b>Fluorescent annexin V</b> (Annexin V–Cy5.5)	Binds to extracellular-facing PS due to its externalization at the early stage of apoptosis	Lewis lung Carcinoma (LLC) in chemosensitive and chemoresistant mice	Cyclophosphamide	FLI
<b>Radiolabeled annexin-V</b> ( <sup>99m</sup> Tc-Annexin V)		Human breast cancer MDA-MB435 cells in athymic mice	Anti-CD95, quercetin, Siamois 1 and Siamois 2	SPECT
<b>SPIO-C2A</b> C2A domain of Synaptotagmin I	Binds to negatively charged phospholipids including PS, which redistributed from inner to the outer leaflet of plasma membrane during cell death	Subcutaneous EL4 lymphoma in mice	combination of cyclophosphamide and etoposide	MRI
<sup>99m</sup> <b>Tc-C2A</b> C2A domain of Synaptotagmin I		Subcutaneous human H460 non-small cell lung cancer in mice	Paclitaxel	SPECT
<b><sup>18</sup>F-ICMT-11</b>	Binds to activated caspases 3 and 7	Subcutaneous 38C13 lymphoma xenograft in mice	Cyclophosphamide	PET
<b><sup>111</sup>In-3B9</b> (APOMAB)	Binds to the La ribonucleoprotein upon loss of plasma membrane integrity	Subcutaneous EL4 murine lymphoma in mice	Combination cyclophosphamide and etoposide	SPECT
<b><sup>111</sup>In-DAB4</b> (APOMAB)		Subcutaneous EL4 murine lymphoma in mice		

Table 1. Summary of current tumor cell death imaging studies.

Pros	Cons	Ref
<p>1. Small molecular (&lt;2KDa) with the same targeting capability as Annexin V;</p> <p>2. Lower renal uptake compared to that of Annexin V;</p> <p>3. Formulated as a zinc complex improves water solubility.</p>	<p>1. Binding to the phosphatidylserine (PS) exposed on dying cells is zinc-dependent;</p> <p>2. Accumulation at the target limited by the surface area of the plasma membrane and the abundance of externalised of PS;</p> <p>3. Can exhibit cross reactivity for PS in activated platelets, macrophages, endothelial cells and aging erythrocytes;</p> <p>4. Can also bind reversible PS in situations of physiological stress;</p> <p>5. Also selectively target bacteria in heterogeneous biological media;</p> <p>6. Cannot discriminate apoptotic and necrotic tissues.</p>	42
		43
<p>1. High stability, easy synthesis and versatility with respect to reporter group;</p> <p>2. Small size (0.5kDa) contributes to fast clearance and favourable biodistribution;</p> <p>3. Abundance of cytoplasmic target lends to high signal to noise ratio.</p>	<p>1. High renal uptake precludes imaging of kidney and adjacent structures;</p> <p>2. Is unsuitable for discrimination between apoptosis and necrosis.</p>	Chapter5
		44
<p>1. Strong affinity to PS;</p> <p>2. Ligand readily available on cell surface;</p> <p>3. Radiolabeled annexin-V has already been studied in humans with acceptable radiation burden.</p>	<p>1. Large size (&gt;35KDa) results in slow delivery to site of interest, slow clearance, non-specific uptake in non-target tissues and especially strong renal uptake;</p> <p>2. Binding to the PS exposed on dying cells is calcium-dependent;</p> <p>3. As above PSS-794 point 2,3 and 4.</p>	45
		46
<p>1. Small size (&lt;15KDa) so that good penetration of tumor tissue;</p> <p>2. Quick clearance of unbound material so that good tissue contrast;</p> <p>3. Ligand readily available on cell surface.</p>	<p>1. Low affinity to PS (dissociation constant between 90-300 nM. compared to 1-2 nM for Annexin V) due to the imaging agent is a heterogeneous mixture of labelled molecules;</p> <p>2. High renal and hepatic uptake precluding imaging of abdominal region;</p> <p>3. Binding to the PS exposed on dying cells is calcium-dependent.</p>	47
		48
<p>Early detection of caspase-3/7 associated tumor apoptosis.</p>	<p>1. High hepatic uptake precludes imaging of abdominal region;</p> <p>2. Possible cross-reactivity with cathepsins;</p> <p>3. Not suitable to detect necrosis.</p>	49
<p>1. Detection of cell death specific for both tumour cells and other cells, which apoptosis was induced by DNA damaging agents;</p> <p>2. Chemo-sensitive tissue such as gut and bone marrow do not complicate image.</p>	<p>Detection limited to apoptotic malignant cells in response to DNA-damaging treatment.</p>	50
		51

---

## References

1. Plathow, C. & Weber, W.A. Tumor cell metabolism imaging. *J Nucl Med* **49 Suppl 2**, 43S-63S (2008).
2. Levenson, R.M., Lynch, D.T., Kobayashi, H., Backer, J.M. & Backer, M.V. Multiplexing with multispectral imaging: from mice to microscopy. *ILAR J* **49**, 78-88 (2008).
3. Petibois, C. Imaging methods for elemental, chemical, molecular, and morphological analyses of single cells. *Anal Bioanal Chem* (2010).
4. Lowik, C.W., et al. Whole body optical imaging in small animals and its translation to the clinic: intra-operative optical imaging guided surgery. *Eur J Cancer* **45 Suppl 1**, 391-393 (2009).
5. Corsten, M.F. & Bennaghmouch, A. Optical characterization of arterial apoptosis. *Methods Mol Biol* **680**, 117-129 (2010).
6. Ghoroghchian, P.P., Therien, M.J. & Hammer, D.A. In vivo fluorescence imaging: a personal perspective. *Wiley Interdiscip Rev Nanomed Nanobiotechnol* **1**, 156-167 (2009).
7. Pittet, M.J. & Weissleder, R. Intravital imaging. *Cell* **147**, 983-991 (2011).
8. Thurber, G.M., Figueiredo, J.L. & Weissleder, R. Multicolor fluorescent intravital live microscopy (FILM) for surgical tumor resection in a mouse xenograft model. *PLoS One* **4**, e8053 (2009).
9. Rao, J., Dragulescu-Andrasi, A. & Yao, H. Fluorescence imaging in vivo: recent advances. *Curr Opin Biotechnol* **18**, 17-25 (2007).
10. Mahmood, U. & Weissleder, R. Near-infrared optical imaging of proteases in cancer. *Mol Cancer Ther* **2**, 489-496 (2003).
11. Ignat, M., et al. Feasibility and Reliability of Pancreatic Cancer Staging Using Fiberoptic Confocal Fluorescence Microscopy in Rats. *Gastroenterology* (2009).
12. Kim, J.B., et al. Non-invasive detection of a small number of bioluminescent cancer cells in vivo. *PLoS One* **5**, e9364 (2010).
13. Lowe, S.W., Cepero, E. & Evan, G. Intrinsic tumour suppression. *Nature* **432**, 307-315 (2004).
14. Bertram, J.S. The molecular biology of cancer. *Mol Aspects Med* **21**, 167-223 (2000).
15. Joseph, J., Seervi, M., Sobhan, P.K. & Retnabai, S.T. High throughput ratio imaging to profile caspase activity: potential application in multiparameter high content apoptosis analysis and drug screening. *PLoS One* **6**, e20114 (2011).
16. Blum, G., von Degenfeld, G., Merchant, M.J., Blau, H.M. & Bogoy, M. Noninvasive optical imaging of cysteine protease activity using fluorescently quenched activity-based probes. *Nat Chem Biol* **3**, 668-677 (2007).
17. Maxwell, D., Chang, Q., Zhang, X., Barnett, E.M. & Piwnica-Worms, D. An improved cell-penetrating, caspase-activatable, near-infrared fluorescent peptide for apoptosis imaging. *Bioconjug Chem* **20**, 702-709 (2009).
18. Adams, J.M. & Cory, S. The Bcl-2 apoptotic switch in cancer development and therapy. *Oncogene* **26**, 1324-1337 (2007).
19. Muller, J., Wunder, A. & Licha, K. Optical imaging. *Recent Results Cancer Res* **187**, 221-246 (2013).
20. Evan, G.I. & Vousden, K.H. Proliferation, cell cycle and apoptosis in cancer. *Nature* **411**, 342-348 (2001).
21. Muller, P.A. & Vousden, K.H. p53 mutations in cancer. *Nat Cell Biol* **15**, 2-8 (2013).
22. Zhao, L., Guo, Q.L., You, Q.D., Wu, Z.Q. & Gu, H.Y. Gambogic acid induces apoptosis and regulates expressions of Bax and Bcl-2 protein in human gastric carcinoma MGC-803 cells. *Biol Pharm Bull* **27**, 998-1003 (2004).
23. Evan, G. & Littlewood, T. A matter of life and cell death. *Science* **281**, 1317-1322 (1998).
24. Czernin, J., Weber, W.A. & Herschman, H.R. Molecular imaging in the development of cancer therapeutics. *Annu Rev Med* **57**, 99-118 (2006).
25. Grivennikov, S.I., Greten, F.R. & Karin, M. Immunity, inflammation, and cancer. *Cell* **140**, 883-899 (2010).
26. Mathew, R. & White, E. Autophagy in tumorigenesis and energy metabolism: friend by day, foe by night. *Current opinion in genetics & development* **21**, 113-119 (2011).
27. Han, J., Zhong, C.Q. & Zhang, D.W. Programmed necrosis: backup to and competitor with apoptosis in the immune

- system. *Nature immunology* **12**, 1143-1149 (2011).
28. Zong, W.X. & Thompson, C.B. Necrotic death as a cell fate. *Genes Dev* **20**, 1-15 (2006).
29. Ntziachristos, V., Bremer, C., Graves, E.E., Ripoll, J. & Weissleder, R. In vivo tomographic imaging of near-infrared fluorescent probes. *Mol Imaging* **1**, 82-88 (2002).
30. Razansky, D., Buehler, A. & Ntziachristos, V. Volumetric real-time multispectral optoacoustic tomography of biomarkers. *Nat Protoc* **6**, 1121-1129 (2011).
31. Hilderbrand, S.A. & Weissleder, R. Near-infrared fluorescence: application to in vivo molecular imaging. *Curr Opin Chem Biol* **14**, 71-79 (2010).
32. Ntziachristos, V. & Razansky, D. Molecular imaging by means of multispectral optoacoustic tomography (MSOT). *Chem Rev* **110**, 2783-2794 (2010).
33. Kaijzel, E.L., Snoeks, T.J., Buijs, J.T., van der Pluijm, G. & Lowik, C.W. Multimodal imaging and treatment of bone metastasis. *Clin Exp Metastasis* **26**, 371-379 (2009).
34. Niers, J.M., Kerami, M., Pike, L., Lewandrowski, G. & Tannous, B.A. Multimodal in vivo imaging and blood monitoring of intrinsic and extrinsic apoptosis. *Mol Ther* **19**, 1090-1096 (2011).
35. Radermacher, K.A., et al. Multimodal assessment of early tumor response to chemotherapy: comparison between diffusion-weighted MRI, <sup>1</sup>H-MR spectroscopy of choline and USPIO particles targeted at cell death. *NMR Biomed* **25**, 514-522 (2012).
36. Keereweer, S., et al. Optical Image-guided Surgery-Where Do We Stand? *Mol Imaging Biol* (2010).
37. Schaafsma, B.E., et al. The clinical use of indocyanine green as a near-infrared fluorescent contrast agent for image-guided oncologic surgery. *J Surg Oncol* **104**, 323-332 (2011).
38. Jaffer, F.A. & Weissleder, R. Molecular imaging in the clinical arena. *JAMA* **293**, 855-862 (2005).
39. Frangioni, J.V. New technologies for human cancer imaging. *J Clin Oncol* **26**, 4012-4021 (2008).
40. Leblond, F., Davis, S.C., Valdes, P.A. & Pogue, B.W. Pre-clinical whole-body fluorescence imaging: Review of instruments, methods and applications. *J Photochem Photobiol B* **98**, 77-94 (2010).
41. Luke, G.P., Yeager, D. & Emelianov, S.Y. Biomedical applications of photoacoustic imaging with exogenous contrast agents. *Ann Biomed Eng* **40**, 422-437 (2011).
42. Smith, B.A., et al. Optical imaging of mammary and prostate tumors in living animals using a synthetic near infrared zinc(II)-dipicolylamine probe for anionic cell surfaces. *J Am Chem Soc* **132**, 67-69 (2010).
43. Smith, B.A., et al. In vivo targeting of cell death using a synthetic fluorescent molecular probe. *Apoptosis* **16**, 722-731 (2011).
44. Park, D., et al. Noninvasive imaging of cell death using an Hsp90 ligand. *J Am Chem Soc* **133**, 2832-2835 (2011).
45. Schellenberger, E.A., et al. Optical imaging of apoptosis as a biomarker of tumor response to chemotherapy. *Neoplasia* **5**, 187-192 (2003).
46. Al-Ejeh, F., et al. In vivo targeting of dead tumor cells in a murine tumor model using a monoclonal antibody specific for the La autoantigen. *Clin Cancer Res* **13**, 5519s-5527s (2007).
47. van Tilborg, G.A., et al. Annexin A5-functionalized bimodal nanoparticles for MRI and fluorescence imaging of atherosclerotic plaques. *Bioconjug Chem* **21**, 1794-1803 (2010).
48. Dechsupa, S., et al. Quercetin, Siamois 1 and Siamois 2 induce apoptosis in human breast cancer MDA-mB-435 cells xenograft in vivo. *Cancer Biol Ther* **6**, 56-61 (2007).
49. Ohnishi, S., et al. Intraoperative detection of cell injury and cell death with an 800 nm near-infrared fluorescent annexin V derivative. *Am J Transplant* **6**, 2321-2331 (2006).
50. Xiong, C., et al. Peptide-based imaging agents targeting phosphatidylserine for the detection of apoptosis. *Journal of medicinal chemistry* **54**, 1825-1835 (2011).
51. Al-Ejeh, F., et al. APOMAB, a La-specific monoclonal antibody, detects the apoptotic tumor response to life- prolonging and DNA-damaging chemotherapy. *PLoS One* **4**, e4558 (2009).





## CHAPTER SEVEN

**Summary**  
- 论文摘要 -  
**Samenvatting**



## Summary

Optical imaging has shown its appeal as a sensitive, cost-effective and time-efficient preclinical research technique for both *in vitro* assays and *in vivo* whole body imaging. Especially, the development of injectable tumor-specific near-infrared fluorescent (NIRF) probes has made fluorescence imaging (FLI) an effective tool for real-time detection of tumors and metastases in various experimental models. These NIRF probes also have the potential to be used clinically.

In this thesis, we explored diverse applications of using NIRF probes, with specific properties, to visualize and characterize the development of cancer and cell death. In **Chapter 2**, we addressed the questions whether it is possible to detect tumor progression in a luciferase-expressing 4T1-luc2 mouse breast cancer model by using combinations of activatable and targeting NIRF probes; and if there is a correlation between FLI and bioluminescence imaging (BLI) measurements. To answer these questions, sensitivity and specificity studies were performed. Also, a correlation study between the tumor FLI and BLI signals was carried out. In addition, we explored the possibilities to simultaneously detect multiple tumor characteristics by dual-wavelength FLI (~700 and ~800 nm) combined with spectral unmixing.

*In vitro*, we showed that the activatable NIRF probes (ProSense680 and MMPsense680) and the targeting NIRF probes (IRDye 800CW 2-DG and IRDye 800CW EGF) were either activated by or bound to 4T1-luc2 cells. In our bioluminescent mouse breast cancer model, we orthotopically implanted 4T1-luc2 cells in nude mice. This enables us to follow tumor progression longitudinally both by BLI and dual-wavelength FLI, when using combinations of NIRF probes. An enhanced tumor-to-background ratio and a strong positive linear correlation between FLI and BLI measurements were observed for all probes tested. Moreover, immunohistology on sections revealed that each probe exhibited a specific tissue distribution pattern. For this, the *in vivo* use of probe combinations might provide a more comprehensive image of tumor characteristics. These studies suggest that dual-wavelength FLI is a feasible approach to simultaneously detect different features of one tumor and to follow tumor progression *in vivo*. This approach opens up new perspectives for the detection of tumors and metastases in various experimental models and could also be translated into the clinic, for example, image-guided surgery.

Different tumors are characterized by the expression of specific cell surface- or intracellular markers or by the expression of particular marker profiles. These biomarkers can be used to localize and identify tumors or as target of anti-tumor therapy. This implies that the identification and treatment of different tumor types requires specific probes or sets of probes and treatments. However, apart

---

from these heterogeneities, most types of cancer, especially those aggressive and fast growing ones, always display a common feature, namely cell death. Cell death and in particular necrosis at the tumor center is believed to be the result of chronic ischemia caused by vascular collapse. This occurs when the rate of tumor cell growth exceeds that of angiogenesis, which is associated with poor prognosis. In order to locate and/or treat tumors, these necrotic areas, present in most tumor types, can be used for optical imaging of cancer as a universal target.

To this end, we analyzed two representative cell death NIRF probes, targeting either an extracellular or an intracellular biomarker, in a cryolesion mouse model of traumatic brain injury. Synthetic zinc(II)-dipicolylamine PSS-794 binds to phosphatidylserine that is expressed on the plasma membrane of early and late apoptotic as well as necrotic cells (**Chapter 3**); and fluorescently labelled 4-(N-(S-glutathionylacetyl) amino) phenylarsonous acid (GSAO-AF750) binds to the cytosolic heat shock protein-90 (HSP-90) of apoptotic and necrotic cells, coincident with loss of plasma membrane integrity (**Chapter 4**).

In our cryolesion model, an area of local tissue death is initiated by shortly applying a liquid N<sub>2</sub> pre-cooled metal cylinder to the parietal region of a mouse head. Studies with PSS-794 and GSAO-AF750 showed that both NIRF probes selectively accumulate in the brain cryolesion. Local cell death and probe accumulation was confirmed with histology. Moreover, we developed a new *in vitro* dry-ice cell death assay. Luciferase-expressing 4T1-luc2 cells were grown to confluence in a culture plate. A focal area of cell death was induced in the center of the culture well by applying a bar of dry ice to the underside of the culture plate. Subsequently, cells were incubated with different cell death targeting NIRF probes, washed and subjected to FLI and BLI measurements. The presence of dead cells in the center was confirmed by FLI signals and living (luciferase active) cells in the periphery area were revealed by BLI signals. This rapid and robust assay can be used to screen fluorescently labelled compounds with potential cell death targeting properties. Combined, these data suggested the strong specificity of the two NIRF probes in detecting cell death both *in vitro* and *in vivo*.

Next, we investigated the potential of using a HSP-90 alkylator GSAO-AF750 to non-invasively detect cell death as a biomarker of tumor response to chemotherapy (**Chapter 5**). Because the HSP-90 chaperone is an important element in oncogene addiction and tumor cell survival, its expression is enhanced by chemotherapy. As a fluorescently labelled HSP-90 alkylator, GSAO-AF750 demonstrates a favorable biodistribution. It is cleared quickly from the circulation via kidneys and does not accumulate in healthy organs or tissues. In this study, the cell death targeting property of GSAO-AF750 was examined *in vitro* by flow cytometry using Jurkat T cells treated with staurosporine. In our murine mammary tumor model, we non-invasively imaged cyclophosphamide-induced cell death using GSAO-AF750, which further validated its targeting specificity in

labelling apoptotic and necrotic tissues in solid tumors in mice. Thus, this study offers a novel strategy for dynamic monitoring of tumor treatment outcome. Furthermore, optical imaging of cell death, in general, could be clinically applied to diagnose certain disease where cell death is involved at an early stage, monitor therapeutic efficacy to anti-tumor strategies, or evaluate drug toxicity.

**Chapter 6** gives a general discussion about the optical imaging, both at microscopic and macroscopic level. For the future perspective, this chapter outlooks the possibility to embrace new optical (or multimodal) imaging technologies to address important needs in clinical translation. In terms of imaging cancer and cell death, the current challenges and emerging strategies are highlighted. Moreover, the pros and cons of various available tumor cell death imaging agents are discussed.

Taken together, the preclinical studies in this thesis showed that non-invasive optical imaging of cancer and cell death is of great significance and can satisfy an unmet need for complimentary information that would support other diagnostic imaging modalities such as MRI, SPECT/PET and CT. It could also be a fast and low-cost alternative in cases where the other diagnostic imaging modalities cannot be utilized. For this to happen, *in vivo* optical imaging needs to undergo another step in terms of refining its imaging modality.

---

## 论文摘要

光学成像作为一个敏感的临床前研究技术，具有成本和时间效益的优势，已经显示出其在体外实验和体内全身成像的应用价值。特别是，可注射的具有肿瘤特异性的近红外荧光(NIRF)探针的发展已使荧光成像(FLI)成为各种实验模型中实时检测肿瘤及其转移的有效工具。这些NIRF探针也有应用于临床的可能性。

在此论文中，我们探索了使用具有特定属性的NIRF探针将癌症的发展和细胞死亡可视化并进行特性分析。在第二章中，我们讨论了是否有可能通过使用可激活的和目标靶定的NIRF探针组合来检测有荧光素酶表达的4T1-luc2小鼠乳腺癌的发展。如果此方法可行，我们希望揭示出FLI和生物发光成像(BLI)之间存在的相关性程度。要回答这些问题，我们首先进行了敏感性和特异性的研究。然后，我们进行了肿瘤FLI和BLI信号的相关性研究。此外，我们探索了使用双波长FLI(~700和~800纳米)结合光谱分离同时检测多种肿瘤特性的可能性。

在体外实验中，我们发现可激活的NIRF探针 (ProSense680 和 MMPsense680) 和目标靶定的 NIRF 探针 (IRDye800CW 2-DG 和 IRDye 800CW EGF)能被相应的酶激活或被绑定到4T1-luc2细胞上。在生物发光小鼠乳腺癌模型实验中，我们在裸鼠上腹原位移植了4T1-luc2细胞。这使我们能够用BLI和双波长FLI对肿瘤的发展进行实时跟踪。实验表明，所有被检测的探针都呈现出了增强的肿瘤对背景比，FLI也和BLI有较强的正的线性关系。此外，免疫组化结果显示，每个探针都具有其特定的组织分布格局。正因如此，在体内使用探针组合便可提供一个比较全面的图像肿瘤特性。这些研究表明，双波长FLI是一种可行的方法，此方法能同时检测一个肿瘤的不同特性，并实时跟踪肿瘤在体内的发展。该方法为在各种实验模型中非侵入性的检测肿瘤发生和转移提供了新的视角；也为临床应用转化，例如图像引导的手术，提供了未来实践的可能。

不同的肿瘤的特性由特定的细胞表面或细胞内标记物的表达，或特定标记的整体表达轮廓来界定。这些生物标志物可用于寻找

和识别肿瘤，或作为抗肿瘤治疗的目标。这意味着，不同的肿瘤类型的识别需要使用具有不同特异性的探针，其治疗也需要采用不同的探针和治疗方法的结合。然而，除了这些非均质性，大多数类型的癌症，特别是那些快速增长的恶性肿瘤，总是显示一个共同的特点，即细胞死亡。细胞死亡，尤其是细胞坏死在肿瘤的中心，被认为是由血管性虚脱而导致慢性缺血引起的结果。出现这种情况时，肿瘤细胞的生长速度超过了血管生成，这是与不良预后相关。为了定位和/或治疗肿瘤，这些存在于大多数类型的肿瘤的坏死区域，可作为一个具有广泛适用性的生物标志物加以应用于光肿瘤学成像。

为此，我们采用了创伤性脑损伤的一个冷冻创口小鼠模型来分析两个有代表性的细胞死亡NIRF探针：标记细胞外或标记细胞内的生物标志物。一个是合成的氧化锌(II)-吡啶甲基胺(PSS-794)，它可结合到表达于早期和晚期凋亡和坏死细胞的质膜表面的磷脂酰丝氨酸（第三章）；另一个是荧光标记的4-(N-(S-glutathionylacetyl)amino)phenylarsonous acid (GSAO-AF750)，它可在凋亡和坏死细胞的质膜完整性受损后结合到胞质热休克蛋-90(HSP-90)（第四章）。

在我们用于测试探针的冷冻创口小鼠模型中，我们将一个用液氮预冷后的金属圆尖筒置于小鼠头的顶区，以形成一个局部的组织死亡。实验表明，PSS-794和GSAO-AF750两个NIRF探针在静脉注射到小鼠体内后都选择性地积聚在大脑中的冷冻创口区域。组织学研究证实细胞死亡的区域和探针的积累处相吻合。此外，我们研发出了一个新的干冰细胞死亡体外测试方法。首先，具有荧光素酶表达的4T1-luc2细胞在培养板中生长至饱和。然后，将干冰应用到培养板的底面，以在培养板各孔的中心形成一个细胞死亡的区域。随后，往各孔中添加不同的细胞死亡NIRF探针与细胞进行共同培养，一定培养时间后洗涤并进行FLI和BLI的测量。BLI表达出的信号揭示了有荧光素酶活性的活细胞在外围区域，而由FLI表达出的信号则证实了中心死细胞的存在。此法可用于快速，可靠的筛选具有潜在细胞死亡标记属性的荧光标记化合物。综上所述，这些研究表明，两个被检测的NIRF探针无论在体外还是在体内都表现出了很好的标记细胞死亡的特异性。

---

接着，我们进一步研究了使用HSP-90的烷化剂GSAO-AF750作为非侵入性地检测肿瘤对化疗的反应中细胞死亡这一生物标志物（第五章）。因为HSP-90这一伴侣蛋白是原癌基因成癌和肿瘤细胞生存的重要元素，化疗后它的表达增强。作为荧光标记的HSP-90烷化剂，GSAO-AF750表现出了良好的体内组织分布。这表现在它很快地通过肾脏的循环被清除，不会积聚在健康的器官或组织。在这项研究中，GSAO-AF750在离体的细胞死亡靶向性是通过流式细胞仪来检测的，所使用的细胞是用十字孢碱处理过的Jurkat T细胞。在活体实验中，我们再次采用了小鼠乳腺肿瘤模型，通过使用GSAO-AF750，我们非侵入性地成像出了环磷酰胺诱导的细胞死亡，这进一步验证了其靶向特异性地标记小鼠固体肿瘤内的细胞凋亡和坏死组织。因此，这项研究提供了一种对肿瘤治疗效果进行动态监测的新策略。此外，推而广之，光学成像细胞死亡还可以在临床的其他领域广为应用：比如某些早期阶段涉及细胞死亡的疾病的诊断，监测抗肿瘤药的治疗功效，或者是对药物毒性的评价。

第六章给出了对光学成像在宏观和微观层面上的一般性讨论。对于未来发展的前景，此章展望了以融入新的光学成像技术（或多种成像技术结合）来解决临床转化的燃眉之需的可能性。对成像癌症和细胞死亡而言，此章列举了当前的挑战和新兴的战略对策。此外，现有的各种肿瘤细胞死亡显像剂的利弊在此章也进行了讨论。

综上所述，此论文中的临床前研究表明，对癌症和细胞死亡进行非侵入性的光学成像具有十分重要的意义；这些研究能满足现有的需求并为其他诊断成像方式，如MRI,SPECT/PET和CT提供互补支持。它也可能在其它诊断成像方式不能被利用的情况下作为一个快速而又物美价廉的替代方式。为了做到这一点，活体光学成像还需要进一步精进其成像的技术模式。

## Samenvatting

Optische beeldverwerking is een gevoelige, snelle en relatief goedkope techniek toepasbaar in preklinisch *in vitro* en *in vivo* onderzoek. De ontwikkeling van injecteerbare nabij infrarode fluorescente (NIRF) probes heeft fluorescente beeldverwerking geschikt gemaakt om tumorgroei en metastasering in de tijd te volgen in proefdieren. Deze NIRF probes kunnen wellicht op den duur ook bij patiënten worden gebruikt.

In dit proefschrift wordt de toepasbaarheid van verschillende NIRF probes beschreven om tumorgroei en celdood te visualiseren. In **hoofdstuk 2** wordt een combinatie van enzym activeerbare en specifiekgerichte NIRF probes gebruikt om de tumorgroei te volgen in een 4T1-luc2 borstkankermodel in muizen. De correlatie tussen fluorescentie (FLI) en bioluminescentie (BLI) in dit model wordt beschreven. Verder laat dit hoofdstuk de mogelijkheden zien om simultaan meerdere tumoreigenschappen te visualiseren door gebruik te maken van een combinatie van NIRF probes met verschillende spectrale eigenschappen, die we van elkaar kunnen onderscheiden door spectrale analyse.

*In vitro* experimenten laten zien dat de 4T1-luc2 cellen in staat zijn de enzym activeerbare probes (ProSense680 en MMPSense680) te activeren en de specifiek gerichte probes (IRDye 800CW 2-DG en IRDye 800CW EGF) te binden. Na injectie van deze cellen in het borstweefsel van immuundeficiente muizen is tumorgroei met bioluminescentie te volgen. Als vervolgens de verschillende NIRF probes worden ingespoten zien we een sterke lineaire correlatie tussen BLI en FLI met een goede signaal-ruis verhouding. Immunohistochemie laat probe-specifieke expressiepatronen zien in de tumoren waaruit we kunnen afleiden dat het gebruik van deze probes in het proefdier een meer compleet beeld geeft van de verschillende tumoreigenschappen. Het simultaan kunnen visualiseren van verschillende tumoreigenschappen door gebruik te maken van een mix van verschillende NIRF probes in combinatie met spectrale analyse (unmixing) van de verschillende fluorescentie signalen zou wellicht toepasbaar kunnen worden in klinisch onderzoek, in het bijzonder bij beeldgeleide chirurgie.

Elke tumor heeft zijn eigen karakteristieke kenmerken van intracellulaire en oppervlakte eiwitten welke gebruikt kunnen worden ter identificatie van de tumor of bij het bepalen van de te volgen anti-kanker therapie. Verschillende probes en therapieën zijn dus nodig om de verschillende tumoren te identificeren dan wel te behandelen. Wat de verschillende vooral agressieve tumorsoorten meestal gemeen hebben is de vorming van een necrotische kern als gevolg van celdood door ischemie veroorzaakt door vaatlijden. Dit proces treedt op wanneer de snelheid van de tumorgroei groter is dan de vorming van nieuwe bloedvaten door angiogenese en is geassocieerd met slechte prognose. Celdood in necrotisch weefsel is dus een vrij universeel kenmerk van tumoren en kan

---

gebruikt worden om tumoren te lokaliseren of als doelwit voor behandeling.

In **hoofdstuk 3** en **4** worden experimenten beschreven met twee verschillende NIRF probes die specifiek zijn voor het aantonen van dode cellen. In een experimenteel proefdier model waarin traumatisch hersenletsel wordt veroorzaakt door een cryolesie worden in **hoofdstuk 3** de resultaten van de experimenten beschreven uitgevoerd met het synthetische zink(II)-dipicolylamine PSS-794 dat bindt aan fosfatidylserine dat tot expressie komt op de membranen van (vroeg en laat) apoptotische en necrotische cellen. In **hoofdstuk 4** worden de bevindingen beschreven uitgevoerd met het fluorescent gelabelde 4-(N-(S-glutathionylacetyl) amino) phenylarsonous acid (GSAO-AF750) dat aan het cytosolisch heat shock protein-90 (HSP-90) bindt afkomstig uit apoptotische en necrotische cellen wat samengaat met het lek raken van de plasmamembraan.

In het experimenteel cryolesie model wordt een metalen cilinder, dat gekoeld is door vloeibaar stikstof, kortstondig tegen de schedel van een muis gehouden. Dit veroorzaakt lokaal celdood in de hersenen. De NIRF probes PSS-794 en GSAO-AF750 blijken selectief te accumuleren in de cryolesie in de hersenen. Celdood en specifieke accumulatie van de probe in necrotisch weefsel werd bevestigd met histologie. Voor deze studies hebben we een nieuwe assay ontwikkeld waarin we celdood initiëren in de kweekplaat. Bioluminescente 4T1-luc2 cellen worden gekweekt in de kweekplaat waarna er aan de onderkant van de plaat een pellet droogijs tegenaan wordt gehouden. Dit veroorzaakt lokaal celdood met als gevolg lokale inactivatie van het luciferase enzyme waardoor er geen bioluminescentie signaal optreedt op de behandelde plek. Na toevoeging van de fluorescente NIRF probes zien we specifiek fluorescentie op de plek waar celdood is. Deze snelle en robuuste is dus uitermate geschikt om nieuwe probes te screenen op hun potentie om dode cellen aan te tonen. De verkregen data suggereren dat beide probes in staat zijn specifieke celdood aan te tonen.

In **hoofdstuk 5** laten we zien dat GSAO-AF750 te gebruiken is om de effectiviteit van chemotherapie aan te tonen door zijn capaciteit om celdood te detecteren. De expressie van HSP-90 wordt verhoogd als gevolg van de chemotherapie. Biodistributie studies tonen aan dat de fluorescent gelabelde probe snel wordt geklaard via de nieren en niet accumuleert in gezond weefsel. Flowcytometrie laat specifieke binding van de probe zien aan dode Jurkat T cellen die behandeld zijn met staurosporine. In muizen met een tumor die behandeld worden met cyclophosphamide, bindt de probe aan necrotische en apoptotische tumorcellen. Optische beeldverwerking met behulp van specifieke fluorescente celdood-probes maakt het mogelijk de effectiviteit van tumor therapie in tijd te vervolgen. Mogelijkerwijs is deze strategie in de toekomst ook bij patiënten met kanker toe te passen.

In **hoofdstuk 6** worden mogelijke toekomstperspectieven van optische beeldverwerking zowel op microscopisch als macroscopisch niveau

bediscussieerd. In dit hoofdstuk wordt ook de mogelijkheid besproken hoe nieuwe optische of multi-modale beeldverwerkings technieken toegepast zouden kunnen worden in de kliniek. Wat betreft de beeldverwerking van kanker en celdood worden de huidige uitdagingen en nieuwe strategieën besproken. Tevens wordt er aandacht besteed aan de voor- en nadelen van de vele verschillende celdood probes.

Al met al benadrukken de in dit proefschrift beschreven preklinische studies het belang van non-invasieve optische beeldverwerking van tumorgroei en celdood. Deze techniek is zeer waardevol en biedt complementaire informatie naast de gebruikelijke diagnostiek verkregen met behulp van MRI, SPECT/PET en CT. Een ander bijkomend voordeel van deze snelle diagnostische methode zijn de lage kosten in vergelijking met de andere modaliteiten. Echter, voordat optische beeldverwerking zich een vaste plaats kan verwerven in de diagnostiek naast de bestaande technieken zal er nog het nodige gedaan moeten worden aan de verdere optimalisatie van deze techniek.





## **CHAPTER EIGHT**

### **Miscellaneous**



## Acknowledgements – 致谢 – Dankwoord

A past lecturer of Leiden University once said: If A is a success in life, then A equals X plus Y plus Z. Work is X; Y is play; and Z is keeping your mouth shut. That lecturer was later known world-wide as Albert Einstein. Attracted by the glory of numerous renowned scholars, I started working as a PhD candidate in Leiden University Medical Center four years ago. During the time I am pursuing my PhD, many people walked in and out of my life. When you read these lines, you must be one of them who have left footprints. Therefore, I will like to take this opportunity to thank you all!

Following the alphabetical order, I shall start from A, but since the time I started studying in University of Groningen, I realized the importance of “C” (Being a scientist, one needs to be Critical&Creative). So, please allow me to express my full gratitude first to Clemens Löwik for being my supervisor. From drafting the first paper to teach me canoeing in New Hampshire, the allocation of your time invested in me is tremendous and invaluable. Your full enthusiasm and creativity motivated me to keep going all the way. No matter what happens, you always guide me. You always know what direction to go, what to do and sometimes, also what to skip. Thank you so much for believing in me!

My two co-supervisors, Eric Kaijzel and Ermond van Beek, thank you for guiding me throughout the entire PhD study. Eric, I am grateful to receive your guidance on how to communicate with colleagues via emails and in person. Ermond, I learned so much from your critical point of view towards science and also your “rustig” style in life.

My two paranymphs Laura Mezzanotte and Martijn Löwik, thank you very much for accompanying me in and out of the lab. Laura, thanks a lot for bringing your special Italian charm to the whole lab. It definitely spices up our days in the hospital. Martijn, supervising you in the lab is a pleasure, having you as a good friend is even more joyful.

I would like to personally thank other colleagues including, but not limited to: Ammar, Anna, Bart, Boudewijn, Dominique, Edwin, Ernst, Eugenio, Geertje, Guido, Henry, Isabel, Ineke, Jeroen, Jimmy, Judith, Jan-Willem, Jaap, Karien, Kassia, Kees, Luis, Louise, Lianne, Martijn V, Martiene, Man-Chi, Mieke, Marieke, Nancy, Patrick, Pieter D, Randa, Razvan, Trea, Thomas and Vicky. Special thanks go to Annelies, Chris, Frans, Hetty, Henny, Ivo and Joop for your constructive contributions to my PhD project. My appreciation goes to Danielle, Daniel and Bryan for your intensive and dedicated international collaborations.

I am indebted to Alan Chan for being a mentor, both at and outside our work. Thank you so much for infinitely guiding me to bridge the gap between Oriental and Western cultures! 多谢!

---

I am very grateful to Prof. Dr. Pancras Hogendoorn from Leiden, for your hospitality to allocate your time in between your super-busy-Dean agenda. I would like to also thank Prof. Dr. Bauke Dijkstra, Dr. Anton Steen and Dr. Armagan Kocer from Groningen. Having a wise talk with each of you from time to time always brings me precious guidance that lasts long.

Titanic was a great ship, it sunk; the greatest ship is still Friendship. I feel blessed to have friends from all over the world. Please excuse me for not listing you guys, I am sorry, you are not on the list, but you are always in my heart. Each of you is like the star in the dark night. I can always find you when looking up to the sky, even though you are far away! Especially, I thank the great companionship of PJ and Moni, thank you two for your dedication to design such a wonderful thesis! Special thanks to Timmy's loyalty and my deep commemoration for Yingying.

流金岁月，似水年华；海外求学，四海为家。古有云：宝剑锋从磨砺出，梅花香自苦寒来。历经四百余年风霜，莱顿大学仍执许多科研领域之牛耳。我为自己能在莱顿大学医学院攻读博士感到自豪，也为在此期间能结识许多志同道合的朋友而倍感欣慰。君子之交淡若水，我就不再一一致谢了。细水长流，友谊常存。

我要感谢我的父母，感谢你们给予我健康的身体与善良的心智。请谅解我不能随时陪伴在你们左右，但无论天涯海角，你们都让我体会到什么是大爱无言，无国界。我爱你们！同时，我深深感谢在中国的每一位亲朋好友，尤其感谢年迈的长辈对我的记挂。你们莫大的关怀与挂念，是我一直勇往直前的动力。最后，我借此机会怀念我已逝去的至亲小姨和外公。

Being abroad six years, I worked my way up from the bottom. I thank all the friends I have met, you made the world more pretty; I also thank all the challengers I have met, you made me stronger to overcome difficulties and to appreciate the life I have been building up.

Lastly, back to the "C", I am proud to be an ordinary person coming from a most common Chinese family. As the ancient Chinese philosopher Mencius said: When a man is destined for a great responsibility, it first starts with frustration of his spirit and will, harassment by troubles and setbacks, so as to toughen his nature and enhance his abilities beyond the limit.

Alright, enough "C", the last one I would like to bring us all is "Celebration"!





## Curriculum Vitae

The author of this thesis was born in Jiangxi, China, on September 27<sup>th</sup>, 1985. After finishing high school, he moved from his hometown to Beijing in 2003. He enrolled in the four-year Bachelor programme in Biotechnology at Beijing University of Agriculture. There, he grounded himself in theories of Biotechnology and fundamental methodologies of biological research. He broadened his vision by participating in various extracurricular activities, including chairing the English student association in the university. In 2005, he represented the university to compete in China Central Television (CCTV) Cup National English Speaking Contest and won the Excellent Prize at the Provincial Final. His proficiency in English and his eager to learn more in Biomolecular research led him to challenge himself to study abroad.

In June 2007, the author obtained his Bachelor degree in Biotechnology and received full Scholarship to study the Top Master Programme in Biomolecular Sciences and Biotechnology at University of Groningen, The Netherlands. After attending intensive and multidisciplinary courses in Biomolecular Sciences, he started his first research internship at Membrane Enzymology group headed by Prof. Dr. Bert Poolman. Afterwards, he moved to Eindhoven to start his second internship at Biomolecular Engineering group in Philips Research Europe. Inspired by Dr. Marc Robillard, he discovered his great interest in Molecular Imaging.

After receiving a Top Master degree in Science in September 2009, he started pursuing his PhD, under the supervision of Prof. Dr. Clemens Löwik at Leiden University Medical Center (LUMC), The Netherlands. He was involved in the Center for Translational Molecular Medicine (CTMM) project entitled “Intra-operative Multi-Spectral Imaging Systems for Radical Tumor” (MUSIS), with a main research focus on non-invasive optical imaging of cancer and cell death. During the four-year PhD programme, he developed an international research network by actively collaborating with American, Australian and German research groups. For the research he conducted during his PhD, he received several honors and awards: a Young Investigator Award Nominee at the 8<sup>th</sup> European Molecular Imaging Meeting in 2013, Italy; a Travel Stipend Award at World Molecular Imaging Congress both in 2012, Ireland and in 2013, United States of America.

He will start working as a Post-doc researcher in October 2013 for a Marie Curie IAPP grant (project acronym: BRAINPATH), which has been awarded to a consortium of eight different European partners from industry and academia.

---

## 作者简介

本论文作者一九八五年九月二十七日出生于中国江西省。他在二零零三年高中毕业后，离乡北上首都于北京农学院就读四年制生物技术学士课程。在那里，他夯实了自己在生物技术领域的理论基础，熟知了进行生物研究的基本方法。此外，通过参加各种课外活动，他开阔了视野，这其中包括了在大学期间担任院英语社学生协会主席。二零零五年，他代表了大学参加了“中国中央电视台(CCTV)杯”全国英语演讲比赛，并在决赛中获得了省级优秀奖。对英语的熟练掌握和对分子生物学进一步研究的渴求让他决定挑战自我，出国留学。

二零零七年六月，作者取得了生物技术学士学位并获得了在荷兰格罗宁根大学分子生物与生物技术系顶级硕士专业学习的全额奖学金。经过密集的分子生物多学科融合课程培训后，作者开始了他在以Bert Poolman 教授带领的膜酶学实验组的第一次研究实习。之后，他来到埃因霍温市飞利浦欧洲研发基地(Philips Research Europe)在分子生物工程组开始了他的第二次研究实习。在Marc Robillard 博士的启发之下，他对分子成像产生了极大的兴趣。

作者于二零零九年九月荣获顶级理学硕士学位，他继而在荷兰莱顿大学医学中心(LUMC) Clemens Löwik 教授的指导下开始攻读博士学位。他的博士项目隶属于荷兰临床分子医学转化中心(CTMM)旗下题为“手术中对肿瘤进行彻底切除的多光谱成像系统”(MUSIS)的科研项目，其研究的重点为对癌症和细胞死亡进行非侵入性光学成像。四年的博士学习，他通过积极地与美国、澳大利亚和德国的研究同仁合作，开拓了一个广阔的国际交流合作平台。博士期间，他获得多个荣誉和奖项：二零一三年第八届欧洲分子成像会议年度优秀青年研究者提名，二零一二年和二零一三年世界分子成像大会旅行津贴奖。

他将在二零一三年十月以博士后研究员身份加入居里夫人研究基金会旗下八个不同的欧洲产业界和学术界的合作伙伴组成的财团IAPP项目(项目代号：BRAINPATH)。

## Biografie

De auteur van dit proefschrift is op 27 september 1985 geboren in Jiangxi, China. Na het afronden van zijn middelbare school verhuisde hij naar Peking, alwaar hij het 4 jaar durende Bachelor programma in Biotechnologie heeft doorlopen aan de “Beijing University of Agriculture”. Daar heeft hij zich verdiept in de theoretische achtergrond van biotechnologie en fundamentele methodologieën van biologisch onderzoek. Hij verbreedde zijn visie door te participeren in diverse buitenschoolse activiteiten zoals onder andere het bekleden van het voorzitterschap van de Engelse Studenten Associatie binnen de universiteit. In 2005, vertegenwoordigde hij de Universiteit bij de wedstrijd uitgeschreven door China Central Television (CCTV) betreffende de best Engels sprekende student en won hij de “Excellent Prize” bij de provinciale finale. Zijn vaardigheid in het Engels en zijn gretigheid om meer te willen leren van biomoleculair onderzoek heeft er toe geleid dat hij graag de uitdaging aan wilde gaan om in het buitenland te studeren.

In Juni 2007, heeft de auteur zijn Bachelor graad gehaald in Biotechnologie en verwierf hij een volledige beurs om het Top Master Programma Biomoleculaire Wetenschappen en Biotechnologie in Groningen aan te vangen. Na het volgen van een aantal intensieve en multidisciplinaire cursussen in Biomoleculaire Wetenschappen, begon hij zijn eerste onderzoeksstage bij de Membraan Enzymologie groep van Prof. Dr. Bert Poolman. Hierna verhuisde hij naar Eindhoven om zijn tweede onderzoeksstage te beginnen bij de Biomoleculaire Engineerings groep binnen Philips Research Europe. Geïnspireerd door Dr. Marc Robillard, ontwikkelde hij een grote interesse voor Molecular Imaging.

Na het behalen van zijn “Top Master in Science” titel in september 2009, startte hij zijn promotieonderzoek onder leiding van Prof. Dr. Clemens Löwik binnen het Leids Universitair Medisch Centrum (LUMC). Hier was hij betrokken bij het “Center for Translational Molecular Medicine” (CTMM) project met de titel: “Intra-operative Multispectral Imaging Systems for Radical Tumor Resection”, of te wel het MUSIS project. Binnen dit project heeft de auteur zich bezig gehouden met non-invasieve optische beeldvorming van kankerweefsel en celdood in proefdieren. Tijdens zijn vierjarige promotietraject heeft hij een uitgebreid onderzoeksnetwerk ontwikkeld door intensief samen te werken met Amerikaanse, Australische en Duitse onderzoeksgroepen. Voor zijn promotieonderzoek verwierf hij verschillende onderscheidingen en prijzen zoals: Een “Young Investigator Nominee” op de achtste European Molecular Imaging Meeting in 2013 in Turijn; een “Travel Stipend Award” voor het “World Molecular Imaging Congress” voor zowel 2012 als 2013.

Vanaf oktober 2013 zal hij werkzaam zijn in het LUMC als post doc binnen het Europese Marie-Curie IAPP project met het acroniem “BRAINPATH” dat is toegekend aan een consortium van 8 verschillende Europese partners afkomstig uit de industrie en academische wereld.



## List of Publications

- Park D\*, **Xie BW\***, Van Beek ER, Blankevoort V, Que I, Löwik CW, Hogg PJ, Optical imaging of treatment-related tumor cell death using a heat shock protein-90 alkylator. *Mol Pharm*. 2013 Aug 22. [Epub ahead of print]
- **Xie BW\***, Park D\*, Van Beek ER, Blankevoort V, Orabi Y, Que I, Que I, Kaijzel EL, Chan A, Hogg PJ, Löwik CW, Optical imaging of cell death in traumatic brain injury using a heat shock protein-90 alkylator. *Cell Death Dis*. 2013; 4: e473.
- Smith BA\*, **Xie BW\***, van Beek ER, Que I, Blankevoort V, Xiao S, Cole E, Hoehn M, Kaijzel EL, Lowik CW, Smith BD. Multicolor Fluorescence Imaging of Traumatic Brain Injury in a Cryolesion Mouse Model. *ACS Chem. Neurosci*. 2012 Jul 18; 3(7):530-7.
- **Xie BW**, Mol IM, Keereweer S, van Beek ER, Que I, Snoeks TJ, Chan A, Kaijzel EL, Löwik CW. Dual-wavelength imaging of tumor progression by activatable and targeting near-infrared fluorescent probes in a bioluminescent breast cancer model. *PLoS One*. 2012; 7(2):e31875.
- Keereweer S, Mol IM, Kerrebijn JD, Van Driel PB, **Xie BW**, Baatenburg de Jong RJ, Vahrmeijer AL, Löwik CW. Targeting integrins and enhanced permeability and retention (EPR) effect for optical imaging of oral cancer. *J Surg Oncol*. 2012 Jun 1; 105(7):714-8.
- Keereweer S, Kerrebijn JD, van Driel PB, **Xie BW**, Kaijzel EL, Snoeks TJ, Que I, Hutteman M, van der Vorst JR, Mieog JS, Vahrmeijer AL, van de Velde CJ, Baatenburg de Jong RJ, Löwik CW. Optical image-guided surgery--where do we stand? *Mol Imaging Biol*. 2011 Apr; 13(2):199-207.

\* = co-first authors





